1-1-2015

Quantifying Magnetic Moments And Susceptibilities Of Small Cylindrical And Spherical Objects In Mri

Ching-Yi Hsieh
Wayne State University,

QUANTIFYING MAGNETIC MOMENTS AND SUSCEPTIBILITIES OF SMALL CYLINDRICAL AND SPHERICAL OBJECTS IN MRI

by

CHING-YI HSIEH

DISSERTATION

Submitted to the Graduate School

of Wayne State University

in partial fulfillment of the requirements

for the degree of

DOCTOR OF PHILOSOPHY

2015

MAJOR: MEDICAL PHYSICS

Approved by:

_____

Advisor Date

_____

Co − Advisor Date

_____

_____

_____

DEDICATION

To Mr. Ching-Hsiung Hsieh, Ms. Ming-Yueh Hsieh Chen, Ms. Mu-Hsien Hsieh, and Ms. Chiao Ju Hsieh, without their support, I could not be here.

ACKNOWLEDGMENTS

I owe my gratitude to a great number of people who have directly or indirectly helped me throughout my graduate study. Because of them, I have strength and perseverance to finish this PhD study journey. My deepest gratitude is to my advisor, Prof. Yu-Chung Norman Cheng, and my co-advisor, Prof. E. Mark Haacke, for their enduring support, encouragement and guidance all through my study. Prof. Norman Cheng, my advisor, has guided me and helped me considerably during the entire research. I am deeply grateful to him for his inimitable attention to detail during our long discussions related to my works and MR related questions. I would also like to thank Prof. E. Mark Haacke. He has not only taught me to be a good MR physicist but constantly encouraged me to become an independent thinker. I would like to thank the rest of my dissertation committee, Dr. Otto Muzik, Dr. Joe Rakowski, and Dr. Quan Jiang for taking time to make their suggestions and comments about my work.

I have met many wonderful and interesting people while conducting my research. All of them are wonderful people to work with. Dr. Jaladhar Neelavalli has always spent time helping my technical problems and providing his suggestions. Dr. Saifeng Liu has always provided the technical assistance in quantitative susceptibility mapping (QSM). Dr. Charbel Habib has provided suggestions for writing my dissertation. Mr. Zahid Latif, Mr. Yang Xuan, and Mr. Pavan Jella have always helped me scan the phantoms and acquire image data. I have always had insightful discussions with Mr. He Xie and Mr. Paul Kokeny. They are great teammates.

For my medical physics education, and training, Dr. Jay Burmeister, Dr. Charles E. Willis, and Dr. R. Jason Stafford have been great teachers I have ever met in my life. Especially, I need to show great appreciation to Dr. Charles E. Willis and Dr. R. Jason Stafford. They not only guided me through the imaging physics clinical training but also gave me free time to work on my PhD study while I was in the imaging physics residency program at MD Anderson Cancer Center, Houston, Texas.

This PhD journey has almost taken me ten years. During these years, a lot of great friends of mine have supported me in many ways on this PhD journey. Below are my dearest friends I want to show my appreciation.

Dr. Noel Kulik, Dr. Stuart Smith, Dr. Li Hsieh, Dr. Richard Young, Dr. Steve Scherbolein, Dr. Tinsu Pan, Dr. Frank E. Zink, Mr. Koho Vince Cousino Anila, Ms. Anzen Melanie Davenport, Mr. Robert Blank, and Mr. Wes Powell.

TABLE OF CONTENTS

LIST OF TABLES

LIST OF FIGURES

Chapter 1

INTRODUCTION

The bulk magnetic susceptibility, χ, is a fundamental material property that indicates how easy a substance can be magnetized under an external magnetic field. When a biological sample or a person is placed inside an MRI system with a strong magnetic field, different magnetic susceptibilities of tissues induce different local magnetic fields. Given these magnetic field differences, MR signals from these tissues result in contrasts between them. The induced field ΔB is associated with the MR phase image via $\phi = -\gamma \Delta B \tau$, where γ is the gyromagnetic ratio, τ is the time at which signal is detected, and ΔB is the induced magnetic field. The phase differences due to variations in magnetic susceptibility among biological tissues provides a special contrast which is different from the conventional T_1, T_2, and $T_2^\star$ contrast. The magnetic susceptibilities of tissues can be altered by many physiological/pathological mechanisms, for example, changes in tissue iron/calcium deposition, changes in blood oxygen saturation, and deposition of iron in the form of hemosiderin after a stroke. Many well-known neurological conditions such as Alzheimers, Parkinsons, multiple sclerosis and also aging reveal significant changes in iron/calcium depositions in cortical substructures [1, 2].

Susceptibility weighted imaging (SWI) utilizes susceptibility differences and enhances objects in phase images [3]. It has proven to be an effective MR sequence in the study of Alzheimers, Parkinsons, multiple sclerosis, aging, stroke, trauma, cerebral amyloid angiopathy (microbleeds), and Sturge Weber syndrome [1, 4, 5, 6]. However, SWI does not have the ability for quantification. As a result, it cannot distinguish between calcified

objects and hemorrhages, nor quantify the size changes of objects over time. To address these issues, this PhD work will introduce a method called Complex Image Summation around a Spherical or Cylindrical Object (CISSCO), which is effective for the magnetic moment quantifications of small objects from MR images. This CISSCO method adds complex signals of image voxels within a specified sphere or a long cylinder. The overall signal is equated to an analytical formula and we can systematically solve the unknowns in the equation. The unknowns include the effective proton density, volume of the object, and effective magnetic moment of the object. The CISSCO method minimizes quantitative errors due to three main problems in MRI: the partial volume effect, phase aliasing effect, and dephasing effect [7]. An important feature of this method is that the desired information can be extracted non-invasively from MRI without $a\ priori$ information.

My PhD work has developed the 2D and 3D CISSCO method with numerical simulations and phantom studies. In the 2D CISSCO method, I have also applied the method to the susceptibility measurements of several cerebral veins in human images. In addition, the uncertainties and limitations of the CISSCO method are also discussed in this PhD work. The chapters in this dissertation are arranged as follows. Chapter two will give a detailed overview of the 2D CISSCO method. Chapter three will give a detailed overview of the 3D CISSCO method. Chapter four extends the 2D CISSCO method to susceptibility and size quantifications of long cylindrical objects at different orientations with signals inside the objects. Chapter five applies the method in Chapter four for the quantification of the susceptibilities of cerebral veins. Finally, chapter six will address current applications and potential future directions of this method.

Chapter two, three, four, and five of my PhD dissertation have been already published

in the peer-review journals. The content of chapter two has been published in [8]. The content of chapter three has been published in [9]. The content of chapter four has been published in [10]. The content of chapter five has been published in [11].

Chapter 2

QUANTIFYING EFFECTIVE MAGNETIC MOMENTS OF NARROW CYLINDRICAL OBJECTS IN MRI

2.1 Introduction

Changes of blood oxygenation cause a change in the magnetic susceptibility of venous blood. This is the basis of functional magnetic resonance imaging (fMRI) (e.g., see [12]). For this reason, there has been a strong interest to quantify the magnetic susceptibility of venous blood. As a forward problem, researchers in MRI usually model a blood vessel as an infinitely long cylinder and calculate its MR signal with a known susceptibility of the vessel obtained from $ex\ vivo$ studies [13]. In order to avoid the partial volume effect in MRI but to obtain accurate results, an $ex\ vivo$ study usually analyzes the phase information both inside and outside a cylindrical test tube whose diameter occupies at least 10 image pixels [13]. If the wall thickness of the test tube can be neglected, this approach can accurately recover the susceptibility difference between the materials inside and outside the cylinder. On the other hand, the $in\ vivo$ measurement of the blood susceptibility has also been performed on vessels with large enough diameters (e.g., [14]). Nonetheless, the quantification of susceptibility of a cylindrical object with a small diameter has been a challenging problem and has not yet been tackled. Until recently, we [7] and Sedlacik et al. [15] have attempted to solve this inverse problem with two independent approaches. The former requires $a\ priori$ knowledge of the cylinder radius while the latter fits several variables to MR images from multiple long echo times, which can become impractical in $in\ vivo$ studies. In this chapter, we will demonstrate a general approach in the quantification of the effective magnetic moments of narrow cylindrical objects from only

one echo time of a gradient echo image. This new approach relies only on the known imaging parameters but not on the object size, which is usually not known in advance. From the magnetostatic theory [16], in the first order approximation, the magnetic moment per length of a long but narrow object is equal to that of an infinitely long cylinder. This concept makes our approach described in this chapter more applicable to long objects whose cross sections may not be exactly a disk. Practically, our approach may be applied to clinical MR images and industrial problems [17].

In this chapter, we will also show our improved method to identify the center of the cylindrical object. This improved method is robust as we will prove mathematically. Uncertainties of our methods including both the thermal noise from an object and the systematic uncertainty due to discrete pixels will be studied from the error propagation method [18]. By minimizing the uncertainty due to the thermal noise, we will derive criteria of how to effectively evaluate the magnetic moment of an object from images. Certain technical procedures that have been discussed in detail in [7] will be briefly mentioned here but will not be repeated. In the following sections, we will provide the general formulas but focus on null-signal objects perpendicular to the MRI main field in our phantom studies. Results from different imaging parameters will be shown. Objects with different orientations and limitations of our approach will be discussed toward the end of this chapter.

2.2 Material and Methods

The basic concept of our method is to add the complex MR signal of each voxel around a long cylindrical object of interest. As we model each object as an infinitely long cylinder, we only need to examine signals on a plane whose normal is parallel to the axis of the cylindrical object. The cross section of the cylinder on the plane is a disk of

which the circumference is a circle. Thus, these terms will also be used in this chapter. Theoretically, the MR signal around the infinitely long cylinder can be easily modeled. The total signal within a co-axial cylinder can be formulated and can be compared to the actual signal obtained from images, such that the effective magnetic moment can be solved. However, as different types of noise exist in images and the actual center of the object requires a subpixel determination, the challenge is to identify a set of robust procedures to fully solve this problem.

2.2.1 MR Signal of a Cylindrical Object

Applying an external magnetic field on an infinitely long cylindrical object with an absolute susceptibility χ_i embedded in an environment of susceptibility χ_o will induce a magnetic field ΔB both inside and outside the object [16]. If the distortion of the object can be neglected in images, after the correction of the Lorentzian sphere term and frequency adjustment by the MR systems, the phase value of the complex MR signal from a gradient echo sequence outside the cylinder is [12]

$$\phi_{out} = -\gamma \Delta B T_E = -\gamma \frac{\Delta\chi}{2} \frac{a^2}{\rho^2} B_0 T_E \cos 2\psi \sin^2\theta \tag{2.1}$$

where γ is the proton gyromagnetic ratio ($2\pi \cdot 42.58\,$MHz/T), T_E is the echo time, $\Delta\chi \equiv \chi_i - \chi_o$, a is the radius of the cylindrical object, ρ is the perpendicular distance measured from the axis of the cylinder, B_0 is the main field of the MR system, ψ is the polar angle associated with ρ, and θ is the angle between the main field direction and the axis of the cylinder. Figure 2.1 shows the coordinate system used in Eq. 2.1.

In the context of this chapter, it is $\Delta\chi$ that we wish to measure from experiments.

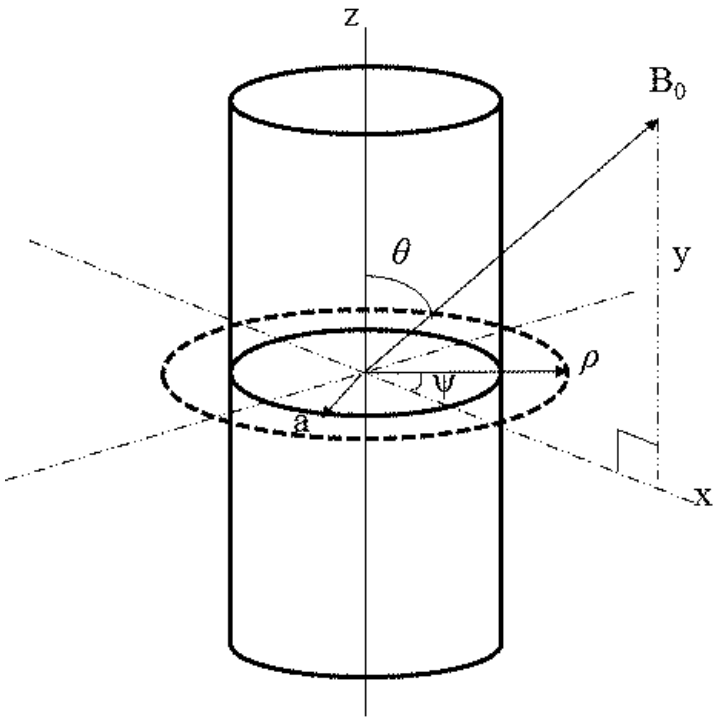

Figure 2.1: A schematic drawing shows the coordinate systems used in Eq. 2.1. Note that the axis of the cylinder is chosen to be parallel to the z-axis only for the derivation of Eq. 2.5. After deriving Eq. 2.5, only angle θ is relevant for further discussions.

Thus, the term susceptibility in this chapter refers to $\Delta\chi$ rather than the absolute susceptibility of the object. In addition, we have adopted SI units. From Eq. 2.1, we define the maximal (or minimal, depending on the sign of $\Delta\chi$) phase value g as

$$g \equiv 0.5\gamma\Delta\chi B_0 T_E \tag{2.2}$$

and the effective magnetic moment (or "magnetic moment, hereafter) as

$$p \equiv ga^2 \tag{2.3}$$

Under the same consideration, the induced phase value inside the cylinder is [12]

$$\phi_{in} = -\gamma \frac{\Delta\chi}{6}(3\cos^2\theta - 1)B_0 T_E = \frac{g}{3}(1 - 3\cos^2\theta) \tag{2.4}$$

If we consider a pseudo cylinder with radius R that is co-axial with the cylindrical object (see Fig. 2.2), for $g \neq 0$, the overall MR signal of the pseudo cylinder from a gradient echo sequence is [7]

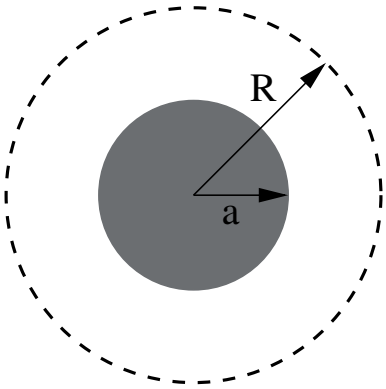

Figure 2.2: A schematic drawing shows the cross section of a cylindrical object with radius a, enclosed by a co-axial pseudo cylinder whose radius is R. The total MR signal within the pseudo cylinder can be formulated.

$$S = \ell\rho_0 \int_a^R d\rho\, \rho \int_0^{2\pi} d\psi\, e^{i\phi_{out}} + \pi\ell a^2 \rho_{0,c} e^{i\,\phi_{in}} = \pi\ell\rho_0 p \int_{p/R^2}^{g} \frac{dx}{x^2} J_0(x\,\sin^2\theta) + \pi\ell a^2 \rho_{0,c} e^{i\,\phi_{in}} \tag{2.5}$$

where ℓ is an arbitrary length of the cylindrical object and can be the slice thickness of the image, J_0 is the zeroth order Bessel function, $\rho_{0,c}$ is the effective spin density of the cylindrical object, and ρ_0 is the effective spin density of the tissue around the object. Both $\rho_{0,c}$ and ρ_0 are constants but depend on imaging and tissue parameters such as relaxation times. Although Eq. 2.5 is derived for an infinitely long cylinder, practically, it is the MR signal per unit length of the pseudo cylinder (S/ℓ) that is needed in our analysis. Thus,

an image slice whose normal component is parallel to the cylinder axis should be used in all quantifications. On that slice, the cross section of the cylindrical object appears as a disk. The same is true for the co-axial pseudo cylinder. The orientation of the cylinder, θ, can be estimated from the coordinates of the two ends of the cylindrical object in images. Therefore, the unknowns in Eq. 2.5 are reduced to g, p, ρ_0, and $\rho_{0,c}$.

2.2.2 Determining the Center of the Cylindrical Object

Equation 2.5 is valid only when the center of the disk (i.e., the cross section of the cylindrical object) is identical to the center of the pseudo disk. Thus the first step is to identify the center of the disk. When a cylindrical object itself has no MR signal, i.e., $\rho_{0,c} = 0$, we can identify the center of the object by minimizing the imaginary part of the signal (Eq. 2.5) within the pseudo disk [7].

When a cylindrical object has a non-zero $\rho_{0,c}$, even if the pseudo circle is replaced by two pseudo concentric circles such that the imaginary part from the annular ring is theoretically zero, the above approach still fails. This is because when the object has an imaginary part of the MR signal, its point spread function leads to an additional imaginary signal in each pixel outside the object. On the other hand, although the "subvoxel shift approach by [15] is valid, it requires many Fourier transformations of an image and thus longer computing time. We offer two alternate approaches below.

The first alternate approach is to maximize the real part of the signal from an annular ring region where the disk is completely inside the smaller pseudo circle. Assume that the annular ring region is formed by two pseudo circles with radii R_1 and R_2 and $a < R_1 < R_2$. The center of the object is located at coordinates (x_0, y_0) with $\sqrt{x_0^2 + y_0^2} + a \leq R_1$. The MR

signal from the annular ring is

$$S = \ell\rho_0 \int_{R_1}^{R_2} d\rho\, \rho \int_0^{2\pi} d\psi\, \exp\left\{-i\, g\frac{a^2}{\rho^2}\cos 2\psi \sin^2\theta\right\} \tag{2.6}$$

where the relations between ρ, ρ, ψ, and ψ in the integrand are given by $\rho\cos\psi = x_0 + \rho\cos\psi$ and $\rho\sin\psi = y_0 + \rho\sin\psi$. One can analytically prove that at $x_0 = y_0 = 0$, $\frac{\partial S}{\partial x_0} = \frac{\partial S}{\partial y_0} = 0$, and $\frac{\partial^2 S}{\partial x_0 \partial y_0} = 0$. Appendix D proves that the real part of the signal is maximum at $x_0 = y_0 = 0$ under certain conditions.

The second approach is to minimize the real part of the signal within one pseudo circle with radius R. With the parameters defined above and with $\sqrt{x_0^2 + y_0^2} < a$, the MR signal of the pseudo disk is

$$S = \ell\rho_0 \int_0^{2\pi} d\psi \int_{r(\psi)}^{R} d\rho\, \rho \exp\left\{-i\, g\frac{a^2}{\rho^2}\cos 2\psi \sin^2\theta\right\} + \pi\ell a^2 \rho_{0,c} e^{i\,\phi_{in}} \tag{2.7}$$

where the relations $\rho\cos\psi = x_0 + \rho\cos\psi$ and $\rho\sin\psi = y_0 + \rho\sin\psi$ still hold. In addition, $r(\psi)$ is the minimal value of ρ and satisfies $r(\psi)\cos\psi = x_0 + a\cos\psi$ and $r(\psi)\sin\psi = y_0 + a\sin\psi$. This leads to

$$(r(\psi)\cos\psi x_0)^2 + (r(\psi)\sin\psi y_0)^2 = a^2 \tag{2.8}$$

and

$$\begin{aligned} r(\psi) &= (x_0\cos\psi + y_0\sin\psi) + \sqrt{(x_0\cos\psi + y_0\sin\psi)^2 + (a^2 x_0^2 y_0^2)} \\ &= \sqrt{x_0^2 + y_0^2}\cos(\psi - \psi_0) + \sqrt{a^2(x_0^2 + y_0^2)\sin^2(\psi - \psi_0)} \end{aligned} \tag{2.9}$$

where $\cos\psi_0 \equiv x_0/\sqrt{x_0^2+y_0^2}$ and $\sin\psi_0 \equiv y_0/\sqrt{x_0^2+y_0^2}$.

Again, one can analytically prove that at $x_0 = y_0 = 0$, $\frac{\partial S}{\partial x_0} = \frac{\partial S}{\partial y_0} = 0$, and $\frac{\partial^2 S}{\partial x_0 \partial y_0} = 0$. Appendix E proves that the real part of the signal is minimum at $x_0 = y_0 = 0$.

All these approaches will fail when $\theta = 0$. In this special case, no phase value is outside the object (see Eq. 2.1). The MR signal becomes:

$$S = \ell\rho_0(A - \pi a^2) + \pi\ell a^2 \rho_{0,c} e^{-2i\,g/3} \tag{2.10}$$

where A is an arbitrarily shaped area that encloses the disk. Only the size of the object can be determined in this case.

2.2.3 Magnetic Moment of the Cylindrical Object

As shown in Fig. 2.3, if three arbitrary concentric circles with radii R_1, R_2, and R_3 are chosen, then three complex signals S_1, S_2, and S_3 can be calculated from MR images as described in [7]. In order to improve the accuracy of our approach, each image pixel is further divided into 100 subpixels in the calculations of the complex signals S_i [7]. From Eq. 2.5, we obtain

$$(S_1 - S_2)\int_{p/R_2^2}^{p/R_3^2} \frac{dx}{x^2} J_0(x\,\sin^2\theta) = (S_2 - S_3)\int_{p/R_1^2}^{p/R_2^2} \frac{dx}{x^2} J_0(x\,\sin^2\theta) \tag{2.11}$$

where the effective magnetic moment, p, becomes the only unknown in the equation. Note that both $\pm p$ satisfy Eq. 2.11 but the correct sign of p may be determined from MR phase images with the help of Eq. 2.1. From Eq. 2.1, it is clear that $p\sin^2\theta/R_i^2$ is the maximal (or minimal) phase value at the circumference of the i-th circle (where $i = 1, 2, 3$).

Therefore, if any R_i is chosen larger than the phase aliasing area, then $|p\sin^2\theta/R_i^2|$ will be always less than π and the solution of $|p\sin^2\theta|$ can be numerically searched between 0 and πR_{min}^2 with a Van Wijngaarden-Dekker-Brent method [19], where R_{min} is the smallest radius among three circles R_i. With the choices of $|p\sin^2\theta/R_i^2|$ in the following subsection, the solution of $p^2\sin^4\theta$ in Eq. 2.11 is unique. This is because $\int dx/x^2 J_0(x)$ can be well approximated by $-1/x - x/4$ in our consideration, which leads to a monotonic function of $p^2\sin^4\theta$ in Eq. 2.11. For example, when $|p\sin^2\theta/R_1^2|$ is 0.5 and $|p\sin^2\theta/R_2^2|$ is 1, the deviation between the exact integral and its approximation is 0.5%. When $|p\sin^2\theta/R_2^2|$ is 1 and $|p\sin^2\theta/R_3^2|$ varies from 2.5 to 3.0, the deviation increases monotonically from 7% to 12%. Thus, the initial guess of $|p\sin^2\theta|$ may be chosen as $\pi R_{min}^2/2$. After p is solved, the effective spin density ρ_0 can be solved from the signal of an annular ring, e.g., $S_1 - S_2$. The above discussion is generally valid except when the angle θ is close to zero. At $\theta = 0$, no magnetic moment appears in the signal, which is given by Eq. 2.10.

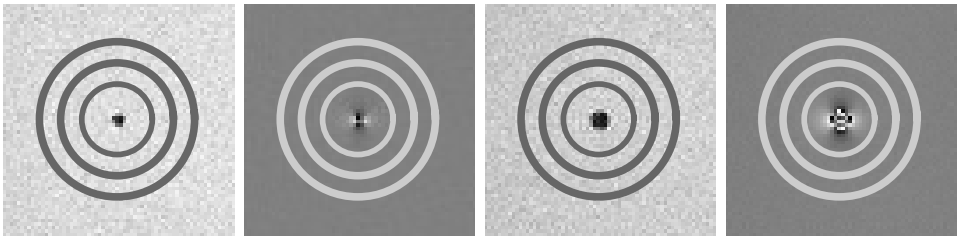

(a) (b) (c) (d)

Figure 2.3: (a) Magnitude and (b) its associated phase image at an echo time of 5 ms show an air cylinder in the gel phantom. (c) Magnitude and (d) phase image at an echo time of 20 ms show the same air cylinder in the gel phantom. Although the actual radius of the cylinder is 0.8 mm and the image resolution is 1 mm × 1 mm, cross sections of the cylinder appear to be different in magnitude images and larger than actual sizes. Note the dipolar phase aliasing patterns in the phase image (d). Circles are explained in the text.

2.2.4 Uncertainty of the Magnetic Moment

It is important to study the uncertainty of the method when it is applied to actual images. In addition, in order to determine the optimal choices of three radii for the quantification of the magnetic moment, the study of the uncertainty can provide some insights. Thermal noise due to the presence of an object and systematic noise due to discrete pixels in images always exist. They lead to the uncertainty of p. By defining $p \equiv p\sin^2\theta$ and rewriting Eq. 2.11, we can derive the uncertainty of p through error propagation [18]:

$$\frac{\delta p}{p} = \frac{\delta p}{p} = \frac{1}{|D|}\sqrt{(\delta(S_2S_3))^2 h_{12}^2 + (\delta(S_1S_2))^2 h_{23}^2} \tag{2.12}$$

where h_{ij} is defined as

$$h_{ij} \equiv \int_{p/R_i^2}^{p/R_j^2} \frac{dx}{x^2} J_0(x) \tag{2.13}$$

with $i, j = 1, 2, 3$ and

$$\begin{aligned} D &\equiv (S_1S_2)\frac{J_0(\phi_3)}{\phi_3} + (S_2S_3)\frac{J_0(\phi_1)}{\phi_1} + (S_3S_1)\frac{J_0(\phi_2)}{\phi_2} \\ &= \pi\ell\rho_0 p\left(h_{12}\frac{J_0(\phi_3)}{\phi_3} + h_{23}\frac{J_0(\phi_1)}{\phi_1} + h_{31}\frac{J_0(\phi_2)}{\phi_2}\right) \end{aligned} \tag{2.14}$$

Here $\phi_i \equiv p/R_i^2$ is chosen to be between 0 and π for all i. In the derivation of Eq. 2.12, we have already assumed that $R_3 < R_2 < R_1$ such that the uncertainty from the annular ring region between R_2 and R_3 is uncorrelated with the uncertainty from the area between R_1 and R_2. The uncertainty from each annular ring consists of the thermal noise and the systematic noise. Both noise sources are also uncorrelated. The former can be approximated by $\sigma\ell\sqrt{\Delta x\Delta y\pi|R_i^2R_j^2|}$ where σ is the standard deviation of the thermal noise

in the image and $\Delta x \Delta y$ is the image in-plane resolution [7]. The systematic noise is represented by ϵ_{ij} calculated from $\delta(S_i S_j) \equiv \epsilon_{ij}|S_i S_j|$ when the thermal noise is neglected. The uncertainty due to the systematic noise $\delta(S_i S_j)$ can be calculated if the center of the cylindrical object, the radius of the object, and the susceptibility difference are all known. Some examples were shown in [7, 20].

Equation 2.12 can be rewritten as

$$\frac{\delta p}{p} = \frac{\sqrt{\frac{\Delta x \Delta y}{\pi p \mathrm{SNR}^2}\left(\left|\frac{1}{\phi_2}\frac{1}{\phi_3}\right| h_{12}^2 + \left|\frac{1}{\phi_1}\frac{1}{\phi_2}\right| h_{23}^2\right) + (\epsilon_{12}^2 + \epsilon_{23}^2) h_{12}^2 h_{23}^2}}{\left|h_{12}\frac{J_0(\phi_3)}{\phi_3} + h_{23}\frac{J_0(\phi_1)}{\phi_1} + h_{31}\frac{J_0(\phi_2)}{\phi_2}\right|} \tag{2.15}$$

where SNR $\equiv \rho_0/\sigma$ is the signal to noise ratio of the magnitude image. In order to determine the optimal combination of ϕ_1, ϕ_2, and ϕ_3, for simplicity, we assume $\epsilon_{12} = \epsilon_{23} = 0$ in Eq. 2.15 and numerically search for the minimum of $\delta p/p$ with $0 < \phi_i \leq \pi$ for $i = 1, 2, 3$.

2.2.5 Resolving the Susceptibility When the Object Has No Spin Density

The susceptibility can be calculated from the known effective magnetic moment, if the radius of the object can be determined. Two approaches are considered to determine the radius of the object when the object has no spin density. The first approach is to utilize a spin echo sequence. The second approach is to perform a gradient echo sequence at a short echo time.

If a spin echo sequence is used to image the cross section of the object, the MR signal from an arbitrarily uniform area A that includes the object is:

$$S_{SE} = \rho_{0,SE}\ell(A - \pi a^2) \tag{2.16}$$

where $\rho_{0,SE}$ is the effective spin density (a constant) of the spin echo images. We have neglected the dephasing effect during the sampling time. With two arbitrary areas A_1 and A_2 such that A_2 is completely enclosed by A_1, $\rho_{0,SE}$ and the cross section of the object πa^2 can be determined. The uncertainty of the cross section can be derived from the error propagation method.

$$\delta(\pi a^2) = \frac{\sqrt{\Delta x \Delta y}}{\mathrm{SNR}} \sqrt{A_2 + \frac{(A_2 - \pi a^2)^2}{A_1 A_2}} \tag{2.17}$$

Note that SNR in Eq. 2.17 refers to the signal to noise ratio of the spin echo image. The noise between A_2 and $A_1 - A_2$ is uncorrelated. In order to minimize the uncertainty, it is obvious from Eq. 2.17 that the area $A_1 A_2$ should be chosen as large as possible before heterogeneity is encountered in the images, while the area A_2 should be chosen as small as possible but larger than πa^2. In fact, A_2 has to be larger than the area of the distorted object in the image so the cross section of the object can be estimated more accurately. In the gradient echo approach, an additional pseudo circle with radius R may be used to solve Eq. 2.5 as g becomes the only unknown after both p and ρ_0 are found. However, Fig. 2.4a demonstrates that the integral in Eq. 2.5 oscillates and quickly approaches an asymptotic value when $|g|$ or echo time increases (with a fixed p). This is due to the J_0 function and $1/x^2$ in the integrand. In order to obtain a unique solution of g from Eq. 2.5, the echo time T_E needs to be chosen short enough such that $|g|$ is at least less than 2.4, which is the first root of the $J_0(x)$ function. However, in order to distinguish the solution from the asymptotic value of the integral with the presence of noise in images, the value of $|g|$ may have to be much less than 2.4. The radius R also needs to be large enough such that $|p/R^2|$ is much less than 2.4. We will show some examples in the Results section.

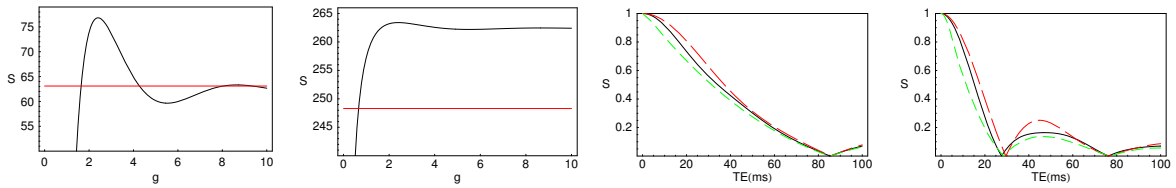

(a) (b) (c) (d)

Figure 2.4: Demonstration of the theoretical signals due to long echo times. For simplicity, no noise has been added in any of these simulations. (a) A plot of the integral in Eq. 2.5 as a function of g with $\rho_0 \ell = 10$ units, $a = 1\,\text{mm}$, $T_E = 5\,\text{ms}$, $\rho_{0,c} = 0$, and $R = 3\,\text{mm}$, such that p is $9.43\,\text{radian}\cdot\text{mm}^2$ and the true value of g is 9.43 radians. The actual MR signal S is represented by a horizontal line. The intersections of the horizontal line and the curve represent possible solutions of g. (b) Similar to (a), except that T_E is reduced to 0.35 ms, such that the true value of g is 0.66. (c) Normalized signals based on Eq. 2.5 as a function of echo time. The solid black curve is plotted with the volume fraction 0.1 and susceptibility 0.95 ppm from [15]. The dashed green curve and the dashed red curve are simulated with volume fraction 0.02 and 0.17, and susceptibility 4.75 and 0.57 ppm, respectively, such that the product of the volume fraction and susceptibility is identical in all three curves. (d) Similar to (c), but the black curve is simulated with volume fraction 0.3 and susceptibility 0.95 ppm. The dashed green curve and the red curve are simulated with volume fraction 0.1 and 0.43, and susceptibility 2.85 and 0.67 ppm, respectively.

2.2.6 Phantom Studies

Images from three different gel phantoms are analyzed in this chapter. The first set of images come from the phantom images in [7]. A narrow but long air cylinder with a diameter of roughly 1.6 mm appears in the images. Images acquired from a coronal 3D gradient echo sequence (Fig. 2.3) and a spin echo sequence are available for our re-analyses. The imaging parameters of the gradient echo sequence were: $T_E = 5$ ms and 20 ms, $T_R = 50$ ms, flip angle = 15°, read bandwidth = 390 Hz per pixel (Hz/pixel), resolution = 1 mm × 1 mm × 1 mm, and fields of view = 256 mm × 128 mm × 64 mm. The imaging parameters of the spin echo sequence were: $T_E = 8.4$ ms, $T_R = 400$ ms, read bandwidth = 130 Hz/pixel, resolution ≈ 0.55 mm × 0.55 mm, fields of view = 140 mm × 140 mm, slice thickness = 1.5 mm, 18 slices, and slice spacing = 1.95 mm.

The second set of images is from a phantom that consisted of a hollow straw in the

gel. As one end of the straw was sealed, the hollow straw created another air cylinder in the gel phantom. The diameter of the straw was 5.24 ± 0.01 mm. This phantom was prepared with 107 g of the gel powder in 1200 ml distilled water. The straw was placed vertically in the phantom when the gel was in its liquid form. Coronal images of a multiple echo 3D gradient echo sequence and a spin echo sequence were acquired. The imaging parameters of the gradient echo sequence were: $T_E = 5$ ms, 10 ms, and 15 ms, $T_R = 25$ ms, flip angle = 15°, read bandwidth = 610 Hz/pixel for $T_E = 5$ ms and 220 Hz/pixel for the other two echo times, resolution = 1 mm $\times$ 1 mm $\times$ 1 mm, and fields of view = 256 mm $\times$ 256 mm $\times$ 96 mm. The imaging parameters of the spin echo sequence were $T_E = 15$ ms, $T_R = 550$ ms, read bandwidths = 90 Hz/pixel and 590 Hz/pixel, resolution = 1 mm $\times$ 1 mm, fields of view = 256 mm $\times$ 256 mm, slice thickness = 2 mm, 20 slices, and slice spacing = 2 mm. Both air cylinders were placed perpendicular to the main field of the MR system. All images were acquired from a 1.5 T Siemens Sonata system. The phase images of the first set images were filtered by a high pass filter size of 32×32 [1] that has a minimal effect on our study here [7]. A high pass filter will also remove the eddy current effects and the constant background phase in a given set of phase images. For our second set of gradient echo images, we applied the line-by-line subtraction method, in order to remove the unwanted background phase around the object of interest in phase images. The line-by-line subtraction method was already described in [7]. This method also had a minimal effect on our studies in the chapter.

The distortion of objects in images (Fig. 2.5) due to the susceptibility effect was studied by varying the read bandwidth. These studies were preformed on another straw phantom made on a different day. The read bandwidths of the gradient echo sequence

at $T_E = 10$ ms were varied from 70 Hz/pixel, 220 Hz/pixel, 350 Hz/pixel, to 700 Hz/pixel. Other imaging parameters remained the same as those listed in the above paragraph.

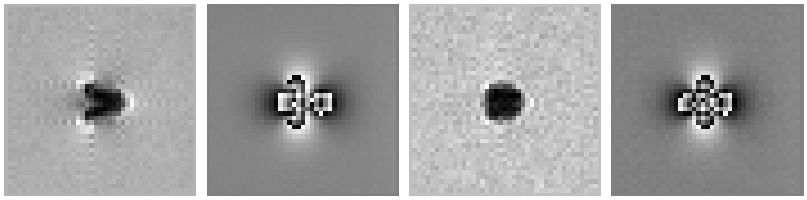

(a) (b) (c) (d)

Figure 2.5: Gradient echo gel images of an empty straw perpendicular to the main field with different read bandwidths are shown. The echo time of these images is 10 ms. (a) Magnitude and (b) its associated phase image were acquired with a bandwidth of 70 Hz/pixel. Note the distortion artifacts in both (a) and (b). (c) Magnitude and (d) phase image were acquired with a bandwidth of 350 Hz/pixel. No obvious distortion is observed in (c) or (d).

2.2.7 Image Simulations

In order to calculate the correct systematic noise (or uncertainty) due to discrete pixels, both image parameters and measured magnetic moments are used. In addition, the susceptibility difference between the air and gel is assumed to be 9.4 ppm [21]. The simulations and the addition of Gaussian noise were described in [7]. It is worth mentioning again that proper rotations of data after Fourier transformation are required. This is due to different definitions of the Fourier transformation in different computer software, but we follow the definition provided in [12].

In all simulations, we assume that $\theta = \pi/2$, $\Delta\chi = 9.4$ ppm, and $B_0 = 1.5$ T. The image resolution is set to 1 mm $\times$ 1 mm (or 1 pixel $\times$ 1 pixel). Other parameters are provided with corresponding simulated result in the next Section.

2.3 Results

2.3.1 Center of the Object

The one circle approach appears to be the easiest method in the identification of the object center. The radius of the pseudo circle cannot be too small or too large. In the former case, the thermal noise and discrete pixels will contribute significant uncertainty to the process. We would recommend a radius of at least three pixels. In the latter case, the overall MR signal will be dominated from the pixels without magnetic moment information and become insensitive to identifying the center. Equation C.2 in Appendix C is consistent with these considerations. Based on the phase images, a circle whose circumference intersects with phase values around ± 2 radians along the vertical and horizontal axes is a reasonable choice while the phase of 2.6 radians would be the optimal choice. In the approach of using two concentric circles, we suggest using radii that differ by at least one pixel such that enough pixels are used in the analysis. Based on our experience in simulation and phantom studies, the center of the object identified by any of our three procedures often differs from the actual center by 0.1 to 0.3 pixel. In addition, all the results from the one circle approach agree with the theoretical criterion (Eq. C.2 in Appendix C). We have also tried the approach by Sedlacik et al. [15] on some of our simulated images and have identified the same centers determined by our one-circle method. However, as the "subvoxel shift approach by [15] involves a 2D Fourier transformation of every possible center, while our method only requires a sum of complex numbers from the neighboring subpixels, our method takes less than half the computing time of their approach.

2.3.2 Optimal Choice of the Radii Combination

Simulations of Eq. 2.15 reveal that the uncertainty of the magnetic moment will be at a minimum when the three phase values are smallest, roughly 1 radian, and 2.5-3 radians. This result means that one circle should be chosen as large as possible while the other two circles should be chosen when their radii are roughly the lengths from the center of the object to the desired phase values. All circles should be outside the phase aliasing region. Due to the left handed setting by MRI manufacturers, note that the signs in all phase images of Fig. 2.3 are opposite to the signs in Eq. 2.1 (right handed system). Practically, as the uncertainty in the phase image is inversely proportional to SNR in the magnitude image [12], the radius of the largest circle can be chosen where the phase value is not smaller than 0.1 radian. Furthermore, as the MR signal is discretized and the center of the object may be different from the center of a pixel, the phase value measured from MR images may not be exactly equal to any of the above desired phase values and may not be symmetric around the object. In addition, phase values close to $\pm\pi$ radians may not be available from the phase profiles due to the partial volume effect. Simulated phase profiles shown in Fig. 2.6 reflect these practical problems. In any case, the phase profiles are only used as references for choosing the radii of the three circles for the measurements of the magnetic moment. It is not necessary to identify the exact phase values for our measurements. In fact, any choice of three circles can lead to a solution of the magnetic moment except that the uncertainty may be larger than desired (see below). Nevertheless, in order to better estimate the uncertainty (Eq. 2.15) due to each radius used in our analyses, we have averaged four radii and their corresponding phase values

taken from a vertical and a horizontal phase profile through the center of the object.

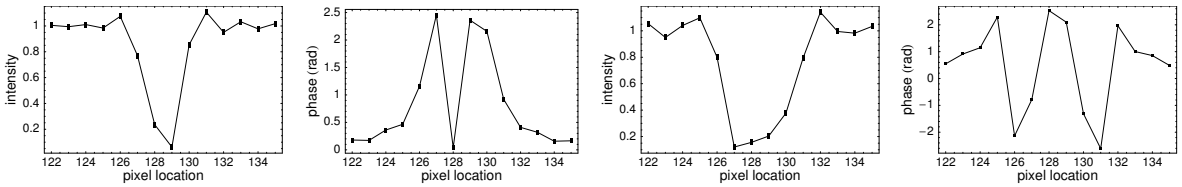

(a) (b) (c) (d)

Figure 2.6: An infinitely long cylinder with radius 0.8 pixel is simulated without the thermal noise. The center of the object is purposely shifted to the 128.9th pixel in simulations. Our method identified a center that is only 0.1 pixel away from the simulated center. The magnitude (a) and its associated phase profile (b) are simulated with an echo time of 5 ms. The magnitude (c) and its phase profile (d) are simulated with a T_E of 20 ms. Note the asymmetric phase patterns in (b) and (d) and asymmetric dephasing profiles in (a) and (c). These profiles agree very well with those obtained from actual gel phantom data. Also note that each pixel contains only one complex signal, displayed as dots in these plots. The lines connecting the dots have no special meaning.

2.3.3 Measurements of the Magnetic Moment

Table 2.1a lists the magnetic moments obtained from our previous data [7]. As the radii of the three circles are chosen as described above, the uncertainties calculated from Eq. 2.15 are less than 10%. As a comparison, when the radii of the largest circles are reduced, the uncertainties of the measured magnetic moments are increased but are still within 16% (Table 2.1b).

In theory, the effective magnetic moment is proportional to the echo time. The results of the magnetic moment obtained from different echo times clearly show that relationship within uncertainties in Table 2.1. With the known radius of the object 0.8 mm and an assumed $\Delta\chi = 9.4$ ppm, the theoretical magnetic moments at $T_E = 5$ ms and 20 ms are 6.04 radian·mm^2 and 24.14 radian·mm^2, respectively. That the magnetic moment at the bottom slice is smaller than that at the top is likely due to the collapsing of the air cylinder in the gel phantom.

Two slices of the second phantom (straw phantom) at three echo times are analyzed

and their results are shown in Table 2.2. As the diameter of the straw is 5.24 ± 0.01 mm, the theoretical magnetic moments at $T_E = 5$ ms, 10 ms and 15 ms are 64.7 radian·mm^2, 129.5 radian·mm^2, and 194.2 radian·mm^2, respectively. Even though the cross section of the straw is slightly deformed during the solidification of the gel solution, the measured magnetic moments are still in good agreement with the theoretical values and between themselves at different echo times. However, when the calculated uncertainty is less than 1%, one will need to consider the inaccuracy due to pure numerical algorithms which can be as large as 0.3% [7].

Table 2.3 shows magnetic moments of the straw at four different read bandwidths from the same slice. All the measured magnetic moments agree with each other within uncertainties. Therefore, our measurements of the magnetic moment from a gradient echo sequence do not seem to be affected by the distortion effect even at a relatively low bandwidth. The measured moments in both Tables 2.2 and 2.3 are slightly different from the theoretical values as the presence of the gel powder used in the phantoms can shift the susceptibility away from that of pure water. As we choose the radii outside the phase aliasing regions, we also effectively avoid the distortion effect.

2.3.4 Estimations of Object Volumes from Spin Echo Images

When the object has no spin density, the cross section of the object and its uncertainty are calculated based on Eq. 2.16 and Eq. 2.17. Three slices of the spin echo images from our previous study are analyzed as they correspond to slice 10, 19, and 37 of the gradient echo images. The measured cross sections are shown in Table 2.4. The result from slice 19 agrees well with the theoretical value of the object cross section, 2.01 mm^2. In general, the results from Table 2.4 also indicate a collapse at the bottom of

	$T_E = 5$ ms						$T_E = 20$ ms					
slice	radii (mm)	phases (radian)	moment p	δ	ϵ_{12}	ϵ_{23}	radii (mm)	phases (radian)	moment p	δ	ϵ_{12}	ϵ_{23}
10	(1.6, 2.7, 5.0)	(2.3, 1.0, 0.3)	7.11	4%	0.055	0.003	(3.1, 5.0, 7.0)	(2.4, 1.0, 0.3)	27.6	2%	0.022	0.005
19	(1.6, 2.4, 5.0)	(1.8, 1.0, 0.2)	5.82	8%	0.098	0.010	(3.6, 5.0, 7.0)	(2.1, 0.9, 0.3)	23.6	4%	0.010	0.004
28	(1.6, 2.4, 5.0)	(1.8, 1.0, 0.2)	5.56	9%	0.097	0.010	(2.9, 4.0, 7.0)	(2.0, 1.0, 0.3)	21.3	3%	0.060	0.005
37	(1.6, 2.6, 5.0)	(1.7, 0.7, 0.1)	5.07	8%	0.056	0.010	(2.9, 4.0, 7.0)	(2.0, 1.0, 0.3)	19.1	5%	0.054	0.039
43	(1.4, 2.6, 5.0)	(1.7, 0.9, 0.1)	4.62	5%	0.012	0.007	(2.5, 3.8, 7.0)	(2.0, 1.0, 0.2)	18.8	3%	0.052	0.001
46	(1.4, 2.6, 5.0)	(1.7, 0.9, 0.1)	4.52	4%	0.021	0.005	(2.4, 3.5, 7.0)	(2.0, 1.4, 0.2)	17.8	3%	0.040	0.005

(a)

	$T_E = 5$ ms						$T_E = 20$ ms					
slice	radii (mm)	phases (radian)	moment p	δ	ϵ_{12}	ϵ_{23}	radii (mm)	phases (radian)	moment p	δ	ϵ_{12}	ϵ_{23}
10	(1.6, 2.3, 2.7)	(2.3, 1.4, 1.0)	6.93	6%	0.01	0.12	(3.1, 3.6, 4.1)	(2.4, 1.9, 1.4)	26.1	6%	0.09	1.40
19	(1.6, 1.9, 2.4)	(1.8, 1.5, 1.0)	6.06	15%	0.48	0.17	(3.6, 4.2, 5.0)	(2.1, 1.3, 0.9)	23.7	9%	0.09	0.02
28	(1.6, 2.0, 2.4)	(1.8, 1.3, 1.0)	5.96	14%	0.21	0.23	(2.9, 3.4, 4.0)	(2.0, 1.4, 1.0)	21.0	7%	0.37	0.01
37	(1.6, 1.9, 2.3)	(1.7, 1.4, 1.0)	4.82	16%	0.14	0.09	(2.9, 3.4, 4.0)	(2.0, 1.4, 1.0)	18.3	10%	0.20	0.02
43	(1.4, 1.8, 2.1)	(1.7, 1.3, 1.0)	4.31	7%	0.02	0.05	(2.5, 3.4, 3.8)	(2.0, 1.5, 1.0)	18.6	4%	0.16	0.16
46	(1.4, 1.7, 2.2)	(1.7, 1.4, 0.9)	4.22	6%	0.02	0.03	(2.4, 3.4, 3.8)	(2.0, 1.5, 1.0)	17.0	4%	0.03	0.10

(b)

Table 2.1: (a) Magnetic moments of six slices from the existing images at echo times of 5 ms and 20 ms. The first column lists the slice number, with the smaller number representing the top slice. The second and the seventh columns list the values of the three radii (in units of mm or pixel) used in Eq. 2.11 to solve the magnetic moment. The third and the eighth columns list the corresponding averaged phase value of each radius. The fourth and the ninth columns list the magnetic moment solved from Eq. 2.11. The fifth and the tenth columns list the overall uncertainty of the magnetic moment from Eq. 2.15. This uncertainty, which includes both thermal noise and systematic noise, was calculated from the error propagation method and simulations, respectively. The sixth and the eleventh columns list the uncertainty of systematic noise calculated from simulations. The SNR of the images at both echo times is about 14:1. (b) Similar to (a), magnetic moments of identical six slices are analyzed with non-optimal choices of radius combinations. The phase of each radius listed in the third and the eighth columns was the interpolated and averaged value. Some measured cross sections are listed in Table 2.4

	Slice 30				Slice 35			
T_E (ms)	radii (mm)	phases (radian)	moment p	δ	radii (mm)	phases (radian)	moment p	δ
5	(6, 8, 13)	(2.3, 0.9, 0.2)	64.0	1.4%	(6, 9, 13)	(2.1, 1.0, 0.3)	63.3	1.5%
10	(7, 9, 14)	(2.4, 1.3, 0.5)	130	0.6%	(7, 10, 14)	(2.4, 1.2, 0.5)	128	0.6%
15	(9, 13, 16)	(2.5, 1.2, 0.7)	191	0.9%	(9, 13, 16)	(2.4, 1.1, 0.7)	193	0.9%

Table 2.2: Effective magnetic moments of the air straw measured at two different slices. The notation of each column is identical to that described in Table 2.1. The SNRs of images at $T_E = 10\,\text{ms}$ and $15\,\text{ms}$ are 23:1. The SNR of images at $T_E = 5\,\text{ms}$ is 15:1. The measured cross sections of the straw and the theoretical values of the magnetic moments are shown in the text.

Slice 10 at $T_E = 10\,\text{ms}$				
BW (Hz/pixel)	70	220	350	700
p (radian·mm^2)	125.1 ± 0.4	126.6 ± 0.6	124.7 ± 0.6	124.2 ± 1.0

Table 2.3: Study of the distortion effect in gradient echo images (Fig. 2.5). The theoretical value is $129.5\,\text{radian·mm}^2$. The results indicate that distortion has minimal effect to our method.

the phantom and an enlargement of the object at the top of the phantom.

For the straw phantom, one slice of the spin echo images at two different read bandwidths is analyzed. The SNR is 33:1 for images acquired with bandwidth 90 Hz/pixel and is 11:1 for images with bandwidth 590 Hz/pixel. The measured cross sections are $21.4 \pm 0.3\,\text{mm}^2$ and $22.2 \pm 0.8\,\text{mm}^2$ at bandwidth 90 Hz/pixel and 590 Hz/pixel, respectively. In the former case, $A_1 = 1148\,\text{mm}^2$ and $A_2 = 120\,\text{mm}^2$, while in the latter case $A_1 = 821\,\text{mm}^2$ and $A_2 = 69\,\text{mm}^2$. The theoretical value of the cross section is $21.6\,\text{mm}^2$ if the cross section is a perfect disk. As the straw has slightly deformed inside the gel phantom, its cross section may not be a perfect disk but has a smaller cross section than that of the perfect disk, given the same circumference. These results show good agreement between the measurements and the theoretical value within uncertainties predicted by Eq. 2.17. The results also indicate that the geometric distortion does not significantly affect the quantification.

Slice	A_1	A_2	$A_{measured}$	$A_{predicted}$
10	721	43	3.06 ± 0.74	2.31
19	725	39	2.75 ± 0.70	1.97
37	725	40	2.17 ± 0.71	1.59

Table 2.4: Three cross sections $A_{measured}$ of the narrow air cylinder are analyzed from the spin echo images. The areas of A_1 and A_2 are shown in the number of pixels while the values of $A_{measured}$ and $A_{predicted}$ are shown in units of mm^2. The uncertainties of the measured cross sections ($A_{measured}$) are calculated from Eq. 2.17. The predicted cross sections ($A_{predicted}$) are calculated from the magnetic moments in Table 2.1a divided by the assumed susceptibility difference 9.4 ppm. The uncertainties in this calculation are not listed. The SNR of the spin echo images is 5:1.

2.3.5 Resolving Susceptibility from Gradient Echo Simulations with No Spin Density of the Object

In addition to our efforts in the previous subsection, we also explore the possibility of quantifying susceptibility from gradient echo images. We investigate this possibility with simulations. If all variables and parameters are known, we can calculate the MR signal in each case. Such an MR signal is a number and is displayed as a horizontal straight line in Fig. 2.4a or 2.4b. On the other hand, if the magnetic moment p is known but the susceptibility and object radius are not known, then we can simulate the MR signal as a function of g, as shown as a curve in Fig. 2.4a or 2.4b. The intersections of the curve and the line indicate the possible solutions of the susceptibility. The result shown in Fig. 2.4a indicates that the minimal value of $|\Delta\chi|$ (with a fixed p) can be extracted at a given echo time. In this example, the minimal value of $|\Delta\chi|$ is roughly 1.5 ppm, much less than 9.4 ppm used for the image simulations. If the echo time is shortened, as shown in Fig. 2.4b, then g or susceptibility is likely to be uniquely determined. If the thermal noise is added as one arbitrary unit (compared to $\rho_0\ell$, which is 10 units) and an image resolution is assumed as 1 mm^2, then the uncertainty of the signal S within a radius R (3 mm) is roughly

5.3 units ($\sqrt{\pi R^2}/\sqrt{\Delta x \Delta y}$). This means that the signal S is within one standard deviation of the asymptotic value shown in Fig. 2.4a when g is larger than roughly 3.5. On the other hand, with a much shorter echo time (which may be impractical), the susceptibility and radius of the object can be resolved from Eq. 2.5 and Fig. 2.4b. However, this result implies that the spin echo approach presented in the above subsection seems better.

The examples shown in Fig. 2.4a and 2.4b indicate that one cannot accurately determine the susceptibility and object size through a curve fitting of data from long echo times, where g becomes too large. If sufficient noise had been included in the simulations, both Fig. 2.4c and 2.4d demonstrate that the volume fraction and susceptibility each can only be roughly determined at orders of magnitude through curve fitting. However, when an object has enough MR signal, the curve fitting method appears applicable to determine the susceptibility and volume of the object [15]. This is because Eq. 2.4 only contains the susceptibility information (i.e., g), rather than the magnetic moment (i.e., p).

2.4 Discussion

Three common problems in MRI have been overcome in our method of obtaining the magnetic moment: partial volume effect, dephasing effect (signal loss shown in Fig. 2.6a and 2.6c), and the phase aliasing effect (shown in Fig. 2.6d). In our examples, the partial volume effect is overshadowed by the dephasing effect. These are practical reasons why our method applied on small objects is much better than the conventional least squares fitting method or the method of measuring the relaxation time T_2^*. Some results of how bad the least squares fitting method has performed are shown in [7].

As shown in Fig. 2.6, even when the object has no signal, the actual center of the object may not be in the pixel with the lowest magnitude signal. This fact implies that the

center of the object has to be determined based on the information outside the object, as suggested by our procedures here or by Sedlacik et al. [15]. However, the approach by [15] will take much longer time than ours.

After the center of the object is identified, two phase profiles through the object center along the vertical and horizontal directions are used for the selections of the radii of three circles. All three circles should be larger than the phase aliasing area around the object but the smallest circle should be as small as possible (i.e., as close to the aliased phase as possible). However, as shown in Fig. 2.6, the maximum phase value may not be close to $\pm\pi$ radians but a choice of a slightly larger radius of the smallest circle does not seem to increase the uncertainty much. Due to the discrete pixels, a function can be used to interpolate the phase values such that more accurate phase values can be used for the selections of three radii at non-integer pixels. For this purpose, we have tried a linear function and a function based on Eq. 2.1 and we have found no difference of which function to use. This is clearly supported by the fact that Eq. 2.11 does not rely on the knowledge of phase values, which only serve as references of how to choose the radii. The radii of non-integer pixels are an important feature in our method. For example, if we consider two radii at 2.3 and 2.6 pixels, both radii refer to the same pixel along the vertical and horizontal directions. However, as the signal inside a circle can change even with a slight change of its radius, Eq. 2.11 offers a much more accurate way to solve the magnetic moment. Practically, a uniform region may appear only around the neighborhood of the object. Even with non-optimal choices of radii, our method appears to be effective as most of the uncertainties listed in Table 2.1b are still within 10%.

The uncertainty $\delta p/p$ derived from Eq. 2.15 is inversely proportional to SNR and $\sqrt{p}$

(or $\sqrt{T_E}$). This is clearly shown in Table 2.1. Although Eq. 2.15 implies that the longer the echo time, the smaller the uncertainty, it is important to remember that the SNR of the material around the object will also reduce when the echo time increases. Thus, if the echo time is longer than the relaxation time T_2 of the surrounding material, the uncertainty will likely increase.

The systematic uncertainty and the uncertainty due to the thermal noise in the measurements of magnetic moments are comparable in most of our phantom studies. Although all sources of uncertainties are considered uncorrelated in Eq. 2.15, actually, the systematic uncertainties from two annular rings S_1S_2 and S_2S_3 may be partially correlated as they share the same boundary ($2\pi R_2$). However, we have neglected that correlation in this research.

Given the uncertainties and magnetic moments shown in Table 2.1, the internal collapsing of the air cylinder in the first phantom seems the only explanation. The measurements of the cross sections from the spin echo images also support this finding (Table 2.4). This collapsing is not obvious from the visual inspection of images. Assuming $\Delta\chi = 9.4$ ppm, the radius of the air cylinder appears to change from 0.8 mm (slice 19) to 0.67 mm (slice 46). With an image resolution of 1 mm $\times$ 1 mm, such a subpixel change of the object radius can be clearly distinguished from our magnetic moment measurements.

The presence of the object susceptibility can lead to distortion artifacts and dephasing effects in images. They occur in all images but in the gradient echo images the dephasing effect at the echo dominates the artifacts unless the read bandwidth is very low. A usual way to minimize the distortion artifacts is to increase the read bandwidth in a sequence. However this change will lead to a lower SNR in images and thus a larger

uncertainty (Eq. 2.15 and Table 2.4). Our phantom studies indicate that the geometric distortion does not seem to affect the measurements of magnetic moment as shown in Table 2.3. In the spin echo images, as the dephasing effect due to the susceptibility difference can be enhanced during the sampling period, the measured volume of the object should be treated as the maximal volume. This is supported by the results shown in Table 2.4. The geometric distortion also does not seem to affect the volume measurements of the objects from the spin echo images.

Although the absolute susceptibility of gel is assumed as the same as the absolute susceptibility of water, -9 ppm, in our analyses, the actual susceptibility of the gel may be slightly different than that of water.

2.4.1 Resolving Susceptibility and Volume when the Object Has No Spin Density

Further examination of Eq. 2.17 indicates some interesting aspects and the limitation of the spin echo approach. If the cross section of the object occupies more than one pixel in the image, then the uncertainty estimated from Eq. 2.17 does not depend on the image resolution but it depends on the fields of view. This is because SNR is proportional to $\sqrt{L_x L_y \Delta x \Delta y}$ where L_x and L_y are the fields of view along the two orthogonal directions. However, if the cross section of the object is within one pixel, then the smallest A_2 that can be chosen is $\Delta x \Delta y$. If the second term in Eq. 2.17 can be neglected, then the uncertainty is proportional to $\sqrt{\Delta x \Delta y}/\sqrt{L_x L_y}$. This means that a spin echo image with a high resolution can determine the size of the object more accurately, even at the expense of a low SNR or a long imaging time. On the other hand, if the object is less than one pixel after the image has been acquired, the uncertainty of Eq. 2.17 in this case becomes $\Delta x \Delta y$/SNR. This means that if the volume fraction of the object in a pixel ($\pi a^2/(\Delta x \Delta y)$)

is less than 1/SNR, the estimated uncertainty of the cross section is more than 100%.

Practically, a spin echo sequence is routinely performed in each clinical diagnosis. As the magnetic moment can be determined from one gradient echo sequence described in Section 2.2.3, knowing the radius of the object will automatically lead to the value of susceptibility. The only exception is when $\theta = 0$. In this special case, only the size of the object can be determined. When a gradient echo image and a spin echo image are analyzed, no registration of the images is required in our approach.

In the gradient echo approach, the susceptibility and volume cannot be resolved individually when the susceptibility is larger than a certain value with a fixed magnetic moment (see Fig. 2.4a). This is consistent with the theory of electromagnetism, as in the far field the magnetic moment of an object is the leading term [16]. In general, our experience shows that the gradient echo approach for determining object susceptibility is not favorable, as the desired echo time to minimize distortions and signal losses may need to be very short and thus require a very high read bandwidth. For this reason, the spin echo approach is a better method.

2.5 Conclusion

Our method can accurately quantify the effective magnetic moment of a narrow cylinder from MR images. It has overcome three general problems in MRI and is applicable to small objects in a locally uniform background. However, the application of our method is not limited to small objects. The effective magnetic moment of an object can be obtained from standard gradient echo images while the volume of the object may be derived from typical spin echo images. We have demonstrated the feasibility of our approaches through phantom studies. In addition, a phantom study has revealed that a subpixel

change of the object volume can be distinguished from the change of magnetic moment using our method in MRI.

Chapter 3

MAGNETIC MOMENT QUANTIFICATIONS OF SMALL SPHERICAL OBJECTS IN MRI

3.1 Introduction

Cerebral microbleeds and small calcifications appear as small dark round spots in magnetic resonance (MR) magnitude images. They exist in elder populations or patients with dementia (e.g., see [22]). Currently, except for number counting, there is no effective method of quantifying these objects. Similarly, localized nanoparticles also appear as dark round spots in images (e.g., see [23]). The least squares fit method is currently the "best method of quantifying magnetic moments of nanoparticles [23]. However, a good fit to the magnetic field distribution requires many voxels outside the nanoparticle dephasing region. As the magnetic field outside an object decreases quickly, the least squares fit method is only useful for an object with a very large magnetic moment. When the magnetic moment of an object is not large enough, even in the 2D case, the least squares fit method becomes inaccurate [7]. Recent quantitative susceptibility mapping (QSM) techniques also cannot accurately measure the magnetic moments or susceptibilities of small objects (e.g., see [24]). In fact, before one can reliably quantify susceptibility of a small object from MRI, one must first quantify the magnetic moment of the object. This is particularly true if we only use MR phase images to quantify the magnetic property of a spherical object, as phase is proportional to the effective magnetic moment of the object rather than the susceptibility alone. This makes the quantification of magnetic moment as important as the quantification of susceptibility for small objects in MRI.

In this chapter, we demonstrate a new method in the quantification of effective mag-

netic moments of spheres from MR images. This 3D method follows similar ideas described in the 2D case [8] but its mathematical derivations are much more complicated. The combination of this 3D method and the previous 2D cylindrical method is the CISSCO (Complex Image Summation around a Spherical or a Cylindrical Object) method. The CISSCO method relies only on the known imaging parameters and assumes that an object of interest is a sphere or an infinitely long cylinder. From the magnetostatic theory [16], in the first order approximation, the magnetic moment of a small object with an arbitrary geometry is equal to that of a perfect sphere. This concept makes our 3D method described in this chapter applicable to spherical-like objects such as microbleeds, nanoparticles, and maybe industrial particles [17].

In the following sections, a procedure and its mathematical proof will be given to identify the center of the spherical object. Detailed procedures of magnetic moment quantification will be presented. Uncertainties of quantified magnetic moments including both the thermal noise from the object of interest and the systematic errors due to discrete pixels will be studied from the error propagation method [18]. By minimizing the uncertainty due to the thermal noise, we will derive the criteria of how to effectively evaluate the magnetic moment of a given object in images. Effective magnetic moments of glass beads will be measured by both MRI and a SQUID (superconducting quantum interference device) based magnetometer. Results of simulations and phantom studies from different imaging parameters will be compared and will be followed by discussions. Although we focus on objects without MR signals in this chapter, the procedures of measuring the magnetic moment are applicable to objects with signals (see Eq. 3.1 and Eq. 3.6 below).

3.2 Methods

The basic concept of the CISSCO method is to add the complex MR signal of each voxel around an object of interest. From the statement in the above introduction, this object can be modeled as a perfect sphere. The overall signal from space within a concentric sphere of the spherical object is given by [25]

$$S = \rho_0 \int_0^{2\pi} d\phi \int_0^{\pi} d\theta \, \sin\theta \int_a^R dr \, r^2 \, e^{-ip(3\cos^2\theta - 1)/r^3} + s_c = \frac{4\pi}{9\sqrt{3}} \rho_0 a^3 \int_{-1}^{2} dx D(x) e^{-igx} + s_c \tag{3.1}$$

where $p \equiv \gamma \Delta\chi B_0 T_E a^3/3$ and $D(x)$ is proportional to the density-of-states

$$\begin{aligned} D(x) &= \tfrac{1}{x^2}(2-x)\sqrt{1+x} && \text{when } x \in (-1, -\lambda) \text{ or } (2\lambda, 2) \\ &= \tfrac{1}{x^2}\left[(2-x)\sqrt{1+x} - \left(2 - \tfrac{x}{\lambda}\right)\sqrt{1+\tfrac{x}{\lambda}}\right] && \text{when } x \in (-\lambda, 2\lambda) \\ &= 0 && \text{otherwise} \end{aligned} \tag{3.2}$$

The effective spin density of the material outside the spherical object is modeled as a constant ρ_0, which depends on imaging and tissue parameters such as relaxation times. The signal from the spherical object itself is s_c and is a constant (real number) depending on object volume and imaging parameters. The radius of the object is a. The effective magnetic moment p (hereafter magnetic moment, unless otherwise specified) is defined as ga^3 and the extremum phase g is defined as $\gamma \Delta\chi B_0 T_E/3$, where γ is the gyromagnetic ratio $2\pi \cdot 42.58$ MHz/T, $\Delta\chi$ is the magnetic susceptibility difference between the susceptibility of the object and that of the surrounding material, B_0 is the MRI main field strength, and T_E is the echo time. Hereafter the word susceptibility refers to $\Delta\chi$ unless otherwise

specified, as this is the variable that MRI measures. The azimuthal angle θ is measured from the main field direction and is defined by the spherical coordinate. The distance r is measured from the center of the object in the spherical coordinate. Lastly, $\lambda \equiv (a/R)^3$ is the volume fraction where R is the user defined radius of a concentric sphere. If the center of the object can be determined and thus the concentric sphere can be correctly positioned, the unknowns in Eq. 3.1 to be solved are ρ_0, $\Delta\chi$, a, and s_c.

In principle, the theoretical signal S can be compared to the actual signal and those unknowns may be quantified. However, as there are various types of noise to consider and the center of the spherical object must also be determined, the biggest challenge is to identify a set of robust procedures for accurate quantification of the magnetic moment which is directly related to the susceptibility.

3.2.1 Numerical simulations

We conduct three sets of simulations. The first task is to validate Eq. 3.1 with numerical simulations. We assign zero signal inside each spherical object but unity for ρ_0 in this first study. The radius of a simulated spherical object (a) has to be at least 32 grid points in order to reduce the error within 0.3%, due to an imperfect spherical surface. The main field B_0 and the echo time T_E are chosen to 1.5 T and 5 ms, respectively. The susceptibility difference $\Delta\chi$ is changed from 10^{-3} ppm to 10^4 ppm by every order of magnitude. The overall signal S within a given radius R can be calculated by replacing the 3D integrals in Eq. 3.1 by the discrete sums of the complex signal at each grid point. On the other hand, the complex signal S can also be calculated directly from the single integral, using Eq. 3.2. If Eq. 3.1 is correct, both results should be equal to each other. Several values of R are used in our simulations. For $\Delta\chi \leq 1$ ppm, the value of R is chosen to be at least

6 grid points larger than the radius a, in order to have sufficient signals included in S. For $\Delta\chi > 1$ ppm, the radius R varies but it should satisfy $0.1 \leq p/R^3 \leq \pi$. (See Section 3.3.3 for the reason of limiting p/R^3 in this range.) The comparisons between the discrete sums and integrals of signals from Eq. 3.1 provide us the numerical errors in our method.

The purpose of the second set of simulations is to properly model the discrete nature of MRI data. This will allow us to study the systematic noise (or error) due to discrete voxels in MRI. For this purpose, we simulate MR signals induced from a sphere with a fixed radius of 32 points on 1024^3 grid points in the spatial domain but at different echo times. Then we Fourier transform the simulated data into k-space based on the definition used in MRI (e.g., see [26]), take the central 32^3 points in k-space, and inverse Fourier transform the data back to the spatial domain. These processes mimic the digitized (or discretized) MR signal and the reconstructed MR images, which display a spherical object with an effective radius of one pixel and a field-of-view of 32 pixels. With a limited computer memory, we first need to simulate and perform Fourier transformation of every 1024^2 points, store the data in the hard drive, and then repeat the process through the third dimension. Other parameters used in simulations are $B_0 = 1.5$ T, $\rho_0 = 10$ units, and $\Delta\chi = 10$ ppm. Echo times 5 ms, 10 ms, 15 ms, and 20 ms are used in this set of simulations. We also shift the centers of spherical objects in our simulations and study the effects. For example, if we shift the center of an object by 8 points on the original 1024^3 grid, we effectively shift the object center by 0.25 pixel on the reconstructed 32^3 images.

The systematic noise (ϵ in Eq. 3.15 below) is calculated as the absolute difference between the real part of the simulated signal (within a given R) and that of the theoretical signal (from the integral of Eq. 3.1 with Eq. 3.2) divided by the real part of the theoretical

signal. The object centers at different subpixel positions, g, and a are also inputs to our simulations in order to calculate systematic errors.

The purpose of the third set of simulations aims to add the thermal noise onto the above second set of images. The thermal noise is Gaussian distributed with a zero mean and a standard deviation σ. The thermal noise is added onto the real and imaginary part of the images and is generated by a random number generator [19]. The theoretical signal to noise ratio (SNR) in images is defined by ρ_0/σ. In our simulated images, we choose an SNR of 10:1. This is achieved by assigning one unit to the standard deviation in the Gaussian distributions (as $\rho_0 = 10$ units). Example images without and with a shifted object center are shown in Fig. 3.1.

Most of our simulations were performed on a personal computer with an Intel Pentium 4 Processor of 2.6 GHz and 2.56 GB memory. Some tests were carried out in higher power computers. Although Mathematica, Matlab, C, and C++ programs were used in simulations and following calculations, the C and C++ programs were the major utilities.

3.2.2 Calculations of signals from images

In order to improve the accuracy when adding MR signals from images within a sphere of a given radius R, we have divided each voxel into 1000 subvoxels (i.e., a factor of 10 along each direction). The MR signal in each subvoxel is 0.001 of the signal in the original voxel. This procedure is applied throughout this chapter whenever the overall complex signal within a radius R is calculated from either simulated or phantom images.

3.2.3 Identifying the center of a spherical object

Equation 3.1 is valid only when the center of the spherical object is identical to the center of the concentric sphere with a radius R. Thus before the quantification of the

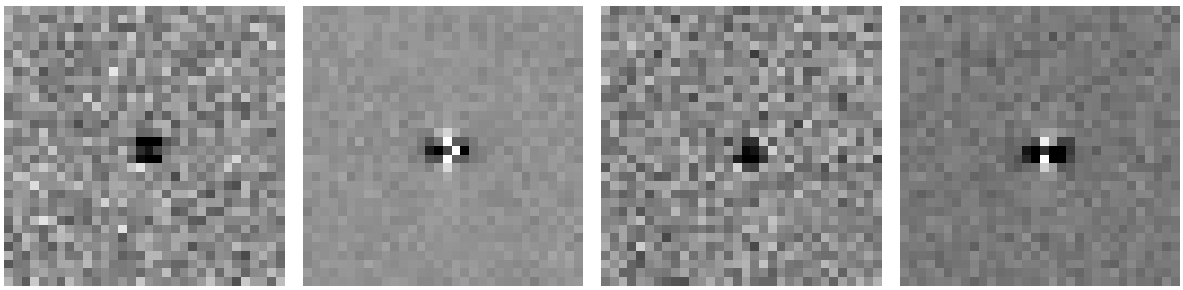

(a) (b) (c) (d)

Figure 3.1: Examples of simulated images. Coronal views are displayed here. The SNR is 10:1 and echo time is 5 ms in these images. Radius of the object is 1 pixel. Other parameters used in simulations are described in the text. (a) Magnitude and (b) its associated phase image of a spherical object whose center is located at the corner of a voxel. In this case, the center of the object is considered as unshifted. (c) Magnitude and (d) its associated phase image of the same object whose center, however, has been shifted by roughly 0.3 pixel along both the x-direction and the z-direction. Thus, the overall shift of the object center is roughly 0.42 pixel. The phase pattern right around the object in (d) is clearly different from that in (b).

magnetic moment, we need to identify the center of the object. We have considered three possible procedures. One is to maximize the real part of the signal from a given spherical shell around the object. Another is to minimize the real part of the signal within a given sphere. The other is to identify the object center at which the sum of the phase values of the complex signals within a given sphere is zero (given the $(3\cos^2\theta - 1)/r^3$ phase distributions). The main idea in each procedure is to choose a sphere or a shell, move the sphere or shell around the object, sum up the complex signals or phases within the sphere or shell, and determine the object center when the minimal or maximal value of the overall summed signals has occurred. Equivalently, in the following proofs, we consider a fixed shell and a fixed sphere with their centers at the origin, but move the spherical object around. When extremum occurs, the center of the object will coincide with the center of the fixed shell or the center of the fixed sphere.

In the procedure of maximizing the real part of the shell signal, the object should be

completely inside the inner sphere of the shell. Assume that the shell is formed by two concentric spheres with radii R_1 and R_2 and $a < R_2 < R_1$. The center of the object is assumed to be located at coordinates (x_0, y_0, z_0) with $\sqrt{x_0^2 + y_0^2 + z_0^2} + a \equiv r_0 + a \leq R_2$. The MR signal from the shell is

$$S = \rho_0 \int_{R_2}^{R_1} dr\, r^2 \int_0^{2\pi} d\phi \int_0^{\pi} d\theta\, \sin\theta \exp\left\{-i\frac{p}{d^3}(3\cos^2\theta - 1)\right\} \tag{3.3}$$

where $d^2 = (r\,\cos\phi\,\sin\theta - x_0)^2 + (r\,\sin\phi\,\sin\theta - y_0)^2 + (r\,\cos\theta - z_0)^2$ and $d\cos\theta + z_0 = r\cos\theta$. One can analytically derive that, at $r_0 = 0$, $\dfrac{\partial S}{\partial x_0} = \dfrac{\partial S}{\partial y_0} = \dfrac{\partial S}{\partial z_0} = 0$. Derivations of second derivatives are provided in Appendix D.

The second approach is to minimize the real part of the signal within one sphere with a radius R. With the parameters defined above and with $r_0 < a$, the MR signal of the concentric sphere is

$$S = \rho_0 \int_0^{2\pi} d\phi \int_0^{\pi} d\theta\, \sin\theta \int_{\rho(\theta,\phi)}^{R} dr\, r^2 \exp\left\{-i\frac{p}{d^3}(3\cos^2\theta - 1)\right\} + s_c \tag{3.4}$$

where $\rho(\theta, \phi)$ satisfies $(\rho\cos\phi\sin\theta - x_0)^2 + (\rho\sin\phi\sin\theta - y_0)^2 + (\rho\cos\theta - z_0)^2 = a^2$ and

$$\begin{aligned} \rho(\theta,\phi) \;=\; & x_0\cos\phi\sin\theta + y_0\sin\phi\sin\theta + z_0\cos\theta \\ & + \sqrt{(x_0\cos\phi\sin\theta + y_0\sin\phi\sin\theta + z_0\cos\theta)^2 + (a^2 - x_0^2 - y_0^2 - z_0^2)} \end{aligned} \tag{3.5}$$

It is obvious that at $r_0 = 0$, $\rho(\theta, \phi) = a$. Again, one can analytically prove that, at $r_0 = 0$, $\dfrac{\partial S}{\partial x_0} = \dfrac{\partial S}{\partial y_0} = \dfrac{\partial S}{\partial z_0} = 0$. Derivations of second derivatives are shown in Appendix E. How

the radius R is chosen is further described in the Results section.

3.2.4 Quantification of the effective magnetic moment

The 3D integral form in Eq. 3.1 implies that the summed MR signal from an arbitrary shell depends only on the moment p and spin density ρ_0. If we choose a shell formed by two concentric spheres with radii $R_1 > R_2$, then the MR signal of the shell is $S_1 - S_2$, which satisfies

$$\frac{9\sqrt{3}}{4\pi\rho_0}(S_1 - S_2) = \tag{3.6}$$
$$R_1^3 \int_1^{R_1^3/R_2^3} \frac{dx}{x^2}(2e^{ixp/R_1^3} + e^{-2ixp/R_1^3}) + \int_{-1}^{2} \frac{dx}{x^2}[2 - (2-x)\sqrt{1+x}](R_1^3 e^{-ixp/R_1^3} - R_2^3 e^{-ixp/R_2^3})$$

where S_1 and S_2 are the MR complex signals calculated from their corresponding radii R_1 and R_2. In order to derive Eq. 3.6, the following identity is used so no singularity is created in the integrands.

$$\int_{-\lambda}^{2\lambda} \frac{dx}{x^2}\left[(2-x)\sqrt{1+x} - \left(2 - \frac{x}{\lambda}\right)\sqrt{1+\frac{x}{\lambda}}\right] e^{-igx} =$$
$$\int_{-\lambda}^{2\lambda} \frac{dx}{x^2}\left[(2-x)\sqrt{1+x} - 2\right] e^{-igx} + \int_{-\lambda}^{2\lambda} \frac{dx}{x^2}\left[2 - \left(2 - \frac{x}{\lambda}\right)\sqrt{1+\frac{x}{\lambda}}\right] e^{-igx} \tag{3.7}$$

In theory, Eq. 3.6 itself seems sufficient to solve the two unknowns (p and ρ_0) from a complex shell signal. However, our experience reveals that a calculation utilizing only the imaginary part of Eq. 3.6 can lead to an inaccurate determination of the effective magnetic moment. This may be due to a lack of the first order imaginary term when one expands Eq. 3.6 into a Taylor series in p. Thus we use three concentric spheres to quantify the magnetic moment. Assume that the radii of the three arbitrary spheres satisfy

$R_1 > R_2 > R_3$. Their corresponding MR complex signals are S_1, S_2, and S_3. We can solve the magnitude of p from

$$Re(S_1 - S_2)Re(f_{23}) - Re(S_2 - S_3)Re(f_{12}) = 0 \tag{3.8}$$

where we define $Re(f_{ij})$ as

$$Re(f_{ij}) \equiv Re\left(\frac{9\sqrt{3}}{4\pi\rho_0}(S_i - S_j)\right) \qquad \text{with } i, j = 1, 2, 3 \tag{3.9}$$

and where S_is appearing in Eq. 3.8 are the complex signals directly taken from images, but Eq. 3.9 is calculated using the theoretical formula in Eq. 3.6 or its alikeness. The magnetic moment p is the only unknown in Eq. 3.8. Since we only use the real parts in Eq. 3.8 to solve the magnetic moment, we can only determine $|p|$. After that, we can compare the imaginary part of $S_1 - S_2$ (or $S_2 - S_3$) to the right hand side of Eq. 3.6 but with p replaced by $|p|$. If the imaginary part of the signal is above the thermal noise (depending on the choices of R_is) and if the Gibbs ringing effect due to the object can be neglected, this comparison can determine the sign of p.

The optimal choices of the three radii will be determined when the uncertainty of p is minimized and discussed in the next subsection. This can be done by rewriting $Re(f_{ij})$

$$\begin{aligned} & Re(f_{ij}) \qquad\qquad (3.10) \\ = \;& \frac{p}{\phi_i}\int_1^{\phi_j/\phi_i}\frac{dx}{x^2}[2\cos(x\phi_i) + \cos(2x\phi_i)] \\ + \;& \int_{-1}^{2}\frac{dx}{x^2}[2 - (2-x)\sqrt{1+x}]\left[\frac{p}{\phi_i}\cos(x\phi_i) - \frac{p}{\phi_j}\cos(x\phi_j)\right] \end{aligned}$$

where we define ϕ_i as

$$\phi_i \equiv p/R_i^3 \qquad \text{with } i = 1, 2, 3 \tag{3.11}$$

As each ϕ_i turns out to be a phase value on the equatorial plane of the object (see the argument in the exponential function on the left hand side of Eq. 3.1), a choice of R_i leads to a rough estimation of p. In order to avoid the dephasing and the phase aliasing effect, we can choose R_3 sufficiently large such that $|p|/R_3^3$ is less than π. On the other hand, we want to keep R_1 small enough such that ρ_0 within the radius R_1 is approximately a constant. These two considerations indicate that $|p|$ is between 0 and πR_3^3. The Van Wijngaarden-Dekker-Brent method [19] can be used to numerically solve $|p|$. The mean value theorem of integral calculus refers to that the root of a function is unique in a given range when the derivative of the function is not zero in that entire range. As the derivative of Eq. 3.8 with respect to p is the denominator D in Eq. 3.12 in uncertainty calculations, for a meaningful result of p between 0 and πR_3^3, the value of D cannot be zero. Thus the solution of $|p|$ from Eq. 3.8 is unique.

3.2.5 Uncertainties of the effective magnetic moment

As described earlier, the inevitable sources of uncertainties and errors are from the thermal noise and systematic noise. These two noise sources are uncorrelated. We can analytically formulate the overall uncertainty from Eq. 3.8 through the error propagation method [18]. The basic concept is to calculate the first derivative of the real part of Eq. 3.6 and its counter part of $Re(S_2 - S_3)$. The uncertainty of p, δp, in percentage is

$$\frac{\delta p}{|p|} = \frac{1}{|D|}\sqrt{(\delta[Re(S_2 - S_3)])^2\frac{(Re(f_{12}))^2}{p^2} + (\delta[Re(S_1 - S_2)])^2\frac{(Re(f_{23}))^2}{p^2}} \tag{3.12}$$

where

$$D = Re(S_1 - S_2)Re\frac{\partial f_{23}}{\partial p} - Re(S_2 - S_3)Re\frac{\partial f_{12}}{\partial p} \tag{3.13}$$

$$\begin{aligned} & Re\frac{\partial f_{ij}}{\partial p} \\ = & -2\int_1^{\phi_j/\phi_i} \frac{dx}{x}[\sin(x\phi_i) + \sin(2x\phi_i)] \\ + & \int_{-1}^{2} \frac{dx}{x}[2 - (2-x)\sqrt{1+x}][\sin(x\phi_j) - \sin(x\phi_i)] \end{aligned} \tag{3.14}$$

In the above derivation, we have assumed no correlation between $S_1 - S_2$ and $S_2 - S_3$. Their variances are

$$(\delta[Re(S_i - S_j)])^2 = [\epsilon_{ij}Re(S_i - S_j)]^2 + \frac{4\pi}{3}\sigma^2(R_i^3 - R_j^3)\Delta x\Delta y\Delta z \tag{3.15}$$

where ϵ_{ij} is the systematic error in percentage and is calculated by neglecting the thermal noise (i.e., infinite SNR). The voxel volume is $\Delta x\Delta y\Delta z$. If the systematic noise can be neglected, Eq. 3.12 is proportional to $\sqrt{\Delta x\Delta y\Delta z}/(\mathrm{SNR}\sqrt{|p|})$ and the rest only depends on ϕ_i defined in Eq. 3.11. As we have limited each ϕ_i between 0 and π, for any given image resolution, SNR, and the effective magnetic moment of the object, we can numerically determine the minimal value of $\delta p/|p|$ in Eq. 3.12 by varying ϕ_i. The optimal combination of (ϕ_1, ϕ_2, ϕ_3) provides a guidance of how to choose radii of the three concentric spheres. Due to discrete voxels, precise values of radii are not required in our approach. In our estimation of the uncertainty, we have assumed that the center of the object is correctly identified, even though this is not completely true.

3.2.6 Resolving the magnetic susceptibility and volume of the object individually

One way to determine susceptibility (or g) is to measure the volume of the object from spin echo images and then calculate $\Delta\chi$ (or g) from the magnetic moment, as $g = p/a^3$. However, this approach is valid only when the object has no spin density ($s_c = 0$) and if the dephasing effect due to $\Delta\chi$ through sampling in the spin echo images can be neglected. The latter condition may be satisfied by increasing the image resolution, but at the expense of SNR and imaging time. Consider the real part of the MR signal S_{SE} from an arbitrarily uniform volume V that encloses the entire object on spin echo images

$$S_{SE} = \rho_{0,SE}(V - V_0) \equiv \rho_{0,SE}\left(V - \frac{4\pi}{3}a^3\right) \tag{3.16}$$

where $\rho_{0,SE}$ is the effective spin density (a constant) around the object in the spin echo images. With two arbitrary volumes V_1 and V_2 such that V_2 is completely enclosed by V_1, $\rho_{0,SE}$ and the volume of the object $V_0 = 4\pi a^3/3$ can be determined from

$$\begin{aligned} S_{1,SE} &= \rho_{0,SE}(V_1 - V_0) = \rho_{0,SE}(V_1 - V_2) + \rho_{0,SE}(V_2 - V_0) \\ S_{2,SE} &= \rho_{0,SE}(V_2 - V_0) \end{aligned} \tag{3.17}$$

which leads to

$$V_0 = (S_{1,SE}V_2 - S_{2,SE}V_1)/(S_{1,SE} - S_{2,SE}) \tag{3.18}$$

As the signals $S_{1,SE} - S_{2,SE}$ and $S_{2,SE}$ are uncorrelated and their thermal noises are proportional to the square root of number of voxels, the uncertainty of the object volume can

be derived from the error propagation method [18]

$$\delta V_0 = \frac{\sqrt{\Delta v}}{\mathrm{SNR}_{\mathrm{SE}}} \sqrt{V_2 + \frac{(V_2 - V_0)^2}{V_1 - V_2}} \tag{3.19}$$

where Δv is the voxel volume of the spin echo images and $\mathrm{SNR}_{\mathrm{SE}}$ is the SNR in the spin echo images. In order to minimize the uncertainty, it is obvious that the volume $V_1 - V_2$ should be chosen as large as possible before heterogeneity is encountered in the images, while the volume V_2 should be chosen as small as possible but still larger than the object. In fact, in order to estimate the volume of the object more accurately, V_2 has to be larger than the volume covering both the distorted object and voxels due to its shifted image intensity in the spin echo image. In our analyses, for simplicity, we have used the magnitude part of the spin echo images rather than the real part.

3.2.7 Phantom studies

We prepared three gel phantoms with different sizes of spherical glass beads and imaged them with a 1.5 T MR machine (Siemens Sonata) at different echo times for the validation of our method. We measured the diameter of each glass bead ten times with a vernier caliper. We mixed 107 g of gelatin powders into 1200 ml distilled water for each phantom. After placing a glass bead on the top of a solidified gel layer in a container, we poured more gelatin solution into the container. This process was repeated until two or three beads were embedded in each gel phantom. The first phantom contained two glass beads of diameters 3 mm and 5 mm and a hollow straw (see Fig. 3.2). The straw served as a reference such that the absolute magnetic susceptibility of the gel was validated as that of water, -9.05 ppm in SI units [8]. Coronal images of a multiple echo

3D gradient echo sequence and of a 3D turbo spin echo sequence were acquired. The imaging parameters of the gradient echo sequence for the first phantom were $T_E = 5$ ms, 10 ms, 15 ms, and 20 ms, $T_R = 25$ ms, flip angle $15°$, resolution 1 mm $\times$ 1 mm $\times$ 1 mm, field of views 256 mm $\times$ 256 mm $\times$ 96 mm, and read bandwidth 610 Hz per pixel (Hz/pixel) for $T_E = 5$ ms and 220 Hz/pixel for the other three echo times. The scan time for the gradient echo sequence was 615 sec. Imaging parameters of the 3D spin echo sequence were $T_E = 71$ ms, $T_R = 600$ ms, flip angle of the refocusing pulse $160°$, turbo factor 25, resolution 1 mm $\times$ 1 mm $\times$ 1 mm, field of views 256 mm $\times$ 256 mm $\times$ 96 mm, read bandwidths 610 Hz/pixel, actual phase encoding lines 275, actual partition encoding steps 112, and the scan time was 740 sec for this spin echo sequence. The second phantom contained

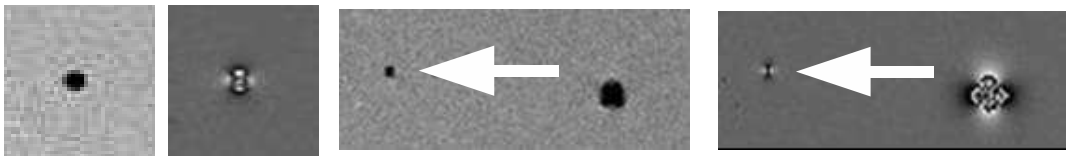

(a) (b) (c) (d)

Figure 3.2: (a) The magnitude and (b) its associated phase image show a 5 mm glass bead in the coronal view acquired at echo time 10 ms from a 1.5 T MR machine. (c) The magnitude image and (d) its associated phase image show a 3 mm glass bead (pointed by the white arrow) and the cross session of an air straw. The 1.5 T MRI machine adopts the right-handed convention. Note the somewhat opposite phase patterns outside the bead and the air straw. The main field direction is along the up-down direction of each image.

two beads of diameters 2 mm and 6 mm. The parameters of the gradient echo sequence for the second phantom were identical to the above parameters, except that the number of slices was 72 and the read bandwidth was 350 Hz/pixel for all four echoes. The use of different read bandwidths was to test whether this imaging parameter would affect our quantitative method. A circular polarized radiofrequency (rf) head coil was used to image the first two phantoms.

In order to study the effect of the magnetic moment measurement due to heteroge-

neous image intensity, we placed another set of 2 mm, 3 mm, and 5 mm beads in the third gel phantom and imaged the phantom with an 8-channel rf coil. Imaging parameters of the 3D gradient echo sequence were mostly the same as those stated above, except that the number of slices was 64, the read bandwidth was 350 Hz/pixel for all four echoes, and two averages were used for this scan. We acquired both the combined magnitude images (using the sum-of-squares method for reconstruction) and original k-space data from each channel. The magnetic moments quantified from single channel k-space data were compared with the moments obtained from the combined magnitude images but with phase images from single channels.

To remove the background field in phase images, we first chose a volume-of-interest (VOI) within the phantom and around each bead. Manual phase unwrapping followed by a 3D second order polynomial fitting were performed within each VOI. The dimension of a VOI along each independent direction was about 3-4 times of the diameter of the bead. In addition, each VOI also excluded certain voxels nearby each bead, as those voxels contained measurable phase information from the bead itself. After the fit, we subtracted the polynomial from the original phase images and thus removed the unwanted background field around each bead.

3.2.8 Magnetic moment measurements by SQUID

Absolute magnetic moments of the 2 mm, 3 mm, 5 mm, and 6 mm glass beads from the first two phantoms were also measured with a SQUID based magnetometer (Quantum Design MPMS-5S), at fields between 0.5 T and 5.0 T in intervals of 0.5 T. At each field strength, the magnetic moment of each bead was measured 10 times and the averaged value and standard deviation of the magnetic moment were obtained. The measurements

at 1.5 T were compared to results derived from our CISSCO method.

Except for the 2 mm glass bead, each bead was placed inside a straw that was mounted to the magnetometer for measurements. The 2 mm bead was placed inside a capsule and then was fixed inside the straw by a cotton ball. The magnetic moments of the experimental setups without beads were also measured and were subtracted from the measurements with beads. After the absolute magnetic moment of each bead was measured, the absolute susceptibility was calculated from the magnetic moment divided by 1.5 T and by the volume of each bead (V_0 in Table 3.4). We compare the susceptibility values between SQUID and MRI.

3.3 Results

3.3.1 Numerical simulations

In general, the numerical errors from simulations are small. The numerical error of the real part of the complex signal in Eq. 3.1 is no more than 0.3%, while the numerical error of the imaginary part of the complex signal in Eq. 3.1 is between 0.2% to 0.3%. These results indicate that under infinite image resolution, our theoretical derivations agree well with numerical calculations.

After the proper reconstruction of 32^3 images with different small spherical objects, without adding the thermal noise, for most cases, we have found that the real part of the total complex signal from either a sphere or a shell is within 3% of the theoretical value given by Eq. 3.1 or Eq. 3.6. However, the imaginary part of the total signal or phase can deviate from the theoretical value by 100%. Such a large error is due to the point spread function of the object or due to the lack of the first order term of the magnetic moment. As long as the real part is used in the quantification of the magnetic moment, such a

large error due to the imaginary part or phase of the signal does not seem to lead to any inaccurate quantification.

3.3.2 Identification of the object center

Among the three possible procedures of identifying the object center, we have found that the sole use of the imaginary part of the MR signal does not lead to an accurate determination. As a result, the phase approach fails. For the procedure of using a shell to determine the object center, the second derivatives of the real part of the signal S with respect to all directions have to be negative. However, from numerical evaluations of the equations provided in Appendix D, this will occur only when ϕ_1 and ϕ_2 are certain values. This result suggests that using a shell is not a robust procedure to determine the center of the object. We also confirm that from our simulations.

The best procedure of identifying the object center is to use the one sphere approach. When the real part of the signal is minimized by moving the sphere around the object, the object center is determined. In this approach, the second derivatives of the real part of the signal S with respect to all three directions have to be positive. From numerical evaluations of the equations in Appendix E, these conditions can be satisfied when ϕ_R is less than roughly 2.1 radians. On the other hand, the radius R should not be chosen larger than a radius whose ϕ_R is less than 0.1 radian, as such a choice can lead to insensitive results of second derivatives. We suggest to choose a radius R with the corresponding ϕ_R between 1 and 2 radians, if possible. As a rough value of ϕ_R can be estimated from certain pixels on the equatorial plane in phase images, the magnetic moment p can also be estimated from $\phi_R R^3$. With the one sphere approach and the implementation of a downhill simplex program from [19], it typically takes our Pentium 4 roughly 20 seconds

to identify the center of an object with $p < 30$ radian $\cdot$ pixel^3.

From our numerical simulations, the identified center of each object is within 0.3 voxel of the actual center, whether the thermal noise has been added into the images or not. A 0.3 voxel deviation away from the actual center is relatively large and it occurs when centers of objects have been purposely shifted by 0.4 voxel in either or all three directions. However, even in those situations, the quantified magnetic moments of the objects are still accurate (i.e., within the uncertainties estimated by Eq. 3.12).

3.3.3 Measurements of the magnetic moment: simulation results

We first want to determine the three optimal radii used for the quantification of the magnetic moment. This can be found by minimizing the uncertainty of the magnetic moment in Eq. 3.12. By neglecting the systematic errors ϵ_{ij}, we have found that (ϕ_3, ϕ_2, ϕ_1) are best in the range of (π-2.6, 1.0-0.7, ≤ 0.1) radians. A choice of R_2 with a corresponding phase value of $\phi_2 \approx 0.9$ radian would provide a slightly lower uncertainty. Given these phase ranges and Eq. 3.11, R_1 may be chosen as roughly $3R_3$. Similarly, R_2 may be chosen as roughly $1.4R_3$ or $0.5R_1$. None of these three radii needs to be a multiple integer of a pixel. The ranges of ϕ_is also imply that R_1 can be chosen as large as possible but should not be too large to include significant phase values from any nearby objects. The radius R_3 can be chosen as small as possible but larger than phase aliasing areas around the object. We typically choose the three radii within these ranges of ϕ_i values. However, in order to reduce systematic errors due to the Gibbs ringing effects, our studies show that it is better to choose R_3 at least half a pixel away from the surface of the object. In addition, the difference between each R_i is better to be at least one pixel. These two rules of choosing radii for moment measurements supersede the above selection rules.

We follow all these rules and list results in Tables 3.1 and 3.2. Nonetheless, if these two rules are used, particularly for objects with small magnetic moments or phase values, it is obvious that the above simple relations between the three radii for minimizing uncertainty due to the thermal noise may not be met.

Quantified magnetic moments of simulated objects at four different echo times with and without thermal noise added into images are shown in Table 3.1. The listed phase values (third column) in Table 3.1 are measured from the equatorial plane of each object at their corresponding radii (second column). Due to discretized MR voxels and averaged MR complex signal within each voxel, a phase value measured from each voxel may not agree with the actual phase value (p/R^3). As given by the theory, the measured magnetic moments appear to be proportional to the echo time T_E. In all eight cases, the maximal uncertainty (one standard deviation) of the measurement is no more than 6% of the actual magnetic moment. The difference between the measured magnetic moment and the actual moment for any case (except for one) is less than the uncertainty calculated from Eq. 3.12.

3.3.4 Measurements of the magnetic moment: phantom results

Table 3.2 lists the quantified magnetic moments of four glass beads at four different echo times. Most uncertainties calculated from Eq. 3.12 are less than 20%. Even though in most cases the effective magnetic moments of glass beads are larger than those values used in simulations, as ϕ_3 in most cases are not close to the ideal value, the uncertainties in Table 3.2 are usually larger than those shown in Table 3.1. While the exact magnetic moment of each glass bead is not known in advance, Table 3.2 has shown that the magnetic moment of each bead is proportional to the echo time (and independent of the read

T_E	radii	phase	p_{ideal}	w/o thermal noise		w/ thermal noise	
(ms)	(pixel)	(radian)	(rad $\cdot$ pixel^3)	p	$\delta p/p$ (%)	p	$\delta p/p$ (%)
5	(1.5, 2.5, 3.5)	(1.56, 0.58, 0.16)	6.69	7.11	5.5	6.81	6.0
10	(1.8, 2.8, 4.0)	(2.42, 1.26, 0.20)	13.4	13.5	2.5	13.4	3.2
15	(2.1, 3.1, 5.0)	(1.78, 0.64, 0.16)	20.1	20.4	1.8	20.3	2.5
20	(2.4, 3.4, 5.0)	(2.23, 0.89, 0.22)	26.8	26.9	1.1	26.8	2.0

Table 3.1: Magnetic moments quantified from simulated images at four different echo times with and without simulated thermal noise. The first column lists the echo time. The second column lists three radii used in Eq. 3.8 to solve p. The third column lists their corresponding phase values directly measured from images. These values are different from p/R_i^3, as explained in the text. The fourth column lists $p_{ideal} \equiv \gamma \Delta\chi B_0 T_E a^3/3$. The fifth and seventh column list quantified p values. The sixth and eighth column list the uncertainty of p calculated from Eq. 3.12. The uncertainty in the sixth column only includes the discrete error, but that in the eighth column includes both thermal and discrete noise. All quantified magnetic moments except for one agree with ideal values within 5% of the ideal values. The differences between quantified values and ideal values are properly covered by the uncertainties calculated from Eq. 3.12.

bandwidth) within estimated uncertainties. However, one exception occurs for the 6 mm bead at $T_E = 5$ and 20 ms. Our further investigations have ruled out most possibilities and hence suggested that at $T_E = 5$ ms, poor eddy current compensations result in residual unwanted phase in the original phase images. At $T_E = 20$ ms, as the phase induced from the bead extends to the largest area, residual background phase from the phantom itself has made some influences. In both cases, the second order polynomial fit did not seem to completely remove the unwanted background phase in images. Fig. 3.3 shows the plot of the quantified magnetic moments of four glass beads as a function of $0.5\gamma\!\!\!^{-}B_0 T_E V_0$, where $\gamma\!\!\!^{-}$ is $\gamma/2\pi$, MHz/T. The slope of each fitted line is the magnetic susceptibility of the glass bead. For the 6 mm glass bead, after excluding the magnetic moment at $T_E = 5$ ms, the slope of the fitted line, Fig. 3.3(d), is -1.76 ± 0.05 and the intercept of this line is 2.90 ± 2.75.

Results from the 8-channel coil are shown in Table 3.3. As the magnitude intensity around the background of each bead does not vary too much, the results from the com-

	Diameter 2 mm					Diameter 3 mm					
T_E	radii	p	δ	ϵ_{12}	ϵ_{23}	radii	p	δ	ϵ_{12}	ϵ_{23}	
(ms)	(mm)	(rad · mm^3)	(%)			(mm)	(rad · mm^3)	(%)			
5	(1.5, 2.5, 3.5)	−1.28	45	0.001	0.010	(2.0, 3.0, 4.0)	−5.54	15	0.004	0.014	(a)
10	(1.5, 2.5, 3.5)	−3.05	21	0.001	0.026	(2.0, 3.0, 4.0)	−10.45	11	0.005	0.040	
15	(1.5, 2.5, 3.5)	−4.90	13	0.001	0.040	(2.0, 3.0, 4.0)	−14.71	6	0.008	0.040	
20	(1.5, 2.5, 3.5)	−6.48	7	0.001	0.034	(2.0, 3.0, 4.5)	−18.24	2	0.005	0.019	

	Diameter 5 mm					Diameter 6 mm					
T_E	radii	p	δ	ϵ_{12}	ϵ_{23}	radii	p	δ	ϵ_{12}	ϵ_{23}	
(ms)	(mm)	(rad · mm^3)	(%)			(mm)	(rad · mm^3)	(%)			
5	(3.0, 4.0, 5.0)	−20.93	8	0.003	0.013	(3.5, 4.5, 6.0)	−26.39	3	0.003	0.001	(b)
10	(3.0, 4.0, 5.8)	−40.41	5	0.004	0.033	(3.5, 4.5, 6.7)	−62.67	2	0.004	0.015	
15	(3.0, 4.2, 6.7)	−57.94	1	0.004	0.008	(3.5, 4.7, 7.7)	−92.16	1	0.001	0.015	
20	(3.1, 4.4, 7.4)	−76.05	1	0.003	0.014	(3.5, 5.0, 8.6)	−127.00	1	0.002	0.032	

Table 3.2: Magnetic moments of glass beads 2 mm, 3 mm, 5 mm and 6 mm at four different echo times were measured by the CISSCO method. The first column lists the echo time. The second and seventh column list the values of three radii (in units of mm or pixel) used in Eq. 3.8 to solve for each magnetic moment. The third and eighth column list quantified magnetic moments. The fourth and ninth column show the uncertainties of magnetic moments (in percentage). The uncertainties are calculated from Eq. 3.12, including both thermal noise and systematic noise. The fifth, sixth, tenth, and eleventh column list uncertainties of systematic noise calculated from simulations. The SNR of the images at four different echo times is about 13:1. Quantified magnetic moments per echo time for each bead agree with each other within two standard deviations of the uncertainties, except for the 6 mm bead measured at $T_E = 5$ ms. Half of the overall estimated uncertainties are no more than 5%.

bined channel for each bead also agree with the results from the single channel. The SNR used in Eq. 3.12 can take into account intensity variations in magnitude images and, in the worst case, the SNR can be chosen as 1:1. The results from the 8-channel coil are also consistent with those shown in Table 3.2, but we notice that for the 5 mm bead, the magnetic moments in Table 3.3 are roughly 9% lower than those listed in Table 3.2. Measuring the diameter of the second bead (used in the third phantom), we find a diameter of 4.98 ± 0.04 mm. While this value is still consistent with the diameter shown in Table 3.4, this slight reduction of the diameter leads to a 3% reduction in volume and thus in the magnetic moment measurements. The remaining 6% differences between the two sets of measurements could be due to the susceptibility difference between the two 5 mm beads,

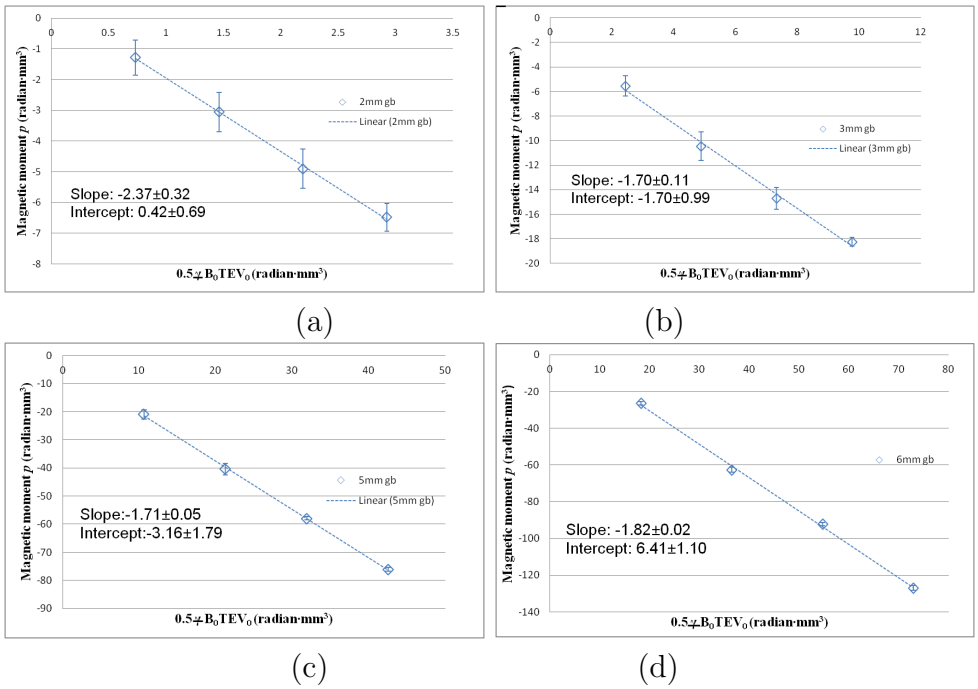

Figure 3.3: The linear fit between the magnetic moment and $0.5\gamma B_0 T_E V_0$ is given in the chart. (a) diameter 2 mm glass bead (b) diameter 3 mm glass bead (c) diameter 5 mm glass bead and (d) diameter 6 mm glass bead

or due to the lack of quality assurance checks on the clinical MR machine, since the third phantom was scanned several months behind the first two phantoms.

3.3.5 Estimations of object volumes

When an object such as a glass bead produces no signal in MRI, the volume of the object and its uncertainty can be calculated from spin echo images, based on Eq. 3.18 and Eq. 3.19. With an SNR of 30:1 in the spin echo images, the measured volumes and associated uncertainties are shown in Table 3.4. Table 3.4 also lists the mean diameter and its associated standard deviation of each glass bead measured from a vernier scale. The difference between the volume measured from spin echo images and that from the vernier scale is within 5% for any glass bead.

	Diameter 2 mm				Diameter 3 mm				Diameter 5 mm			
T_E	p_{SS}	$\delta p/p$	p_{ch}	$\delta p/p$	p_{SS}	$\delta p/p$	p_{ch}	$\delta p/p$	p_{SS}	$\delta p/p$	p_{ch}	$\delta p/p$
(ms)	(rad · mm^3)	(%)	(rad · mm^3)	(%)	(rad · mm^3)	(%)	(rad · mm^3)	(%)	(rad · mm^3)	(%)	(rad · mm^3)	(%)
5	1.69	35	1.85	29	4.80	26	5.04	24	18.92	13	19.20	13
10	3.90	17	4.17	15	9.76	17	9.72	17	37.48	8	37.35	8
15	5.42	14	5.47	14	14.59	8	14.70	8	53.74	1	53.89	1
20	7.00	8	7.05	8	18.44	2	18.51	2	70.49	1	70.30	1

Table 3.3: Magnetic moments of glass beads 2 mm, 3 mm, and 5 mm at four different echo times quantified from combined 8-channel images and from single channel images. For single channel data, we use images reconstructed from k-space from one of the 8 channels. For combined data, we use the same phase images as those from the single channel, but for the magnitude part we use the multichannel (sum of squares) data. The first column lists the echo time. The second, sixth, and tenth column are quantified magnetic moments from the combined data. The fourth, eighth, and twelve column are the measured magnetic moments from the single channel data. The column following each quantified magnetic moment lists its associated uncertainty, which includes both thermal noise and systematic noise calculated from Eq. 3.12. The SNR of images at all four echo times is about 15:1. Quantified magnetic moments per echo time for each bead again agree with each other within two standard deviations of the uncertainties. Measurements between two different coils for each bead also have good agreements.

3.3.6 SQUID measurements

The results from SQUID measurements in general agree with those from the CISSCO method. The absolute magnetic moments averaged from 10 SQUID measurements at 1.5 T are $(-6.09 \pm 0.062) * 10^{-8}$ A·m^2, $(-1.97 \pm 0.0087) * 10^{-7}$ A·m^2, $(-8.06 \pm 0.27) * 10^{-7}$ A·m^2, and $(-1.52 \pm 0.00068) * 10^{-6}$ A·m^2, for the 2 mm, 3 mm, 5 mm, and 6 mm bead, respectively. The absolute susceptibility of each glass bead is calculated from the absolute magnetic moment and is listed in Table 3.5. Although the standard deviations of these magnetic moments are small or negligible, the actual uncertainties from SQUID measurements are large. For example, when the same beads were measured by SQUID on a different day, the measured magnetic moments were roughly 16%, 17%, 6%, and 16% deviated from the above values for the 2 mm, 3 mm, 5 mm, and 6 mm bead, respectively. These deviations are likely due to environmental background noise caused by nearby electrical circuits that is difficult to shield. In addition, the magnetic moment of the capsule and

Diameters of glass beads (mm)	V_1 (mm^3)	V_2 (mm^3)	V_0 (mm^3)	V_0 (mm^3)	Diff %
2.06 ± 0.05	320	57	4.4 ± 0.3	4.6 ± 0.3	4.3
3.08 ± 0.02	440	63	15.2 ± 0.3	15.3 ± 0.3	0.6
5.03 ± 0.10	1536	199	67.3 ± 0.4	66.6 ± 4.0	1.0
6.02 ± 0.10	1678	378	109.0 ± 0.8	114.2 ± 5.7	4.5

Table 3.4: The volume estimations of glass beads imaged by a spin echo sequence. The first column lists the diameters of glass beads measured by a vernier caliper. The second column lists the pseudo volume V_1. The third column lists the pseudo volume V_2. The fourth column shows the estimated volume V_0 from spin echo images. The fifth column is the calculated volume based on the first column. The sixth column is the difference in percentage between V_0 and V_0. Accurate volume measurements of beads without MR signal can be obtained from spin echo images.

cotton ball is roughly 9 times of the magnetic moment of the 2 mm bead. These facts imply that the actual error of SQUID measurements is probably about $3 * 10^{-8}$ A·m^2. The 16% difference from the 6 mm bead may be due to whether the glass bead was mounted slightly off the center of the magnetometer, as the bead was considered as an oversized object for our SQUID-based magnetometer.

In order to compare SQUID results to MR results, we need to add the absolute susceptibility of water, $\chi_{H_2O} = -9.05$ ppm, to the susceptibility values measured from MRI. This is because the susceptibility from MRI, $\Delta\chi$, is defined as $\chi_{gb} - \chi_{H_2O}$, where χ_{gb} is the absolute susceptibility of the glass bead. The calculated absolute susceptibility values of glass beads from MRI are also listed in Table 3.5. They agree with those measurements from SQUID within uncertainties.

3.4 Discussion

Our simulations and phantom studies have demonstrated that the CISSCO method can accurately quantify magnetic moments of small objects. The word “small is measured relatively to an image resolution on a particular MRI machine. For this reason and

Beads	MRI	MRI + water	SQUID
2 mm	-2.23 ± 0.32 ppm	-11.3 ± 0.3 ppm	-11.1 ± 0.7 ppm
3 mm	-2.01 ± 0.13 ppm	-11.1 ± 0.1 ppm	-10.8 ± 0.2 ppm
5 mm	-1.82 ± 0.11 ppm	-10.9 ± 0.1 ppm	-10.1 ± 0.7 ppm
6 mm	-1.68 ± 0.09 ppm	-10.7 ± 0.1 ppm	-11.2 ± 0.6 ppm

Table 3.5: Comparisons of magnetic susceptibility measurements between MRI and SQUID. The first column lists the diameters of glass beads. The second column lists calculated susceptibilities ($\Delta\chi$) from magnetic moments of glass beads obtained at $T_E = 15$ ms in Table 3.2 and from volumes V_0 in Table 3.4. The uncertainties of susceptibility values were calculated through the error propagation method. These are results from MRI. The third column lists the absolute susceptibility value of each bead, by adding -9.05 ppm (which is the absolute susceptibility of water) to each value shown in the second column. We assume no uncertainty of the water susceptibility value. The fourth column lists measured susceptibility of each bead from SQUID. Measurements between our CISSCO method from MRI and SQUID agree within uncertainties. However, different sizes of beads seem to have slightly different susceptibility values.

for fair comparison of results from different machines with different sequence parameters, it is better to use radian $\cdot$ pixel^3 as the unit for CISSCO measurements. In the following subsections, we will discuss certain issues related to the measurements of magnetic moments, susceptibility quantifications, and the background phase removal methods.

3.4.1 Quantifications of magnetic moments

Choices of the three radii

For a small object with a high susceptibility value (or a long echo time or a high field strength), the CISSCO method can reliably quantify a magnetic moment down to a few radian $\cdot$ pixel^3, as indicated in Table 3.1. On the other hand, for a relatively large object with a small susceptibility value (or a short echo time or a low field strength), the quantified magnetic moment can have a large uncertainty. First, we note that the choices of three concentric spheres with radii R_i will always lead to a solution from Eq. 3.8. However, due to insufficient phase information around the object of interest, R_is may not be optimal

values given at the beginning of Sec. 3.3.3 (when only the thermal noise is considered). Furthermore, in order to reduce any significant systematic errors due to discrete image pixels, R_3 (the smallest radius of choice) should be at least half a pixel away from the surface of the object and the radius between each R_i needs to be differed by one pixel. The larger the R_i is, the smaller the systematic error is. The choices of non-optimal R_is can lead to a larger uncertainty of the measured magnetic moment, due to the presence of the thermal noise. Some of such results can be seen in Table 3.2. Generally speaking, given the optimal ranges of R_is in Sec. 3.3.3, the phase value at the equatorial plane on the surface of the object (i.e., $|g| \equiv |p|/a^3$) is better to be at least 3 radians in order to obtain accurate results. This can be challenging for MRI studies if $\Delta\chi$ is too small.

Determination of the sign of a quantified magnetic moment

The phase term, $-p(3\cos^2\theta - 1)/r^3$, shown in Eq. 3.1 has a minus sign and this left-handed definition follows the convention in [26]. On the other hand, many MRI vendors (including ours) use the right-handed definition [27], which leads to a sign change in the phase term. As a result, quantified magnetic moment or susceptibility can also have a sign change. Thus, one should be careful about interpreting measurements from MR images and determine whether an object of interest is paramagnetic or diamagnetic to water. As an example, Fig. 3.2d shows phase distributions from a glass bead and from an air straw (in a cylindrical shape). As the glass bead is diamagnetic to water but air is paramagnetic to water, we see somewhat opposite phase patterns around those two objects. (Note that the air straw has a $\cos 2\psi$ phase distributions outside the straw, as it is a 2D object.)

One may think to determine the magnetism of an object by visually examining phase intensities appearing in images. This can be dangerous, as Fig. 3.1b and Fig. 3.1d clearly show different phase intensities and patterns of the same object, especially for phase values inside the object. A reliable way is to quantify the imaginary part of the sum from the CISSCO method, as describe in the above text.

No major effect due to a slightly shifted center of the object

Solving the magnetic moment from Eq. 3.8 takes no more than one second of the computer time. However, as stated above, it can take 20 seconds or longer on a Pentium 4 to determine the center of an object. In addition, the identified center may not be the actual center, due to the presence of noise in images. This can happen when phase values around the object are close to zero. As a result, the sum of the complex signal does not differ much using either the identified center or one of its neighboring subpixels. Visual inspections of the object centers are needed in those situations. As long as the identified center of the object is close to the true center, the quantified magnetic moment is also very close to its true value.

Comparisons between CISSCO and other methods

Due to discrete voxels, the phase outside the object of interest does not exactly follow the $1/r^3$ decay. This is the main reason why the least squares fit is not able to accurately determine the magnetic moment of a small object. The CISSCO method avoids this problem by summing up MR signals of neighboring voxels. For comparison, the magnetic moments measured by Bos et al. [23] using the least squares fit range from roughly

21.6 radian $\cdot$ pixel^3 to 359 radian $\cdot$ pixel^3. Those moments are sufficiently large and can be accurately quantified by CISSCO. For another comparison, recent work by Liu et al. [24] shows that mean magnetic moments of glass beads have been underestimated by at least 10%, using a susceptibility mapping method. Their mean magnetic moments of air bubbles were even much worse. On the other hand, we accidentally discover a small air bubble in images of the third phantom. The quantified volume of that air bubble is a little bit under 1 mm^3 and thus its uncertainty is over 20%. However, with this volume, the quantified susceptibility is about -9.26 ppm, compared to the ideal -9.4 ppm.

3.4.2 Susceptibility quantifications

Different beads showing slightly different susceptibility values

As the 3D second order polynomial fit may not effectively remove the background phase at the longest echo time for the 6 mm bead, which has widest phase distributions, we use results from $T_E = 15$ ms shown in Table 3.2 for the estimations of susceptibility values listed in Table 3.5. We are surprised that susceptibility values from different beads are slightly different, although those values still agree with each other within two standard deviations of the uncertainty. Perhaps those differences are realistic, due to possibly small contaminations during manufacturing processes, as we could imagine that different beads were made from different dewar or machines. Nonetheless, comparing the results of two different 5 mm beads shown in Table 3.2 and Table 3.3, and given the susceptibility results from Table 3.5, these results suggest that the CISSCO method has the accuracy to distinguish small changes between quantified magnetic moments.

A reason why the susceptibility cannot be solved from Eq. 3.1

After solving the magnetic moment p, one may think to use Eq. 3.1 to further solve the susceptibility of the object, when $s_c = 0$. Unfortunately this is not realistic, as explained here. With the help of Eq. 3.7, we can rewrite Eq. 3.1 to be

$$\begin{aligned} \frac{9\sqrt{3}}{4\pi\rho_0 R^3} S &= 2\int_1^{1/\lambda} \frac{dx}{x^2} e^{i\lambda g x} + \int_1^{1/\lambda} \frac{dx}{x^2} e^{-i2\lambda g x} \\ &+ \int_{-1}^{2} \frac{dx}{x^2} \left[2 - (2-x)\sqrt{1+x}\right] e^{-i\lambda g x} + \lambda \int_{-1}^{2} \frac{dx}{x^2} \left[(2-x)\sqrt{1+x} - 2\right] e^{-igx} \end{aligned} \tag{3.20}$$

Note that $\lambda g \equiv p/R^3$ and radius R is at our choice. If we consider a known p and a fixed R, but consider $\lambda \to 0$ (and thus $g \to \infty$), Eq. 3.20 clearly shows that the signal S quickly approaches to an asymptotic value. With the presence of noise in MR systems, this derivation suggests that Eq. 3.1 can only allow us to determine an upper bound of the object volume and thus the lower bound of the susceptibility (or g). For example, when a nanoparticle is smaller than an imaging voxel, we may accurately determine its magnetic moment with our CISSCO method, but are not able to determine its volume from Eq. 3.1.

3.4.3 Background phase removal methods

Problems of different methods

In this work, we use a 3D second order polynomial fit method to remove the background phase in phantom images. While such a polynomial fit is not perfect, at least it will not overcorrect phase values induced from glass beads. We have also tried to use a 32×32 high pass filter to remove the background field. When magnetic moments of beads are not large, the results from the high pass filter are about the same as those

shown in Table 3.2. However, when a magnetic moment is larger than 70 radian $\cdot$ pixel^3, such a high pass filter size will significantly reduce the quantified result. If we reduce the size of the high pass filter to, say, 16×16, such a high pass filter size cannot effectively remove the background phase distributions induced from the geometry of the phantom container at long echo times. Thus, for a uniform presentation of the scientific work here, we have chosen the polynomial fit over the high pass filter. A recent SHARP (Sophisticated Harmonic Artifact Reduction for Phase) method [28] is also not suitable for us, as the theory behind that method requires only a spherical surface, but the method sums up phase values within a spherical volume. If the volume has included an object or has cut through an object, then the theory is violated. In addition, the spherical kernel used in SHARP should be large enough in order to mimic a perfect sphere. However, such a choice will remove pixels close to the boundary of the phantom container but we need those pixels for phase induced from beads at long echo times.

Future work

In reality, even if we can completely remove the unwanted background field, an object of interest can still be affected by the magnetic field produced from a nearby tissue. If we can approximate that field as a local uniform field around the object, then the absolute value of Eq. 3.6 may be used to solve p. The procedure of identifying the object center will need to be modified as well. These should be considered before the CISSCO method can be applied to $in\ vivo$ images. On the other hand, a constant background phase globally appearing in a uniform phantom can be usually removed by a high pass filter, which does not appear to alter the susceptibility of a small object [7].

3.5 Conclusion

We have developed and demonstrated that the CISSCO method can accurately quantify magnetic moments of several small objects from standard 3D gradient echo MR images. Our method has three advantages. First, we can reliably quantify the effective magnetic moment as low as a few radian $\cdot$ pixel^3. This means that the radius of the object can be much smaller than a pixel. Second, the uncertainty of each measurement from CISSCO is reduced by summing up voxels around the object. The uncertainty can be further reduced if the echo time can be increased without losing SNR. Third, as a result, the quantified magnetic moment or susceptibility of the object can be accurate within 10% and sometimes within 5% of the true value for practical applications and within reasonable imaging time. We have demonstrated those results with simulations and phantom studies. Our next goal is to apply the CISSCO method to $in\ vivo$ small objects such as microbleeds in the brain or nanoparticles labeling cells.

Chapter 4

AN IMPROVED METHOD FOR SUSCEPTIBILITY AND RADIUS QUANTIFICATION OF CYLINDRICAL OBJECTS FROM MRI

4.1 Introduction

The magnetic susceptibility of *in-vivo* objects can reveal the property of the objects or physiological information. For example, the susceptibility of blood is affected by the oxygen saturation level [29, 12, 13]. Therefore, measuring oxygen saturation may provide important clinical diagnostic information. Several research groups [13, 14, 30, 15] have tried to measure the susceptibility of blood. Lai et al. [14] and Langham et al. [30] have quantified the susceptibility of blood in large veins by using the phase information inside veins. On the other hand, Sedlacik et al. [15] has used a general fitting method to extract the size of a vein, its magnetic susceptibility, and other variables, from a 20-echo gradient echo MR sequence. As a result, the latter approach will require a much longer than usual scan time. Recently, the susceptibility of veins has been quantified by quantitative susceptibility mapping (QSM) techniques from different groups [31, 32, 33, 34, 35, 36, 37, 38, 39, 40, 41, 42, 43, 44]. In general, QSM techniques may be divided into two major categories. One is an inverse method [33, 34, 35, 36, 37, 38, 39]. The other is a constrained regularization approach [39, 40, 41, 42, 43, 44]. The inverse method may underestimate susceptibility values in small objects (whose diameters are less than 4 pixels) [40, 35, 38]. The constrained regularization approach may underestimate or overestimate the true susceptibility (as we will show later) and may take time to generate just one set of susceptibility maps. In addition, the intrinsic uncertainty of QSM methods has not been studied rigorously.

In this paper, we introduce a method that requires only one or two echo times from a standard gradient echo sequence for most $in\text{-}vivo$ cylindrical objects and can quantify the susceptibility and cross-sectional area of a narrow cylinder for most orientations (except for the magic angle). For most biological tissues, as magnetic susceptibility of an object is roughly known in advance, using one or two echoes can significantly reduce the possible solutions of susceptibility values and obtain a unique answer. Our previous work [8] has demonstrated how to quantify the effective magnetic moment and susceptibility of a narrow cylinder, with no MR signal inside the cylinder. This paper will focus on the quantifications of susceptibility and cross-sectional area from any given cylindrical object $with\ an\ MR\ signal$.

Our method relies on equations solved with known imaging parameters. In general, we quantify the following unknowns in sequence: orientation θ, effective magnetic moment $\wp$, spin density outside the object ρ_0, susceptibility $\Delta\chi$, radius of the object a, and spin density of the object $\rho_{0,c}$. We only need three concentric circles around a given cylindrical object for these quantifications. We will review the complex signal induced from a cylinder in the next section. Section 4.2.2 shows how to systematically obtain the susceptibility and object size from a cylindrical object at an arbitrary orientation, except for the parallel ($\theta = 0°$) and magic angle ($\theta = 54.7°$) orientations. Section 4.2.3 explains how to solve the susceptibility of an object when it is parallel to the main field. The magic angle orientation will be discussed later in section 4.2.4. Uncertainties of susceptibility and other unknowns will be studied through the error propagation method [18] in section 4.2.5, and relevant formulas will be provided in F and G. Sections 4.2.6, 4.2.7, and 4.2.8 describe procedures and post-processing steps of our simulations, phantom, and human studies.

Our results and comparisons to two QSM methods will be shown in section 4.3. Factors affecting the accuracy and precision of susceptibility quantifications based on our method will be discussed in sections 4.4.1 and 4.4.3 . In addition, as multiple solutions of susceptibility from our equations may occur, we comment on how to reduce possible solutions in section 4.4.2. Finally, we will discuss the limitations of our method and future work in section 4.4.4.

4.2 Methods and materials

4.2.1 MR signal of a cylindrical volume containing a coaxial object

As we have previously described the theoretical concept of this signal calculation in [8], here we only summarize the concept and needed equations. We begin with the phase value of the complex MR signal inside an infinitely long cylinder (or a finite cylinder with a ratio of the height to the diameter being at least 5 to 1 [45]) from a gradient echo sequence [12]

$$\phi_{in} = -\gamma \frac{\Delta\chi}{6}(3\cos^2\theta - 1)B_0 T_E \equiv \frac{g}{3}(1 - 3\cos^2\theta) \tag{4.1}$$

where γ is the proton gyromagnetic ratio $(2\pi \cdot 42.58)$ MHz/T, $\Delta\chi$ is the susceptibility difference between the regions inside and outside the object, θ is the angle between the main field direction and the axis of the cylinder (see Fig. 4.1(a)), B_0 is the main magnetic field, T_E is the echo time, and $g \equiv 0.5\gamma B_0 \Delta\chi T_E$. The orientation θ can be estimated manually from a 3D data set based on the coordinates of the two end points of a cylindrical object. The word susceptibility hereafter refers to $\Delta\chi$, unless it is otherwise explained. We have adopted the SI units throughout the paper. The phase outside the cylindrical object is

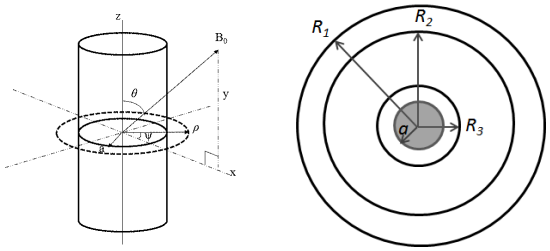

(a) (b)

Figure 4.1: (a) A cylinder has an orientation θ relative to the main field. (b) A schematic drawing shows the cross section of a cylindrical object with radius a, enclosed by three coaxial pseudo cylinders (or circles) whose radii are R_1, R_2, and R_3. The MR signal within each pseudo cylinder (or circle) is S_1, S_2, and S_3, respectively.

given by

$$\phi_{out} = -\gamma \Delta B T_E = -\gamma \frac{\Delta\chi}{2} \frac{a^2}{\rho^2} B_0 T_E \cos 2\psi \sin^2\theta \tag{4.2}$$

where ρ is the perpendicular distance measured from the axis of the cylinder, and ψ is the polar angle associated with ρ. A drawing depicting a cylindrical object and those angles is displayed in Fig. 4.1(a).

Through choosing a coaxial pseudo-cylinder of radius R, which is around the cylindrical object of interest with a radius of a (such that $R > a$ shown in Fig. 4.1(b)), the overall gradient echo signal within R from a slice perpendicular to the axis of the cylinder is given by

$$\begin{aligned} S &= \ell\rho_0 \int_a^R d\rho\, \rho \int_0^{2\pi} d\psi\, e^{i\phi_{out}} + \pi\ell a^2 \rho_{0,c} e^{i\,\phi_{in}} && (4.3) \\ &= \pi\ell\rho_0 \wp \int_{\wp/R^2}^{g'} \frac{dx}{x^2} J_0(x) + \pi\ell a^2 \rho_{0,c} e^{i\,\phi_{in}} && (4.4) \end{aligned}$$

where ℓ is the slice thickness of the image or can be an arbitrary length of the cylindrical

object, ρ_0 is the effective spin density outside the object, $\rho_{0,c}$ is the effective spin density inside the cylindrical object, $\wp$ is the effective magnetic moment defined by $\wp \equiv ga^2 \cdot \sin^2\theta \equiv g'a^2$, g' is the maximal (or minimal) phase value at the surface of the object (see Eq.(4.2)) and is defined by $g' \equiv g \cdot \sin^2\theta$, and J_0 is the zeroth order Bessel function. The word "effective" is dropped from this point on. Both $\rho_{0,c}$ and ρ_0 are treated as unknown constants in Eq.(4.4) and they depend on imaging parameters, actual spin densities, and relaxation times T_1 and T_2.

4.2.2 Susceptibility quantification of a cylindrical object with MR signal

Equation(4.4) contains four independent unknowns: the magnetic moment, susceptibility, and two spin densities (i.e., ρ_0 and $\rho_{0,c}$). We first choose one circle to determine the center of the object. The center of the object as shown in Fig. 4.1(b) can be identified by minimizing the real part of the overall signal from a circle enclosing the cross section of the object (see section 3.1 of [8]). As the signals are added within the circle, this procedure of finding the center of the object is minimally affected by the partial volume effect or any subpixel shift of the center. After identifying the center of the object, we choose three concentric circles to quantify the magnetic moment $\wp$. Figure 4.1(b) shows the schematic drawing of the three radii (R_1, R_2, R_3) for the magnetic moment quantification. The optimal choices of those radii have been described in [8]. Briefly, from Eq.(4.4), we can derive

$$Re(S_1 - S_2)\int_{\wp/R_3^2}^{\wp/R_2^2} \frac{dx}{x^2} J_0(x) = Re(S_2 - S_3)\int_{\wp/R_1^2}^{\wp/R_2^2} \frac{dx}{x^2} J_0(x) \tag{4.5}$$

where S_1, S_2, and S_3 are calculated from complex sums of the signals (from images) enclosed by R_1, R_2, and R_3, respectively, and $R_1 > R_2 > R_3$. In addition, $Re(S)$ is the

real part of the complex signal S. Note that $\wp$ is the only unknown in Eq.(4.5) to be solved. On the other hand, both $\pm\wp$ satisfy Eq.(4.5). In order to improve the accuracy of our measurements of those complex sums, each image pixel is further divided into 100 subpixels, as explained in [7].

After finding $\wp$, we can solve the spin density outside the object (ρ_0) from two concentric circles in the following equation, derived from Eq.(4.4).

$$Re(S_1 - S_2) = \pi\ell\rho_0\wp \int_{\wp/R_1^2}^{\wp/R_2^2} \frac{dx}{x^2} J_0(x) \tag{4.6}$$

Here we choose the annular region between R_1 and R_2, as this region contains more pixels than those between R_2 and R_3.

We can now proceed to solve $\Delta\chi$. By eliminating $\pi\ell a^2\rho_{0,c}$ in Eq.(4.4), the complex signal S can be rewritten into one equation, in which susceptibility $\Delta\chi$ is the only unknown.

$$\begin{aligned} Re(S)\sin\phi_{in} &= Im(S)\,\cos\phi_{in} + \pi\ell\rho_0\wp\,\sin\phi_{in} \int_{\wp/R^2}^{g'} dx J_0(x)/x^2 \\ &= Im(S)\,\cos\phi_{in} + \pi\ell\rho_0|\wp|\,\sin\phi_{in} \int_{|\wp|/R^2}^{|g'|} dx J_0(x)/x^2 \end{aligned} \tag{4.7}$$

where $Im(S)$ is the imaginary part of the complex signal S. After the susceptibility is solved from the Van Wijngaarden-Dekker-Brent method [19], the radius a of the object can be calculated from $\sqrt{\wp/g'}$. For our quantifications, we choose $R = R_3$, which is the innermost radius shown in Fig. 4.1(b), and its corresponding $S = S_3$ for Eq.(4.7). The sign of the susceptibility solved from Eq.(4.7) will indicate whether the object is paramagnetic or diamagnetic relative to its surrounding environment, if the counterclockwise definition

of the spin rotation [27] is used as in Eq.(4.1) and Eq.(4.2). If a vendor uses the clockwise definition, then the susceptibility solved from Eq.(4.7) should be multiplied by a minus sign. Afterward, Eq.(4.4) will allow us to solve $\rho_{0,c}$. It is important to note that due to the nonlinear nature of Eq.(4.7), multiple solutions of the susceptibility may exist. This will depend on the value of g' and this is further discussed in detail in section 4.4.2 and Appendix H.

4.2.3 A cylindrical object parallel to the main field

To be more general, the descriptions in this subsection include orientations of objects close to 0°. These situations have little phase distributions outside those objects and the above approach becomes unpractical, due to very small or nulled $\wp$. In addition, phase inside a small object may be aliased and also affected by the Gibbs ringing. Thus, we utilize the complex signals at two different echo times to solve for $\Delta\chi$. We then solve for radius a. The details are described below. First, we quantify spin density outside the cylinder of interest with two concentric circles at each echo time. When θ is close to 0°, we can assume that $|g'|$ is less than 1 with some choices of T_E. In the condition of $|g'| < 1$, $J_0(x)$ can be well approximated by $1 - x^2/4$ and Eq.(4.7) can be rewritten as

$$Re(S_n)\sin\phi_{in,n} = Im(S_n)\cos\phi_{in,n} + \pi\ell\rho_{0,n}\sin\phi_{in,n}(R^2 + \frac{g_n'^2 a^4}{4R^2} - a^2 - \frac{g_n'^2 a^2}{4}) \qquad (4.8)$$

where the subscript n is referred to each variable obtained at the n^{th} echo time T_{E_n}, as those variables depend on the echo time. At each echo time, if we choose two different

radii, $R_a > a$ and $R_b > a$, then we can derive

$$Re(S_{n,a}) - Re(S_{n,b}) = \pi \ell \rho_{0,n}(R_a^2 - R_b^2)(1 - \frac{g_n'^2 a^4}{4R_a^2 R_b^2}) \tag{4.9}$$

As $|\wp_n|/R^2 = |g_n'|a^2/R^2$ and is the maximal phase at radius R, with the presumptive $|g_n'| < 1$, it will be easy enough to choose slightly large R_a and R_b such that both $|g_n'|a^2/R_a^2$ and $|g_n'|a^2/R_b^2$ are less than 0.5. This will lead to $(g_n'^2 a^4)/(4R_a^2 R_b^2) < 1/16$, which can be neglected from Eq.(4.9). As a result, each $\rho_{0,n}$ can be estimated from Eq.(4.9).

Furthermore, if we choose the same R on images at two different echo times T_{E_1} and T_{E_2}, then Eq.(4.8) can be rewritten as

$$Re(S_1)\sin\phi_{in,1} = Im(S_1)\cos\phi_{in,1} + \pi\ell\rho_{0,1}\sin\phi_{in,1}(R^2 + \frac{g_1'^2 a^4}{4R^2} - a^2 - \frac{g_1'^2 a^2}{4}) \tag{4.10}$$

$$Re(S_2)\sin\phi_{in,2} = Im(S_2)\cos\phi_{in,2} + \pi\ell\rho_{0,2}\sin\phi_{in,2}(R^2 + \frac{g_2'^2 a^4}{4R^2} - a^2 - \frac{g_2'^2 a^2}{4}) \tag{4.11}$$

By multiplying Eq.(4.10) by $\rho_{0,2}\sin\phi_{in,2}$ and multiplying Eq.(4.11) by $\rho_{0,1}\sin\phi_{in,1}$, we obtain

$$\begin{aligned}
&(\rho_{0,2}Re(S_1) - \rho_{0,1}Re(S_2))\sin(\phi_{in,1})\sin(\phi_{in,2}) = \\
&\quad \pi\ell\rho_{0,1}\rho_{0,2}\sin(\phi_{in,1})\sin(\phi_{in,2})\frac{a^2}{4}(1 - \frac{a^2}{R^2})(g_2'^2 - g_1'^2) \\
&\quad +\rho_{0,2}Im(S_1)\sin(\phi_{in,2})\cos(\phi_{in,1}) - \rho_{0,1}Im(S_2)\sin(\phi_{in,1})\cos(\phi_{in,2})
\end{aligned} \tag{4.12}$$

Eq.(4.12) now contains only two unknowns: the radius of the object a and the magnetic susceptibility $\Delta\chi$. When the orientation is close to 0°, we may neglect the g'^2 term in Eq.(4.12) and $\Delta\chi$ becomes the only unknown in the equation. As $\phi_{in}(T_{E_n}) \simeq -2g_n/3$,

Eq.(4.12) becomes

$$\begin{aligned}
&\left[\rho_{0,2} Im(S_{T_{E_1}}) + \rho_{0,1} Im(S_{T_{E_2}})\right] \sin\left(\frac{2(g_1 - g_2)}{3}\right) \\
&- \left[\rho_{0,2} Im(S_{T_{E_1}}) - \rho_{0,1} Im(S_{T_{E_2}})\right] \sin\left(\frac{2(g_1 + g_2)}{3}\right) = \\
&\left[\rho_{0,2} Re(S_{T_{E_1}}) - \rho_{0,1} Re(S_{T_{E_2}})\right] \left[\cos\left(\frac{2(g_1 - g_2)}{3}\right) - \cos\left(\frac{2(g_1 + g_2)}{3}\right)\right] \qquad (4.13)
\end{aligned}$$

After solving $\Delta\chi$, the cross-sectional area of the object, πa^2, can be solved from Eq.(4.8) and $\rho_{0,c}$ can be uniquely solved from the imaginary part $Im(S) = \pi \ell a^2 \rho_{0,c} \sin\phi_{in}$ of the object signal.

The nature of trigonometric functions may lead to multiple solutions of $\Delta\chi$. However, those solutions should be validated by checking whether they satisfy both Eq.(4.10) and Eq.(4.11). In addition, as almost all biological tissues have $|\Delta\chi| \leq 2$ ppm [46], for $B_0 \leq 3$ T and $T_E \leq 11.7$ ms, these values lead to $|\phi_{in}| \leq 2\pi$. If $|g'|$ is small but not zero, then based on discussions in H.2 and knowledge of the signs of $Im(S)$ from summation and ϕ_{in} from a direct measurement of phase images, the possible number of solutions of susceptibility for a biological tissue with the stated MR parameters is no more than two. If $g' = 0$, we can either estimate the radius a of the object or neglect it in Eq.(4.8), and then follow a similar approach described in H.1 to solve the susceptibility. In this scenario, the solved ϕ_{in} is unique between 0 and 2π. If two or more solutions simultaneously satisfy Eq.(4.10) and Eq.(4.11), then more echo times can be used to determine the actual solution of $\Delta\chi$. More details are discussed in section 4.4.2.

4.2.4 The magic angle orientation

When the orientation of a cylindrical object is close to the magic angle, phase inside the object is zero, and the second term (the complex term) in Eq.(4.4) becomes a real number. In this orientation, the single echo approach is not applicable, as the signal inside the object does not produce an imaginary part. As a result, the uncertainty of the susceptibility based on Eq.(L.1) becomes infinite. If we consider a double echo approach, with a short separation between two echoes such that $\rho_{0,c}$ does not vary too much between the two echo times, the signal difference between two echo times is roughly

$$S_{T_{E_1}} - S_{T_{E_2}} \approx \pi \ell \rho_{0,1} \wp_1 \int_{\wp_1/R^2}^{g_1'} dx\, J_0(x)/x^2 - \pi \ell \rho_{0,2} \wp_2 \int_{\wp_2/R^2}^{g_2'} dx\, J_0(x)/x^2 \tag{4.14}$$

where the subscripts 1 and 2 refer to the variables at the two echo times. As the magnetic moment and spin density outside the cylinder at two different echo times can be solved [8], Eq.(4.14) is again left with only one unknown, $\Delta\chi$, to be solved.

In order to evaluate the feasibility of this approach, we have simulated images with a cylindrical object at the magic angle orientation and with imaging parameters given in section 4.2.6.

4.2.5 Calculating uncertainties of susceptibility and other unknowns

The two major independent errors leading to uncertainties in susceptibility and other measures available in this work are from the thermal (white) noise due to the presence of the object and the systematic noise due to discrete pixels, partial volume, and Gibbs ringing in images. We can derive the uncertainty of $\Delta\chi$ based on Eq.(4.7) for most orien-

tations or Eq.(4.12) for the parallel orientation, through the error propagation method [18]. Similarly, the uncertainties of object size and spin densities can be derived. These results are given in Appendices F and G. All noise estimates in Appendices F and G, including the orientation measurements, are uncorrelated. The minimization of uncertainties may also reveal the optimal imaging parameters or radius selection.

The thermal noise within an area A_R can be approximated by $\sigma\ell\sqrt{\Delta x\Delta y A_R}$, where σ is the standard deviation of the thermal noise in the images and Δx and Δy are the in-plane resolutions [7]. The error due to the systematic noise can be calculated if the center of the cylindrical object, the radius of the object, and the susceptibility difference are all known. Simulations and results of the systematic error have been discussed in [7, 8].

4.2.6 Simulations

In our simulations, we assumed a $\Delta\chi$ of 0.5 ppm and a main field of 3 T. We simulated each cylindrical object and its induced magnetic field on a 4096×4096 matrix and converted the matrix to 256×256. We added the white noise to the 256×256 matrix. The detailed procedures were described in [7, 8]. We performed most of our simulations and susceptibility quantifications on a Pentium 4 personal computer. The radius of each cylindrical object on the 256×256 matrix was targeted to be one pixel. We simulated objects at five orientations $\theta = 90°$, $70°$, $57°$ (magic angle), $40°$, and $0°$, and at three echo times $T_E = 11$, 17, and 20 ms. An effective spin density of 20 arbitrary units at $T_E = 0$ with a transverse relaxation rate, $R_2 = 10\,s^{-1}$, was used for the signal inside the cylinder but 10 for the outside. The standard deviation of the thermal noise (σ) was set to be one arbitrary unit such that the signal-to-noise ratio (SNR) outside the cylinder was 10:1. The complex signal from the innermost circle (see Fig. 4.1(b)) was utilized for the susceptibility

quantification.

Liu et al. [47] and Liu et al. [24] suggested that more precise susceptibility values may be calculated from magnetic moments estimated from QSM. Thus, as a comparison between our method and QSM, we applied two QSM methods, susceptibility weighted imaging and mapping (SWIM) [35] and morphology enabled dipole inversion (MEDI) [41], to the same simulated images with the object at an orientation of 90°. For SWIM and MEDI, we duplicated each image 63 times in order to generate a 3D dataset for susceptibility quantification. We downloaded MEDI from http://weill.cornell.edu/mri/pages/qsm.html and tested it with the susceptibility quantification of an infinitely long cylinder with a radius of 16 pixels. The quantified susceptibility value perfectly matched with the input susceptibility value in this particular simulation.

4.2.7 Phantom studies

We prepared a gelatin solution with 60 g of gelatin powder in 1200 ml distilled water. We poured 800 ml of the gelatin solution into a rectangular plastic container, which has a length of 15.0 cm, width of 10.0 cm, and height of 14.0 cm. This was the body of our gel phantom. We prepared a gadolinium solution by adding 1.3 ml of the original Gd-DTPA (Gadolinium-diethylenetriaminepentaceate) MRI contrast agent (which has a concentration of 0.5 M) into the remaining 400 ml of the gelatin solution. The total volume of the gadolinium solution became 401.3 ml. We filled a 10.5 cm long empty straw with the gadolinium solution. We sealed both ends of the straw after it was filled. We immersed the filled straw completely into the middle of the gel phantom. A plastic stand holding up the straw was at the straw's bottom. The molar susceptibility of Gd-DTPA $\chi_{M,Gd-DTPA}$ is $4\pi \times (0.027 \pm 0.001)$ ppm/mM [13]. With water susceptibility roughly -9.05 ppm, the ab-

solute volume susceptibility of the gadolinium solution was about -8.47 ± 0.05 ppm. The susceptibility of interest, $\Delta\chi$, was therefore 0.58 ± 0.05 ppm. The diameter of the straw was 4.92 ± 0.02 mm, measured by a Vernier caliber, and it led to a cross-sectional area of 19.0 ± 0.2 mm^2.

We imaged the phantom with a conventional single-echo 3D spoiled gradient echo (SPGR) sequence, in a 3 T clinical GE Discovery MR750 machine. We used a quadrature head coil for all phantom studies. The imaging parameters were: $T_E = 11$ ms, 17 ms, and 20 ms, $T_R = 30$ ms, flip angle = 20°, read bandwidth = 244.14 Hz/pixel, resolution = 1 mm $\times$ 1 mm $\times$ 1 mm, and fields of view = 256 mm $\times$ 256 mm $\times$ 28 mm. We manually changed the echo time three times and acquired images from three echoes. The acquisition time for each echo was about 4 minutes. We rotated the entire phantom including the straw and scanned the phantom in four different orientations relative to the main field. We aligned images such that they were roughly perpendicular to the straw. As a result, the normal vector of the imaging plane with respect to the main field and the unit vector of the straw relative to the normal vector of the images were used to further determine the actual orientations of the straw with respect to the main field more accurately. The information of unit vectors was listed at tag numbers (0020, 0032) and (0020, 0037) in the DICOM header [48]. The actual orientations of the straw were determined to be roughly 90°, 75.5°, 28.2°, and 0°. We analyzed two different slices from each orientation and each echo time, in order to check the consistency in our phantom studies.

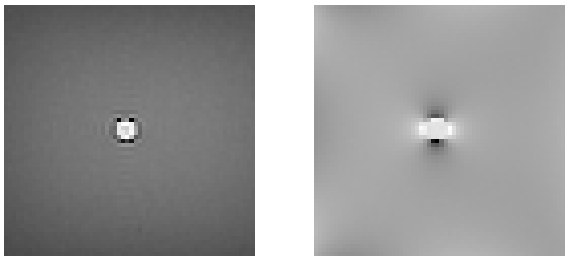

(a) (b)

Figure 4.2: (a) The magnitude and (b) its associated filtered phase image at echo time 20 ms were acquired from a 3 T machine. The straw filled with a Gd-DPTA solution has a diameter of 4.92 ± 0.02 mm. The straw was immersed in the gel phantom and was perpendicular to the main field.

Steps to obtain susceptibility values

With the actual orientation of each straw measured from the procedures described above, the steps to obtain quantified susceptibility $\Delta\chi$ were as follows:

1. We collected and reconstructed the k-space data.

2. We manually unwrap the background phase in each phase image at each echo time by adding proper multiples of 2π in each aliased phase region.

3. We removed the background phase around each straw in each image from the following procedures. We first selected a region of interest (ROI) with a matrix size of 62×62 pixels centered around the straw of interest. We excluded pixels within a radius between 8 and 10 pixels around the straw, depending on the extent of the dipolar phase pattern. We then fit a second order polynomial in 2D to the phase values of those remaining pixels in the ROI. The fitted polynomial from each image of interest represented the background phase, which was subtracted from the unwrapped phase image. A cleaned phase image was then obtained. On each

cleaned phase image, the mean phase value from pixels inside the ROI but outside the dipolar phase pattern of the straw was close to zero. An example of the magnitude and cleaned phase image of the Gd-DPTA doped straw is shown in Fig. 4.2(a) and Fig. 4.2(b).

4. After these procedures, we identified the center of the object (i.e., straw) with the searching algorithm described in [8].

5. With the known center of the object, we solved the magnetic moment of the object with Eq.(4.5) and the spin density surrounding the object with Eq.(4.6).

6. With the known orientation of the object, we solved the susceptibility of the object at each echo time with Eq.(4.7), for all orientations except for the parallel cases. For the parallel orientation, we solved the susceptibility of the object with Eq.(4.12) using two echo times.

To study the effect due to different straw sizes, we reduced the image resolutions of cleaned images and then applied our method for susceptibility quantifications. For each image of interest with the original size of 256×256, we Fourier transformed the magnitude and cleaned phase images to k-space. Then we selected the central 128×128 or 100×100 points out of the 256×256 complex matrix in k-space. We inverse Fourier transformed those smaller matrices back to the image domain and obtained images with lower resolutions. As a result, the theoretical diameters of the straw became 2.46 ± 0.02 mm and 1.92 ± 0.02 mm, respectively. By doing this, we could evaluate our method in a consistent way without introducing additional experimental errors (e.g., effects due to the wall of a small straw).

We also applied SWIM and MEDI on the same cleaned phase images of matrix size 256×256 and 128×128 (but duplicated each image 63 times to generate a 3D dataset) at the 90° orientation. After obtaining the susceptibility maps from SWIM and MEDI, we calculated the mean and standard deviation of the susceptibility from four pixels completely inside the straw and from the central image of each 3D set. In addition, we also measured the background susceptibility values surrounding the straw. The susceptibility values quantified from SWIM and MEDI are shown in Table 4.2.

4.2.8 Pilot in-vivo study

A set of 3D gradient echo images of a female volunteer acquired from a 4 T Bruker/Siemens machine was available to us. The imaging parameters of the gradient echo sequence were $T_E = 19.2$ ms, $T_R = 26$ ms, flip angle = $11°$, read bandwidth = 120 Hz/pixel, resolution = 0.5 mm $\times$ 0.5 mm $\times$ 0.51 mm, and field of view = 256 mm $\times$ 176 mm $\times$ 45 mm. We analyzed a vein on the transverse plane, as shown in Fig. 4.3a and 4.3b. The coronal and sagittal view of this vein is shown in Fig. 4.4. Fig. 4.4c shows a reasonable dipolar pattern of the vein in the phase image and no other objects around this vessel. We quantified the susceptibility with the same steps described in the previous subsection, except that we removed the background phase with a 16×16 high pass filter. In addition to our method, we also applied SWIM to this $in\text{-}vivo$ dataset and compared the susceptibility values between the two methods.

4.3 Results

We summarize below the quantified susceptibility values, cross-sectional areas (A_0), and spin densities from simulations and phantom studies for different orientations and echo times. In order to calculate the uncertainty of each measurement, we first need to

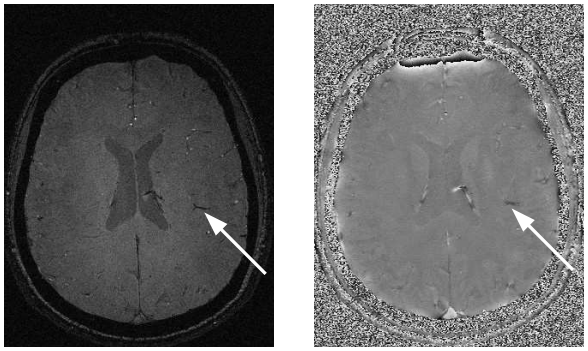

(a) (b)

Figure 4.3: (a) Magnitude and (b) its associated phase image of a volunteer acquired from a 3D gradient echo image at $T_E = 19.2\,\text{ms}$ of $4\,\text{T}$. The vein whose susceptibility is analyzed in this work is indicated by arrows.

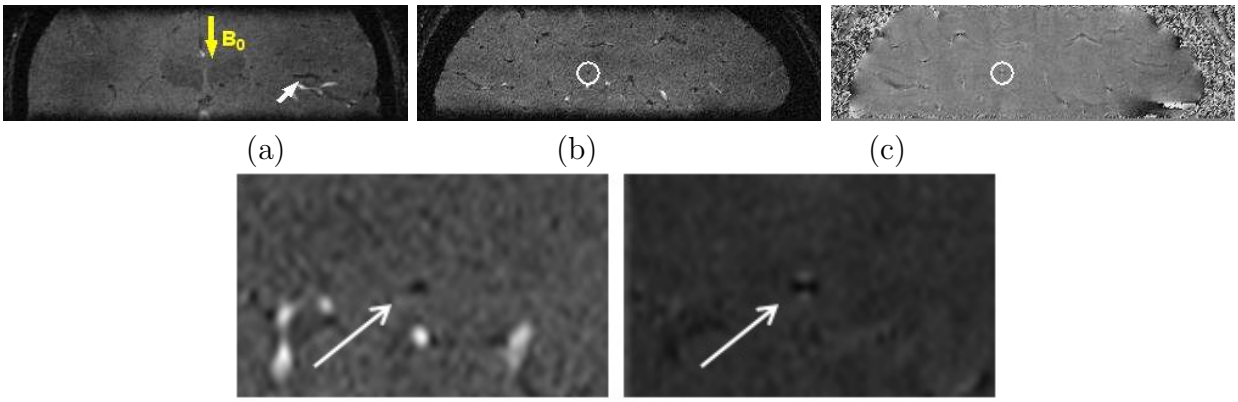

(a) (b) (c)

(d) (e)

Figure 4.4: (a) Coronal view of the same vein (indicated by a white arrow) as shown in Fig. 4.3. The direction of the main field is shown by the yellow arrow. The orientation of this vein is 80° relative to the main field. The same vein (inside circles) is also displayed in the (b) sagittal magnitude and (c) its associated phase image. (d) The enlarged magnitude image of (b). (e) The enlarged phase image of (c).

estimate the uncertainties of the orientation and magnetic moment. The former is roughly one degree in all of our phantom studies while the latter is given in a formula shown in [8].

4.3.1 Arbitrary orientations except for the parallel orientation: simulations and phantom studies

Simulated images at 90°**,** 70°**, and** 40°

As shown in Table 4.1, most measurements of the susceptibility from our approach are close to the original input $\Delta\chi$ of 0.5 ppm. The differences between all quantified

susceptibilities and the actual value are no more than 16%. On the other hand, the estimated uncertainties are sometimes larger due to smaller orientations and shorter echo times. The actual cross-sectional area of each simulated cylinder is 3.14 pixel^2 and the actual spin densities are 17.9, 16.9, and 16.4 at $T_E = 11$, 17, and 20 ms, respectively. The cross-sectional areas and spin densities solved from our approach agree with these true values to within 30%. Again, the estimated uncertainties can be even larger due to uncertainties propagated from susceptibility quantifications. Due to the combination of Gibbs ringing and finite sampling effects, the spin density values inside the objects have been systematically underestimated, as shown in Table 4.1. On the other hand, the spin densities outside the objects have been systematically overestimated.

Table 4.1: Quantified results from simulated images at three different echo times and three orientations. The actual values are: $\Delta\chi = 0.5$ ppm, $A_0 = 3.14$ pixel^2, $\rho_0 = 10$, and $\rho_{0,c}$ at different echo times are given in the text. The first column lists the orientation. The second column lists the echo time. The third column lists magnetic moment $\wp$ calculated from the method in [8]. Numbers inside the parentheses are the theoretical $\wp$ values. The fourth column lists $\Delta\chi$ solved from Eq.(4.7). The chosen radius, R_3, for solving $\Delta\chi$, is 1.5 pixel. The fifth column lists the cross-sectional area of the cylinder. The sixth column lists the effective spin density inside the object calculated from the imaginary part of Eq.(4.4). The seventh column lists the effective spin density outside the object calculated from Eq.(4.6)

Angle (degree)	T_E (ms)	$\wp$ (rad·pixel^2)	$\Delta\chi$ ppm	A_0 pixel^2	$\rho_{0,c}$	ρ_0
90	11	2.21±0.49 (2.21)	0.54±0.18	2.90±0.98	20.3±4.3	9.86±0.20
	17	3.42±0.31 (3.41)	0.50±0.06	3.14±0.41	18.4±2.0	9.83±0.20
	20	4.01±0.16 (4.01)	0.49±0.04	3.14±0.35	17.9±1.8	9.84±0.15
70	11	1.95±0.51 (1.95)	0.57±0.28	2.78±1.39	20.9±6.3	9.87±0.20
	17	3.01±0.45 (3.01)	0.52±0.11	3.02±0.63	19.0±3.0	9.84±0.20
	20	3.51±0.28 (3.54)	0.52±0.09	3.02±0.57	18.4±2.6	9.85±0.20
40	11	0.70±1.75 (0.91)	0.52±1.56	2.32±13.9	20.1±124.6	9.77±0.22
	17	1.55±0.67 (1.41)	0.42±0.34	4.08±4.49	13.4±13.4	9.90±0.20
	20	1.82±0.56 (1.66)	0.44±0.25	3.94±3.23	12.9±9.5	9.91±0.20

Applications of SWIM and MEDI to simulated images

The magnetic moments and susceptibility values quantified from SWIM are 3.84 rad·pixel^2 (0.87 ppm), 2.87 rad·pixel^2 (0.42 ppm), and 2.89 rad·pixel^2 (0.36 ppm) at T_E = 11, 17, and 20 ms, respectively. The magnetic moments and susceptibility values quantified from MEDI are 1.68 rad·pixel^2 (0.38 ppm), 4.03 rad·pixel^2 (0.59 ppm), and 5.30 rad·pixel^2 (0.66 ppm) at T_E = 11, 17, and 20 ms, respectively. These results are not self consistent and they are at least 16% deviated away from the actual susceptibility value (0.5 ppm).

Simulated images at 54.7° (magic angle)

The quantified magnetic moments are 1.92 ± 0.35 rad·pixel^2, 2.58 ± 0.23 rad·pixel^2, and 2.98 ± 0.21 rad·pixel^2, at echo times 11, 17, and 20 ms, respectively. The quantified magnetic susceptibility is 0.80 ± 3.20 ppm obtained from $T_E = 11$ ms and 17 ms using Eq.(4.14). Similarly, the susceptibility value is 0.60 ± 0.25 ppm obtained from $T_E = 17$ ms and 20 ms. These results are quite different from the actual susceptibility 0.5 ppm. In addition, uncertainties derived from the error propagation method are fairly large. In general, when no phase value exists inside the object, eliminating the object signal as shown in Eq.(4.14) leads to large uncertainties of quantified susceptibilities. One alternative solution to this problem is to physically rotate the object by a certain angle even as small as 15°, in order to gain some signals of the imaginary part.

Phantom studies at three resolutions (matrix sizes)

Most of the susceptibilities measured from our method agree well within 12% of the theoretical value, 0.58 ± 0.05 ppm, for all orientations, different echo times, and image resolutions. The results are listed in Tables 4.7, 4.8, and 4.9. However, the quantified susceptibility values from the 100×100 matrix at angle 28.2° are not reliable. The measured cross-sectional areas and the theoretical value agree within 16%, except for results from the 28.2° orientation and from lower image resolutions. Some uncertainties are large due to large uncertainties propagated from the magnetic moments.

Applications of SWIM and MEDI to phantom studies

The susceptibility values quantified from SWIM and MEDI for phantom studies are listed in Table 4.2. For SWIM, we have assigned the suggested thresholding parameter 0.1 as well as other thresholding parameters 0.02 and 0.3 [35]. The susceptibility result using the thresholding parameter 0.02 is 0.40 ppm, but the map contains severe streak artifacts surrounding the straw filled with the gadolinium solution. The susceptibility result using the thresholding parameter 0.3 is 0.23 ppm. For the MEDI method, we have assigned regularization parameters, 50, 100, 250, 400, and 1000 into the kernel. The mean quantified susceptibility values from pixels inside the straw with different regularization parameters are identical to those listed in Table 4.2. All quantified susceptibility values from SWIM or MEDI are underestimated by at least 20% for the perpendicular orientation. For this reason, we do not quantify susceptibility values from SWIM or MEDI from any other orientations, as we expect worse results for those situations. These phantom

and simulated results indicate that current SWIM or MEDI may not accurately quantify susceptibility from cylindrical objects with diameters of less than 5 pixels.

Table 4.2: Quantified magnetic susceptibilities of slice 16 at the 90° orientation from Table 4.7 and Table 4.8, using SWIM and MEDI. For comparisons, results from our method are listed again. The theoretical value of $\Delta\chi$ is 0.58 ± 0.05 ppm. The first column lists the orientation. The second column lists the echo time. The third and fourth column show quantified susceptibility values from our approach. The fifth and sixth column show quantified susceptibility values from SWIM [35]. The seventh and eighth column show quantified susceptibility values from MEDI [41]. The regularization parameters used in MEDI were suggested in their MATLAB code. Optimal choices of those regularization parameters are not known yet [49].

		Our approach		SWIM[a]		MEDI[b]	
Angle (degree)	T_E (ms)	256×256 ppm	128×128 ppm	256×256 ppm	128×128 ppm	256×256 ppm	128×128 ppm
90	11	0.57 ± 0.02	0.57 ± 0.05	0.36 ± 0.02	0.31 ± 0.04	0.42 ± 0.01	0.39 ± 0.06
	17	0.55 ± 0.01	0.59 ± 0.04	0.36 ± 0.08	0.27 ± 0.07	0.40 ± 0.11	0.36 ± 0.06
	20	0.55 ± 0.01	0.54 ± 0.03	0.35 ± 0.07	0.30 ± 0.12	0.40 ± 0.09	0.36 ± 0.16

Comments: [a]thresholding parameter = 0.1. [b]regularization parameter = 250.

4.3.2 Parallel orientation: simulations and phantom studies

Results of simulations and phantom studies for the parallel orientation are shown in Tables 4.3, 4.4, 4.5, and 4.6. Each susceptibility was estimated from Eq.(4.13) with complex signals calculated from two echo times. In Table 4.3, a combination of $T_E = 11$ ms and 17 ms and $T_E = 17$ ms and 20 ms were used for susceptibility quantifications. In Table 4.4, a combination of $T_E = 11$ ms and 17 ms and $T_E = 11$ ms and 20 ms were used for susceptibility quantifications. The reasons for choosing these echo time combinations will be discussed in section 4.4.3. The cross-sectional area of the object, the spin density around and outside the object, and the spin density inside the object were obtained at each echo time. All quantified susceptibility values agree well with the theoretical values. The differences between the quantified susceptibilities and the actual value in simulations were less than 2% and the differences between the quantified cross-sectional areas and

the actual value were less than 8%. In phantom studies, the differences between the quantified susceptibilities and the theoretical value were less than 6%. The differences between quantified cross-sectional areas and the actual value were within 16% for most cases. At $T_E = 20\,\text{ms}$, the estimated uncertainties of cross-sectional areas were very large. This will be discussed further in section 4.4.3.

Table 4.3: Quantified results from simulated images using two different echo times when the object is parallel to the main field. The first column lists the echo time. The second column lists $\Delta\chi$ solved from Eq.(4.13). Numbers inside parentheses show the two echo times used for calculating the susceptibility. The theoretical value of $\Delta\chi$ is 0.5 ppm and the theoretical cross-sectional area is $3.14\,\text{pixel}^2$. The chosen radius, R, for solving Eq.(4.13) is 1.5 pixel. The third column lists the cross-sectional area of the cylinder calculated from Eq.(4.8). The fourth column lists the effective spin density inside the object calculated from the imaginary part used in Eq.(4.8). The fifth column lists the quantified effective spin density outside the object.

T_E (ms)	$\Delta\chi$ ppm	A_0 pixel^2	$\rho_{0,c}$	ρ_0
11	0.51±0.03 (11/17)	2.90±0.38	19.0±2.7	9.90±0.20
17		2.90±1.33	18.5±11.8	9.89±0.20
20	0.51±0.06 (20/17)	2.90±3.76	14.4±21.8	9.89±0.20

Table 4.4: Quantified results from phantom images of the original image resolution at two slices using two different echo times when the object is parallel to the main field. The theoretical value of $\Delta\chi$ is $0.58 \pm 0.05\,\text{ppm}$ and the cross-sectional area is $19.0 \pm 0.2\,\text{mm}^2$. The first column lists the echo time. The second and the sixth column list $\Delta\chi$ solved from Eq.(4.13). The chosen radius, R, for solving Eq.(4.13) is 3.0 mm. The superscripts, a and b, refer to the two echo times used for quantifying susceptibility values. The third and seventh column list the cross-sectional area of the cylinder calculated from Eq.(4.8). The fourth and eighth column list the effective spin density inside the object calculated from the imaginary part used in Eq.(4.8). The fifth and ninth column list the effective spin density outside the object.

	Slice number 12				Slice number 16			
T_E (ms)	$\Delta\chi$ ppm	A_0 mm^2	$\rho_{0,c}$	ρ_0	$\Delta\chi$ ppm	A_0 mm^2	$\rho_{0,c}$	ρ_0
11		21.7±0.4	2424±97	1355±14		21.6±0.4	2388±96	1338±13
17	0.56±0.01^a	21.4±3.2	2332±560	1350±14	0.56±0.01^a	22.1±3.3	2180±506	1329±13
20	0.56±0.01^b	18.6±3.5	2808±842	1341±13	0.56±0.01^b	22.4±4.3	2029±609	1320±13

Comments: $^a T_E = 11\,\text{ms}$ and 17 ms. $^b T_E = 11\,\text{ms}$ and 20 ms .

Table 4.5: Quantified results from phantom images of the 128×128 matrix size reduced from slices shown in Table 4.4. The meaning of each column has been explained in Table 4.4. The chosen radius, R, for solving Eq.(4.13) is 2.0 mm in these cases. The theoretical cross-sectional area is $4.75 \pm 0.05\,\mathrm{mm}^2$.

	Slice number 12				Slice number 16			
T_E (ms)	$\Delta\chi$ ppm	A_0 mm^2	$\rho_{0,c}$	ρ_0	$\Delta\chi$ ppm	A_0 mm^2	$\rho_{0,c}$	ρ_0
11		4.55±0.32	10444±835	5095±51		4.52±0.32	10370±830	5000±50
17	0.55±0.02[a]	4.83±1.30	8729±2008	4764±48	0.55±0.01	4.68±1.26	8749±2012	4619±46
20	0.56±0.01[b]	3.53±1.73	12936±4916	4664±47	0.56±0.01	3.53±1.73	12240±4651	4517±45

Comments: [a] $T_E = 11$ ms and 17 ms. [b] $T_E = 11$ ms and 20 ms.

Table 4.6: Quantified results from phantom images of the 100×100 matrix size reduced from slices shown in Table 4.4. The meaning of each column has been explained in Table 4.4. The chosen radius, R, for solving Eq.(4.13) is 1.5 mm in these cases. The theoretical cross-sectional area is $2.90 \pm 0.03\,\mathrm{mm}^2$.

	Slice number 12				Slice number 16			
T_E (ms)	$\Delta\chi$ ppm	A_0 mm^2	$\rho_{0,c}$	ρ_0	$\Delta\chi$ ppm	A_0 mm^2	$\rho_{0,c}$	ρ_0
11		2.96±0.33	16241±1949	8971±88		3.02±0.33	15674±1881	8776±88
17	0.56±0.03[a]	2.96±1.80	15433±5093	8695±87	0.56±0.03	2.96±1.80	14933±4928	8529±85
20	0.56±0.01[b]	2.60±1.80	18198±8917	8631±86	0.56±0.01	2.84±1.96	15478±7584	8475±85

Comments: [a] $T_E = 11$ ms and 17 ms. [b] $T_E = 11$ ms and 20 ms.

4.3.3 **Pilot** *in-vivo study*

By using our method, the measured magnetic moment of the vein in Fig. 4.4 is 2.13 rad·pixel^2, its susceptibility value is 0.43 ppm, and its cross-sectional area is 1.58 pixel^2. This susceptibility value agrees with the expected susceptibility 0.40 ppm, if we assume an oxygenation level of 70%, a Hematocrit of 0.4, and a susceptibility difference between the fully deoxygenated blood and fully oxygenated blood of 3.39 ppm [50]. As the signal inside the measured vein is about 130 units and the noise of images is about 27 units, the SNR of this vein is around 5 to 1. The SNR of the tissue outside the vein is about 8 to 1. On the other hand, the mean susceptibility value of this vein quantified from SWIM is 0.24 ppm. This pilot study demonstrates that our method will be feasible to clinical studies in the future.

4.4 Discussion

The magnetic moment, the signal of the object itself, and the orientation of the object are the three major factors affecting the quantification of susceptibility in our method. Understanding their uncertainties and roles in the equations sheds some light on how one might improve the accuracy and precision of susceptibility quantifications.

4.4.1 Major factors affecting uncertainty for susceptibility quantification

Uncertainties of the measurements

The uncertainties of susceptibility and other variables are derived from the error propagation method (see section 4.2.5). In order to reduce the uncertainty of a quantified susceptibility, the B^2 and C^2 term in Eq.(L.1) indicate that the radius of R_3 should not be chosen too large. This is to ensure that $Im(S_3)$ is above the noise level. On the other hand, R_3 cannot be too small either, as Gibbs ringing or partial volume can affect each measurement. We suggest R_3 to be at least 0.5 pixel away from the surface of the object but as small as possible. In addition, when $|g'|$ is larger than 3 radians and R_1 and R_2 are optimally chosen, it seems that B^2 and C^2 are the dominant terms in the numerator of Eq.(L.1).

If the susceptibility of an object is roughly known and the focus is to reduce the uncertainty of the measurement, as $\sin\phi_{in}$ appears in both denominator and numerator of Eq.(L.1), it may be helpful to increase the echo time such that $|\sin\phi_{in}|$ becomes unity. If this is not feasible, then one can try to increase the echo time such that $|g'|$ will be between 2.4 and 5.5, with $|g'| \approx 3.5$ being the optimal choice. This is because in this case, $J_0(g')$ becomes negative in the denominator of Eq.(L.1) and thus the uncertainty of

susceptibility is reduced.

Signal inside the cylinder of interest

Eq.(L.1) indicates that increasing SNR inside the cylindrical object ($\mathrm{SNR}_{0,c} \equiv \rho_{0,c}/\sigma$) can reduce the uncertainty of quantified susceptibility. For a sufficiently long cylinder, SNR can be increased by using a thicker slice for example. Increasing the number of acquisitions is also an option, but at the expense of imaging time. In addition, a contrast agent may be used to increase the SNR of the object (e.g., vein). However, the use of contrast agent will mainly help to quantify the object radius more accurately but not to quantify the susceptibility of the object. Nonetheless, a pre- and post-contrast $in\ vivo$ protocol may first allow the determination of the size of a vein from post-contrast images and then calculate only the susceptibility of venous blood based on the magnetic moment measured from pre-contrast images. This assumes that the size of the vein does not change before and after the injection of the contrast agent.

Orientation dependence

When the orientation of a cylindrical object deviates from $90°$, but other factors remain the same, the magnetic moment quantified from the object becomes smaller than that at $90°$ (see section 4.2.1). As a result, the uncertainty of the magnetic moment increases and so does that of the susceptibility. Eq.(L.1) reflects on the above statement. In order to reduce the uncertainty, one possibility is to increase the echo time and therefore the magnetic moment will become larger. When the orientation of the object is close to $0°$, the uncertainty of the estimated susceptibility can be very large (see Eq.(K.2)). This is why for

the parallel orientation, a two-echo approach will be better. Eq.(L.1) also indicates that the uncertainty of susceptibility approaches infinity when the orientation is close to the magic angle. For all quantified susceptibility values, each complex signal from the innermost radius, R_3, is used in Eq.(4.7). As a result, the variables, $\delta Re(S_3)$, $\delta Im(S_3)$, and $\delta(S_i - S_j)$ for any i and j, are uncorrelated. The uncertainty of the susceptibility, Eq.(L.1), is derived based on this condition. For any choice of a radius larger than R_3 used in Eq.(4.7), some variables will become correlated and uncertainty formulas need to be rederived.

For the uncertainty of orientation, $\delta\theta$, low resolution images lead to a larger uncertainty than that quantified from high resolution images. For example, when we convert our phantom images to 4 mm isotropic resolution, on which our straw occupies only a few pixels, the error of the orientation can be up to $\pm 15^\circ$.

Techniques for background field removal

For phantom images, we have tried the high pass filter, quadratic fitting, and sophisticated harmonic artifact reduction for phase data (SHARP) [28] for removing background fields. The quadratic fitting technique is more reliable than the other two techniques when it is applied to our phantom images. High pass filter can remove the background field cleanly at the 90° and 75.5° cases, but not completely remove the background fields at the 28.2° orientation because of the geometry of the phantom container. SHARP, with a kernel size of 6, also shows a similar problem. In addition, after the application of SHARP, the phase values around the straw in the phantom are higher than expected, and the averaged phase value in the background is about 0.1 rad, larger than the noise level in phase images. Furthermore, when we apply SHARP and then our method, SWIM, and MEDI

to the phantom images with the reduced matrix size of 128×128, the quantified susceptibility values of our gadolinium straw become about 0.70 ppm, 0.48 ppm, and 0.55 ppm, respectively.

For human images, given the problems of SHARP described above and the uneasy application of the quadratic fitting technique, we chose to use the high pass filter for removing the background fields. The background phase around the vein was between 0.01 and 0.03 rad after the high pass filter was applied to the $in\text{-}vivo$ data.

4.4.2 The unique solution from Eq.(4.7)

As Eq.(4.7) is a nonlinear function of the magnetic susceptibility, multiple solutions could exist. The number of possible solutions is discussed in the following two subsections. We overlap the range of g' in this section such that some freedom of choices will be allowed. More detailed mathematical descriptions are given in H.

$|g'| > 1.4$ leads to unique solution in one period

When the upper limit $|g'|$ of the integral in Eq.(4.7) is larger than 1.4, with a lower limit, $|\wp|/R^2 \leq 0.5$, the upper limit $|g'|$ can be replaced by infinity and the difference between the actual integral and the approximation is less than 5%. This condition can be achieved by choosing a sufficiently large R. As a result, ϕ_{in} in Eq.(4.7) can be uniquely determined between $2n\pi$ and $2(n+1)\pi$ with n being an arbitrary integer (see Eq.H.2 in H.1). If we choose $B_0 = 3$ T and $T_E = 20$ ms, the possible solutions of $\Delta\chi$ between each adjacent 2π period will differ by at least 1 ppm. This means that susceptibilities of most biological tissues can be uniquely determined with just one echo time.

$0 < |g'| \leq 2$ leads to multiple solutions

Here we summarize our findings, as the detail descriptions and derivations are given in H.2. When $|g'|$ is in this range, we need to examine the number of roots in Eq.(H.3) and Eq.(H.4). As the signs of $\beta \equiv (1 - 3\cos\theta^2)/3$ and $Im(S)$ are known from measurements, the sign of $\beta Im(S)$ is known even before we solve Eq.(H.3). Based on derivations described in H.2, when the object orientation is larger than 24°, at most two roots can be solved from Eq.(H.3). However, if the orientation is less than 24°, then multiple solutions exist. Thus, in this scenario which includes the parallel orientation, we suggest solving the susceptibility with the two-echo approach.

Unknown materials with large susceptibility

For unknown materials with susceptibility values more than 4 ppm, an echo time shorter than 5 ms at 3 T will be needed in order to uniquely determine the susceptibility. However, this may be difficult to achieve and thus multiple echoes may be needed as described below.

As any solution in the form of $\phi_{in} - 2n\pi$ satisfies Eq.(H.1), the actual solution of Eq.(4.7) may be determined from multiple echo gradient echo images. At least, the number of possible solutions will be reduced. For example, consider that phase $q_1 \equiv \phi_{in,1} - 2n_1\pi$ is solved from echo time $T_{E,1}$ and $q_2 \equiv \phi_{in,2} - 2n_2\pi$ is solved from echo time $T_{E,2}$. As $\phi_{in,1}$ and $\phi_{in,2}$ are proportional to $T_{E,1}$ and $T_{E,2}$, respectively, q_1 and q_2 satisfy the following equation

$$\frac{q_1 T_{E,2} - q_2 T_{E,1}}{\pi} = 2(n_2 T_{E,1} - n_1 T_{E,2}) \tag{4.15}$$

Obviously the left hand side of Eq.(4.15) is normally a real number but the right hand side demands that the equation has to be equal to an even integer, if the two echo times are chosen as integers in units of millisecond or sub-millisecond. This is only possible if Eq.(4.15) is zero. Hence, Eq.(4.15) limits possible values of n_1 and n_2. As the magnetic moment $\wp$ and $Im(S)$ are first measured, the subsequently solved susceptibility values $|\Delta\chi|$ will increase as $|n_i|$ increases. The solved object radius a will decrease but the solved spin density inside the object, $\rho_{0,c}$, will increase. However, since rough values of a and $\rho_{0,c}$ can be estimated from the magnitude image, ranges of n_1 and n_2 are limited and $\Delta\chi$ is likely to be uniquely determined with only two echo times. Choosing prime numbers for $T_{E,1}$ and $T_{E,2}$ in millisecond or sub-millisecond units (such as 5.9 ms or 10.9 ms) or using more echoes can very effectively reduce the possible solutions of $\Delta\chi$. This is the main reason why at least a double echo or a triple echo gradient echo sequence is preferred. However, the presence of thermal noise and systematic error may introduce more pseudo solutions.

4.4.3 Measurements and uncertainties from orientations close to 0°

For objects with orientations close to 0°, we may first estimate the value of a^2 from magnitude images. From Eq.(4.12), we can solve an initial value of $\Delta\chi$. Then the updated radius of the object, a, can be calculated from either Eq.(4.10) or Eq.(4.11). The susceptibility value $\Delta\chi$ can be re-solved again from Eq.(4.12). As an iterative procedure, we can repeat the process to reach convergent solutions for the radius of the object, a, and its magnetic susceptibility, $\Delta\chi$.

The uncertainty of susceptibility given in Eq.(G.2) is affected by the SNR inside the object of interest. When the ratio between $SNR_{0,c,1}$ and $SNR_{0,c,2}$ acquired from two echo

times becomes large, the uncertainty of susceptibility will reduce. Thus, the echo spacing between the two echo times is better to be large. This is how the echo time combinations in the phantom experiments were selected (see comments in Table 4.4). In the simulations, we purposely show that the susceptibility of the object can still be quantified from the echo time combination of 17 ms and 20 ms (see Table 4.3), but with a larger uncertainty. Both phase values inside the object acquired from two echo times should not be concurrently multiples of π for susceptibility quantification, as Eq.(G.2) and Eq.(4.13) indicate infinite uncertainty in this scenario. However, the uncertainty of the susceptibility can still be reasonably small, when only either $\phi_{in,1}$ or $\phi_{in,2}$ is a multiple of π. Nonetheless, in this situation, the uncertainties of quantified cross-sectional area and spin density inside the object from that particular echo time will become very large (e.g., see Eq.(G.5) and results at $T_E = 20$ ms in Tables 4.3, 4.4, 4.5, and 4.6)). This is because when a $\phi_{in,n}$ is close to multiples of π, the imaginary part of the signal is close to zero and it becomes impractical to quantify the cross-sectional area and the spin density inside the object.

4.4.4 The limitations of our method and future work

Although our method is derived from the model of an infinitely long cylinder, such a model is valid when the ratio of the height to the diameter of a finite cylinder is larger than 5 to 1 [45]. In addition, the infinitely long cylinder model is also acceptable when any section of a curved cylinder is less than 30° [51]. Thus, for the susceptibility quantification of venous blood, our method is feasible to most $in\ vivo$ medullary and pial veins, with the acquisitions of isotropic 3D gradient echo data from two echo times. Nonetheless, even with a perfect background phase removal procedure, local background phase due to the presence of other neighboring tissues may exist. A large local background phase

such as 0.8 rad may lead to an incorrect center of the object of interest and an incorrect susceptibility value. Thus, our equations for the $in\ vivo$ applications will require local background field corrections after the removal of the global background phase. We are currently revising the equations and engaging these studies.

In our current procedures, for reliable susceptibility quantifications, we suggest to choose the innermost circle with a radius (R_3) of at least 0.5 pixel from the boundary of the object and the differences between any two of the three radii to be at least 1 pixel. This leads to a total of at least 2.5 pixels away from the boundary of a given object. If two or more cylindrical objects or vessels are close to each other, but have at least 5 pixels between their boundaries, then our method is still applicable to the susceptibility quantification of each object. However the accuracy of quantified susceptibility may be a concern. Our method also cannot accurately quantify the susceptibilities of two long cylinders when their nearest boundaries are within 5 pixels, unless they are parallel to the main field. In addition, section 4.4.1 points out low SNR of an object such as a vein at a long echo time will increase the uncertainty (see Eq.(L.1) and Eq.(4.7)). Thus, the steps of quantifying susceptibility and reducing uncertainty in the low SNR object are more complex. Currently we are investigating this situation. In addition, the uncertainty of quantified susceptibility values at the low orientation is large due to small g'. The two echo approach for the low orientation may reduce the uncertainty. We are also investigating this possibility to reduce the uncertainty of the quantified susceptibility.

4.5 Conclusion

Using a standard gradient echo sequence with one or two echo times, our method can accurately quantify magnetic moment, susceptibility, radius, and spin density ρ_0 and

$\rho_{0,c}$ of a given cylindrical object at most orientations. The accuracy of quantified susceptibility can be improved by the orientation close to 90°, high SNR of the object, or a long echo time within the clinical range. Our approach has overcome two problems in estimating susceptibility: phase aliasing and partial volume effects. We have demonstrated the feasibility of this method through simulations, phantom, and $in\text{-}vivo$ human studies. Our method provides an alternate approach for accurate susceptibility and radius quantifications of narrow cylinders.

Table 4.7: Quantified results from phantom images of the original image resolution at three different echo times and three orientations. Two different slices, 12 and 16, were analyzed. The theoretical value of $\Delta\chi$ is 0.58 ± 0.05 ppm and the actual cross-sectional area is $19.0 \pm 0.2\,\mathrm{mm}^2$. The SNR around and outside the straw for all three echo times is about 30:1. The SNR values inside the straw at three echo times, 11, 17, and 20 ms, are about 48:1, 44:1, and 42:1, respectively. The first column lists the orientation. The second column lists the echo time. The third column shows the theoretical $\wp$. The fourth and ninth column show quantified $\wp$. The fifth and tenth column list $\Delta\chi$ solved from Eq.(4.7). The sixth and eleventh column show the cross-sectional area of the cylinder. The seventh and twelfth column list the effective spin density inside the object calculated from the imaginary part of Eq.(4.4). The eighth and thirteenth column list the effective spin density outside the object calculated from Eq.(4.6)

			Slice number 12					Slice number 16				
Angle (degree)	T_E (ms)	$\wp$ (rad·mm^2)	$\wp$ (rad·mm^2)	$\Delta\chi$ ppm	A_0 mm^2	$\rho_{0,c}/1000$	ρ_0	$\wp$ (rad·mm^2)	$\Delta\chi$ ppm	A_0 mm^2	$\rho_{0,c}/1000$	ρ_0
90	11	15.4	14.1±0.7	0.57±0.02	17.6±0.5	2.85±0.06	1235±12	14.5±0.7	0.57±0.02	18.2±0.5	2.72±0.05	1246±12
	17	23.9	21.9±0.5	0.54±0.01	19.2±0.4	2.49±0.02	1218±12	22.4±0.4	0.55±0.01	19.2±0.2	2.55±0.03	1224±12
	20	28.2	26.3±0.5	0.54±0.01	19.0±0.4	2.37±0.05	1208±12	26.2±0.5	0.55±0.01	18.7±0.4	2.40±0.05	1213±12
75.5	11	14.5	12.9±0.9	0.58±0.04	16.9±0.8	2.83±0.10	1216±12	13.0±0.9	0.60±0.04	16.5±0.8	2.83±0.11	1232±12
	17	22.4	21.3±0.4	0.54±0.03	19.3±0.6	2.49±0.10	1203±12	21.1±0.4	0.56±0.04	18.6±0.6	2.53±0.10	1213±12
	20	26.4	24.6±0.5	0.54±0.03	19.0±0.8	2.38±0.10	1197±12	24.5±0.5	0.56±0.03	18.2±0.7	2.36±0.09	1206±12
28.2	11	3.45	3.64±2.87	0.60±0.27	19.3±38.6	2.63±5.06	1280±13	3.22±3.22	0.65±0.53	15.8±31.5	3.13±7.20	1267±13
	17	5.34	6.25±3.75	0.55±0.13	23.4±21.5	2.16±2.03	1280±13	6.11±3.85	0.57±0.13	22.6±20.3	2.36±2.22	1274±13
	20	6.29	6.65±3.39	0.57±0.10	20.4±18.0	2.32±2.23	1268±13	6.97±3.07	0.56±0.10	21.9±19.3	2.13±2.04	1274±13

Table 4.8: Quantified results from phantom images of reduced 128 × 128 matrix size at three different echo times and three orientations. Two different slices, 12 and 16, were again analyzed. The theoretical value of $\Delta\chi$ is still 0.58 ± 0.05 ppm but the cross-sectional area becomes $4.75 \pm 0.05\,\mathrm{mm}^2$. The SNR around and outside the straw for all three echo times is about 60:1. The SNR values inside the straw at three echo times, 11, 17, and 20 ms, are about 96:1, 88:1, and 84:1, respectively. The meaning of each column has been explained in Table 4.7.

			Slice number 12					Slice number 16				
Angle (degree)	T_E (ms)	$\wp$ (rad·mm^2)	$\wp$ (rad·mm^2)	$\Delta\chi$ ppm	A_0 mm^2	$\rho_{0,c}/1000$	ρ_0	$\wp$ (rad·mm^2)	$\Delta\chi$ ppm	A_0 mm^2	$\rho_{0,c}/1000$	ρ_0
90	11	3.85	3.30±0.46	0.55± 0.05	4.30±0.43	11.1±0.6	4911±74	3.27±0.46	0.57± 0.05	4.01±0.40	11.7±0.6	4948±74
	17	5.98	5.46±0.44	0.51± 0.04	4.91±0.34	9.1±0.4	4860±97	5.69±0.46	0.59± 0.04	4.45±0.31	10.4±0.4	4902±98
	20	7.05	6.27±0.44	0.54± 0.03	4.52±0.27	9.1±0.5	4825±96	6.41±0.44	0.54± 0.03	4.68±0.28	8.9±0.4	4842±97
75.5	11	3.63	3.14±0.94	0.55±0.07	4.30±0.69	10.3±1.2	4880±73	3.24±0.97	0.60±0.07	4.08±0.65	11.0±1.3	4864±73
	17	5.60	4.92±0.69	0.54±0.04	4.45±0.36	9.7±0.6	4792±96	4.94±0.69	0.55±0.04	4.45±0.31	9.9±0.6	4827±97
	20	6.60	5.79±0.46	0.53±0.03	4.60±0.18	9.0±0.4	4773±95	5.93±0.47	0.55±0.03	4.52±0.18	9.5±0.4	4809±96
28.2	11	0.86	1.14±0.97	0.46±0.35	7.94±16	7.1±21	5136±77	1.08±0.92	0.52±0.40	6.61±13	8.0±24	5084±76
	17	1.34	1.28±0.70	0.59±0.37	4.45±13	10.5±37	5031±101	1.52±0.84	0.56±0.35	5.56±17	8.2±29	4978±100
	20	1.57	1.78±0.80	0.55±0.10	5.64±7.33	7.7±10	5002±100	1.83±0.82	0.56±0.10	5.73±7.44	7.6±9.9	4936±99

Table 4.9: Quantified results from phantom images of the reduced 100×100 matrix size at three different echo times and three orientations. Two different slices, 12 and 16, were analyzed. The theoretical value of $\Delta\chi$ is still 0.58 ± 0.05 ppm but the cross-sectional area becomes $2.90 \pm 0.03\,\mathrm{mm}^2$. The SNR outside the straw for all three echo times is about 77:1. The SNR values inside the straw at three echo times, 11, 17, and 20 ms, are about 123:1, 113:1, and 108:1, respectively. The meaning of each column has been explained in Table 4.7.

			Slice number 12					Slice number 16				
Angle (degree)	T_E (ms)	$\wp$ (rad·mm^2)	$\wp$ (rad·mm^2)	$\Delta\chi$ ppm	A_0 mm^2	$\rho_{0,c}/1000$	ρ_0	$\wp$ (rad·mm^2)	$\Delta\chi$ ppm	A_0 mm^2	$\rho_{0,c}/1000$	ρ_0
90	11	2.35	1.87±0.54	0.50±0.14	2.66±0.82	17.2±2.7	7953±119	2.03±0.51	0.57±0.17	2.54±0.79	19.1±3.0	8034±120
	17	3.64	3.62±0.43	0.55±0.05	3.02±0.30	17.0±1.2	7795±156	3.52±0.46	0.53±0.05	3.08±0.31	16.2±1.1	7900±157
	20	4.30	3.86±0.54	0.55±0.06	2.78±0.28	16.0±1.4	7943±159	4.08±0.49	0.54±0.05	2.95±0.30	15.2±1.4	7947±158
75.5	11	2.21	1.99±0.98	0.54±0.24	2.78±1.42	18±8	7921±119	2.03±0.99	0.61±0.27	2.54±1.30	20±6	7921±119
	17	3.42	3.31±0.86	0.51±0.12	3.20±0.80	15.4±1.8	7783±156	3.20±0.83	0.55±0.13	2.83±0.71	17.0±2.0	7883±158
	20	4.03	3.60±0.86	0.54±0.12	2.77±0.67	15.8±2.2	7757±155	3.81±0.91	0.55±0.13	2.90±0.69	15.4±2.2	7828±156
28.2	11	0.53	0.57±1.14	0.57±1.14	3.20±19.2	16±128	8279±124	0.67±1.34	0.58±2.32	3.66±22.0	14±113	8275±124
	17	0.81	0.87±0.77	0.57±0.39	3.14±5.97	15±23	8279±166	0.94±0.84	0.56±0.39	3.46±6.58	14±21	8180±164
	20	0.96	1.21±0.39	0.53±0.13	4.01±4.41	11.2±11.2	8270±165	1.14±0.36	0.55±0.13	3.66±4.03	12.5±12.5	8156±163

Chapter 5

SUSCEPTIBILITY AND SIZE QUANTIFICATION OF SMALL HUMAN VEINS FROM AN MRI METHOD

5.1 Introduction

Measuring oxygen saturation can provide an important clinical diagnostic tool. Susceptibility of the venous blood is directly related to the oxygenation level of the blood, (e.g., [29, 12]). Several groups have developed methods to quantify the susceptibility of veins [13, 14, 52, 53, 15, 35, 38, 43, 44, 54, 55, 56]. Some researchers have measured the susceptibility of veins using complex images from multi-echo gradient echo sequences [14, 15], while others have estimated venous susceptibility values only from phase information [52, 53, 55, 56]. Sedlacik et. al. [15] has quantified the susceptibilities and sizes of veins by fitting the oscillating signals from 20-echo gradient echo images. The main disadavntage of their method is the long scan time. The susceptibilities of veins have also been quantified using quantitative susceptibility mapping (QSM) techniques [35, 38, 43, 44, 55]. However, the accuracy of quantified susceptibility of a cylindrical object decreases when the size of the object decreases [35, 10], mainly due to partial-voluming. We have developed an alternate method (CISSCO) of quantifying magnetic moment, susceptibility, and the size of the narrow cylindrical object [7, 8, 10] even if they are partial volumed. The results from CISSCO can differ from the expected susceptibilities by 5% but other QSM methods can differ by 30% [10]. However, before CISSCO can be used practically, the problems connected with local phase induced from other tissues, low SNR of veins at long echo times, and little (or no) phase information outside veins at low orientations must be dealt with.

In this paper, we have improved our CISSCO method by using double echo gradient echo images for the quantifications of venous susceptibilities and sizes. Practically, as long as the ratio of the length to the diameter of a vein is at least 5:1, we can model the middle portion of the vein as an infinitely long cylinder. Finally, based on uncertainty analyses, we suggest imaging parameters and procedures for susceptibility and radius quantifications of veins at 3 T.

5.2 Material and Methods

5.2.1 Theory: susceptibility quantification of a cylindrical object with an MR signal

A more complete description of our original CISSCO method for susceptibility quantification of a cylindrical object with an MR signal has been presented in [10]. Here we summarize the major points and equations. Our method adds up complex MR signals around a cylindrical object of interest and equates that complex sum to equations containing the unknown susceptibility value and radius of the cylinder. We then systematically solve the unknowns.

If the radius of a cylindrical object is a, the overall MR complex signal S within a coaxial cylinder with radius R is

$$S = \pi \ell \rho_0 \wp \int_{\wp/R^2}^{g'} \frac{dx}{x^2} J_0(x) + \pi \ell a^2 \rho_{0,c} e^{i\,\phi_{in}} \tag{5.1}$$

with

$$\phi_{in} \equiv -\gamma \frac{\Delta\chi}{6}(3\cos^2\theta - 1) B_0 T_E \equiv \frac{g}{3}(1 - 3\cos^2\theta) \tag{5.2}$$

where ℓ is the slice thickness of the image or can be an arbitrary length of the cylindrical object, ρ_0 is the effective spin density of the tissue outside the object, $\rho_{0,c}$ is the effective

spin density inside the object, $\wp$ is the effective magnetic moment, which can be expressed by $\wp \equiv ga^2 \cdot \sin^2\theta \equiv g'a^2$, $g' \equiv g \cdot \sin^2\theta$ is the extremum phase value at the surface of the object, θ is the orientation of the cylinder (see Fig. 5.1a) and can be estimated from images [10], $g \equiv 0.5\gamma B_0 \Delta\chi T_E$, γ is the proton gyromagnetic ratio ($2\pi \cdot 42.58$ MHz/T), B_0 is the main magnetic field, $\Delta\chi$ is the susceptibility difference between the regions inside and outside the object (hereafter, $\Delta\chi$ refers to susceptibility), T_E is the echo time, and J_0 is the zeroth order Bessel function. The complex signal S can be directly calculated from images. Note that our effective magnetic moment $\wp$ is linearly proportional to T_E

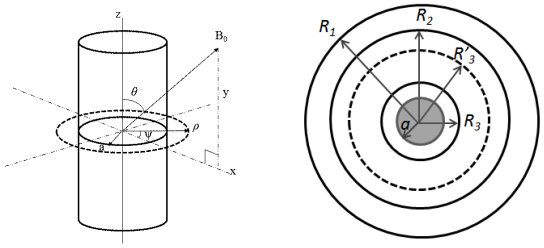

(a) (b)

Figure 5.1: (a) A cylinder has an orientation θ away from the main field. (b) A schematic drawing shows the cross section of a cylindrical object with radius a, enclosed by four coaxial pseudo cylinders whose radii are R_3, R'_3, R_2, and R_1. The MR signal within each pseudo cylinder is S_3, S'_3, S_2, and S_1, respectively.

and the word "effective" is dropped hereafter. Four unknowns in Eq.(5.1) are the radius, susceptibility, and two spin densities ($\rho_{0,c}$ and ρ_0). The two effective spin densities depend on imaging parameters, actual spin densities, and relaxation times T_1 and T_2. Eq.(5.1) is valid only when the image slice is perpendicular to the axis of the cylindrical object. We have adopted SI units throughout this paper.

If we choose three coaxial cylinders with radii $R_1 > R_2 > R_3$ around the cylinder of interest in Fig. 5.1(b), with the use of Eq.(5.1), we can write down the following equation with $\wp$ being the only unknown and solve it

$$Re(S_1 - S_2) \int_{\wp/R_3^2}^{\wp/R_2^2} \frac{dx}{x^2} J_0(x) = Re(S_2 - S_3) \int_{\wp/R_2^2}^{\wp/R_1^2} \frac{dx}{x^2} J_0(x) \tag{5.3}$$

Then we can solve for ρ_0 from $Re(S_1 - S_2)$ using Eq.(5.1).

After solving $\wp$ and ρ_0, by eliminating $\pi \ell a^2 \rho_{0,c}$ in Eq.(5.1), the complex signal S can be rewritten in terms of the the susceptibility $\Delta\chi$ as

$$Re(S) \sin\phi_{in} = Im(S)\ \cos\phi_{in} + \pi \ell \rho_0 \wp\ \sin\phi_{in} \int_{\wp/R^2}^{g'} dx J_0(x)/x^2 \tag{5.4}$$

where $Re(S)$ and $Im(S)$ are the real part and the imaginary part of the complex signal S, respectively. Both values are directly calculated from images. After solving for $\Delta\chi$, we can solve radius a from $\sqrt{\wp/g'}$ [10].

Solution of the measured susceptibility

In theory, Eq.(5.4) should lead to a solution of the measured susceptibility $\Delta\chi$. However, due to the presence of noise in images, it is possible that we cannot obtain a solution from Eq.(5.4). In other words, $h(\Delta\chi)$ defined in the following equation rewritten from Eq.(5.4) is not zero.

$$h(\Delta\chi) \equiv Re(S) \sin\phi_{in} - Im(S)\ \cos\phi_{in} - \pi \ell \rho_0 \wp\ \sin\phi_{in} \int_{\wp/R^2}^{g'} dx J_0(x)/x^2 \tag{5.5}$$

In this situation, we can derive the uncertainty of Eq.(5.5) (see I)

$$\delta h(\Delta\chi)_{max} = \sqrt{(\sigma\ell\sqrt{\Delta x\Delta y\pi R^2})^2 + (\delta\wp)^2\left(\pi\ell\rho_0\sin\phi_{in}\left(\frac{J_0(\wp/R^2)}{\wp/R^2} - \int_{\wp/R^2}^{g'} dx\,\frac{J_0(x)}{x^2}\right)\right)^2} \tag{5.6}$$

where Δx and Δy are in-plane resolutions, σ is the standard deviation of the signal, and $\delta\wp$ is the uncertainty of the magnetic moment. The goal is to estimate $\Delta\chi$, which is not known yet. If we plot $h(\Delta\chi) \pm \delta h(\Delta\chi)$ as a function of $\Delta\chi$ and search for the range of $\Delta\chi$ when $h(\Delta\chi) \pm \delta h(\Delta\chi) = 0$, then the center of the $\Delta\chi$ range can be considered as the measured $\Delta\chi$. In addition, half of the $\Delta\chi$ range can also be considered as the uncertainty of $\Delta\chi$.

Improved procedures for susceptibility quantification of objects at large orientations

When a cylindrical object with a large orientation relative to the main field has sufficient phase values and SNRs both inside and outside, our above procedures can solve the susceptibility and radius of the object from a single echo gradient echo image [10]. However, for susceptibility quantifications of veins, SNRs inside veins (i.e., $\rho_{0,c}/\sigma$) can be low at long echo times. The lower the SNR is inside a vein, the larger the uncertainty of the measured susceptibility. For example, if the SNR inside a vein is lower than 3:1, the uncertainty of the susceptibility can be higher than 50%. Using gradient echo images from two echoes can reduce the uncertainty of the measured susceptibility. We can first quantify the magnetic moment $\wp$ of a given vein using Eq.(5.3) from the longer echo time, as the uncertainty of $\wp$ at the longer echo time is smaller [8]. Then we scale the mag-

netic moment to the shorter echo time and solve the susceptibility of the same vein using Eq.(5.4) at the shorter echo time. This is because at the shorter echo time, we have a higher SNR inside the vein for more accurate susceptibility quantification. However, this echo time cannot be too short, as we still need sufficient phase value and SNR inside the vein.

Solving susceptibilities of objects at small orientations

This scenario and its mathematical derivations have been described in [10]. Briefly, as little or no phase distributions are outside cylindrical objects at small orientations relative to the main field, it is very difficult to accurately quantify the magnetic moment. We can bypass this problem with the following approach. Consider the expansion of Eq.(5.4)

$$Re(S_n)\sin\phi_{in,n} = Im(S_n)\cos\phi_{in,n} + \pi\ell\rho_{0,n}\sin\phi_{in,n}(R^2 + \frac{g_n'^2a^4}{4R^2} - a^2 - \frac{g_n'^2a^2}{4}) \tag{5.7}$$

where the subscript n is referred to each variable obtained at the n^{th} echo time T_{E_n}. Applying two coaxial cylinders to images acquired at each echo time, we can first solve each $\rho_{0,n}$. Then using images from different echo times, we can solve the susceptibility and cross-sectional area of the object of interest from the following equation and Eq.(5.7) through an iterative procedure

$$\begin{aligned}
&(\rho_{0,2}Re(S_1) - \rho_{0,1}Re(S_2))\sin(\phi_{in,1})\sin(\phi_{in,2}) = \\
&\quad \pi\ell\rho_{0,1}\rho_{0,2}\sin(\phi_{in,1})\sin(\phi_{in,2})\frac{a^2}{4}(1 - \frac{a^2}{R^2})(g_2'^2 - g_1'^2) \\
&\quad +\rho_{0,2}Im(S_1)\sin(\phi_{in,2})\cos(\phi_{in,1}) - \rho_{0,1}Im(S_2)\sin(\phi_{in,1})\cos(\phi_{in,2})
\end{aligned} \tag{5.8}$$

Due to little phase outside the vein, we visually determined the center of the vein. The slightly inaccurate determination of the center would not alter our quantified results later. We selected two disk areas, $A_1 > A_2$, centering around the vein and we summed up the overall complex signals U_1 and U_2 within the areas. Note that for biological tissues, the susceptibility solved from Eq.(5.8) is unique [10]. After solving for $\Delta\chi$ and πa^2, $\rho_{0,c}$ can be solved from the imaginary part $Im(S) = \pi\ell a^2\rho_{0,c}\sin\phi_{in}$ of the image.

5.2.2 Revisions of our method due to the presence of a local uniform field

Even if we can precisely remove the background fields due to air/tissue interfaces, susceptibility differences between tissues will still produce fields around the vein of interest. Thus, we need to take this into account in our equations. As the phase induced by other tissues in the local area around the vein of interest perhaps varies slowly, we may approximate that phase to be a constant, ϕ_{bkg}. As a result, the complex signal S shown in Eq.(5.1) becomes $U = Se^{i\phi_{bkg}}$. This local background phase does not affect the quantification of magnetic moment. We will explain the reason in section 5.2.2. However, the background field could affect the accuracy of searching the center of the object and will definitely affect the susceptibility quantification. The following three subsections describe the effects on the center determination and magnetic moment. We will also show how to estimate this local background phase.

Identification of the center of the object

In our procedures, we first need to determine the center of a given object. We can identify the center by minimizing the overall real part of the complex signal within a circle enclosing the object [8]. This circle has a radius R and is chosen by us. With the existence

of ϕ_{bkg}, this procedure may fail. However, from J, we have proved that if $|\phi_{bkg}|$ is less than $\pi/4$ and if the maximal phase value at the boundary of the circle ($|\wp/R^2|$) is less than 2.63 radians, then our original procedure of finding the center of the object will still be valid.

Magnetic moment quantification

With the existence of ϕ_{bkg}, the overall signal in an annular region becomes

$$U_j - U_i = e^{i\,\phi_{bkg}} \pi \ell \rho_0 \wp \int_{\wp/R_j^2}^{\wp/R_i^2} \frac{dx}{x^2} J_0(x) \tag{5.9}$$

where the subscripts i and j refer to different coaxial cylinders or concentric circles. The magnetic moment can again be solved by using Eq.(5.3). It should be clear that ϕ_{bkg} cancels out in Eq.(5.3) and it does not change the solution of Eq.(5.3). Alternatively, we can also replace $Re(U_j - U_i)$ in Eq.(5.3) by $|U_j - U_i|$.

Local background phase estimation

Since the imaginary part of the overall signal within a coaxial cylinder only comes from the object itself (see Eq.(5.1)), we can calculate ϕ_{bkg} from the annular region between R_2 and R_3. From Eq.(5.9),

$$\phi_{bkg} = \tan^{-1} \frac{Im(U_2 - U_3)}{Re(U_2 - U_3)} \tag{5.10}$$

After estimating ϕ_{bkg}, we subtract ϕ_{bkg} from the phase image, and then calculate the complex signal S. Next, we quantify the magnetic moment with Eq.(5.3) and other unknowns including the susceptibility.

If the orientation of an object is small, such that no sufficient phase distribution is outside the object, we can still consider an annular region around the object and use Eq.(5.10) to estimate ϕ_{bkg}. In this case, the signal symbol U represents the complex signal summed around the object. In fact, the area that leads to the signal U does not need to be a circular region. In addition, we do not need to identify the center of the object in this case.

5.2.3 Simulations

All of our following simulations, except for those in the high pass filter studies, assumed a main field of 3 T, $\Delta\chi$ of 0.4 ppm, and radius of the object $a = 1$ pixel. In those simulations, the orientation of the object was perpendicular to the main field, except for two cases where the objects had relatively small orientations (10° and 30°). We simulated each cylindrical object on a 4096×4096 matrix and converted the matrix to 256×256 through Fourier transformation. We also added the Gaussian noise in images such that ρ_0/σ is 10:1 at $T_E = 0$ ms, with an infinite T_2. Similarly, $\rho_{0,c}/\sigma$ is 9:1 at $T_E = 0$ ms, with a $T_2^\star$ of the object to be 24 ms. Detailed descriptions of these procedures can be found in [8, 10]. From $\rho_{0,c}$ at $T_E = 0$ ms and the $T_2^\star$ value, with σ assigned to be unity, $\rho_{0,c}$ were 4.4, 3.3, and 2.6 at $T_E = 17$ ms, 24 ms, and 30 ms, respectively. These were the echo times selectively used in the following scenarios, except for the high pass filter studies.

Presence of the local background field

In order to validate our ideas presented in Section 5.2.2, in this subsection we purposely added a local background phase of 0.1 radian into simulated images at $T_E = 24$ ms. We estimated the local background phase using Eq.(5.10). Then we quantified the mag-

netic moment from Eq.(5.3), susceptibility value from Eq.(5.4), and other unknowns, with and without the removal of the background phase.

Susceptibility quantification at large orientations

We simulated two sets of images at $T_E = 17$ ms and $T_E = 30$ ms for an object perpendicular to the main field. The magnetic moment $\wp$ at $T_E = 30$ ms was first quantified from Eq.(5.3). We then scaled $\wp$ to the value at $T_E = 17$ ms. From the images at $T_E = 17$ ms, we quantified the susceptibility.

Susceptibility quantification at low orientations

In this set of simulations, we simulated two objects. One object was simulated with an orientation of 10° at $T_E = 17$ ms and $T_E = 24$ ms. The other object had an orientation of 30° but was simulated at two different echo time combinations, $T_E = 17$ ms and $T_E = 24$ ms, and $T_E = 17$ ms and $T_E = 30$ ms. We quantified susceptibility, cross-sectional area, and two spin densities of these three cases with Eq.(5.7) and Eq.(5.8).

Influence of the high pass filter

For this set of studies, we simulated cylindrical objects at $B_0 = 3$ T, $\Delta\chi = 0.4$ ppm, $a = 1$ pixel and 3 pixels, and $T_E = 10$, 20, 30, 40, and 50 ms. Both perpendicular and parallel orientation were simulated on 1024×1024 matrices which were further converted to 64×64 matrices through Fourier transformations. No Gaussian noise or T_2 decay were included in any of these simulated images. We chose $\rho_0 = \rho_{0,c} = 10$.

We applied the homodyne high pass filter (16×16) to these simulated images. In order

to study the high pass filter effect, we quantified and compared the magnetic moment of each object at perpendicular orientation with and without the application of the high pass filter. In addition, we also compared the phase value inside each object at both orientations with and without the high pass filter. If the magnetic moment and phase value inside each object do not change before and after the application of the high pass filter, then we know the high pass filter has no influence onto our quantifications of the magnetic moment and susceptibility. Given the convenient use of the high pass filter, we chose the high pass filter in this work over other background phase removal methods.

Table 5.1: Simulated results of magnetic moments of cylindrical objects and phase values inside objects, at different echo times. The radii of these objects were 1 pixel and 3 pixels. The orientations of the objects were 90° and 0°. Theoretical values, results without using the high pass filter, and results using the high pass filter are listed. The first column lists the radius a of the object. The second column lists T_E. The third, sixth, and ninth column show the magnetic moments $\wp$. The fourth, seventh, and tenth column list phase values inside objects perpendicular to the field. The fifth, eighth, and eleventh column list phase values inside objects parallel to the field. Uncertainties of these quantified results are not shown.

		Theory			No high pass filter			High pass filter		
a	T_E	$\wp$	ϕ_{90}	ϕ_0	$\wp$	ϕ_{90}	ϕ_0	$\wp$	ϕ_{90}	ϕ_0
pixel	ms	rad·pixel^2	rad	rad	rad·pixel^2	rad	rad	rad·pixel^2	rad	rad
1	10	1.61	0.54	-1.07	1.79	0.39	-0.58	1.89	0.35	-0.52
1	20	3.21	1.07	-2.14	3.55	0.55	-1.45	3.54	0.55	-1.41
1	30	4.82	1.61	-3.21	5.16	1.45	-4.53	5.11	1.55	-4.56
1	40	6.42	2.14	-4.28	6.66	1.96	-4.89	6.53	1.95	-5.00
1	50	8.02	2.68	-5.35	8.26	2.32	-5.62	7.99	2.50	-5.30
3	10	14.4	0.54	-1.07	14.9	0.53	-1.05	14.7	0.34	-0.71
3	20	28.9	1.07	-2.14	29.2	1.08	-2.11	27.0	0.59	-1.60
3	30	43.3	1.61	-3.21	43.8	1.59	-3.26	36.1	0.54	-3.27
3	40	57.8	2.14	-4.28	58.2	2.16	-4.32	41.8	0.34	-4.80
3	50	72.2	2.68	-5.35	72.8	2.72	-5.36	45.3	0.10	-5.65

5.2.4 Re-examination of phantom images with an object at a low orientation

In our previous work [10], we applied the methods described in Sec. 5.2.1 to objects at the parallel orientation. Here, we want to show that those methods are also applicable

to objects at low orientations. Thus, we re-examined phantom images in [10] with a straw oriented at 28.2° from the main field and filled by the Gadolinium solution with a theoretical $\Delta\chi = 0.58 \pm 0.05$ ppm. The diameter of the straw was 4.92 ± 0.02 mm, which led to a cross-sectional area of 19.0 ± 0.2 mm^2. The images were acquired from a single-echo 3D gradient echo sequence on 3 T, repeated three times with three different echo times: $T_E = 11$ ms, 17 ms, and 20 ms. The image resolution was 1 mm isotropic. We quantified susceptibilities and radii of the straw from two slices (number 12 and 16) for comparisons. For each slice, we obtained quantified values from two sets of echo time combinations. One set used $T_E = 11$ ms and 17 ms and the other set used $T_E = 11$ ms and 20 ms.

The background phase of those phantom images were already removed by a manual phase unwrapping method and a 2D quadratic fitting program. Thus, we did not apply the high pass filter to those images. An example of the magnitude and phase image of the Gd-DTPA doped straw are shown in Fig. 5.2a and Fig. 5.2b.

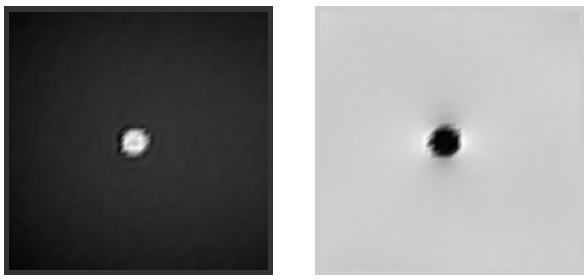

(a) (b)

Figure 5.2: (a) The magnitude and (b) its associated filtered phase image at echo time 20 ms acquired from a 3 T machine. The straw filled with Gd-DTPA solution had a diameter of 4.92 ± 0.02 mm. The straw was immersed in a gel phantom and had an orientation of 28.2° to the main field.

5.2.5 Uncertainties of susceptibility and other unknowns

The two major independent noise sources contributing uncertainties in our quantified results are from the Gaussian noise and the systematic noise due to discrete pixels, partial

volume effect, and Gibbs ringing in images. Uncertainties of quantified unknowns can be derived from the error propagation method [18]. These have been discussed in the past (e.g. [10]). However, if the choice of radius $R \equiv R_3'$ used in Eq.(5.4) is larger than R_3 (see Fig. 5.1(b)), which is used to quantify the magnetic moment, then we need to rederive the uncertainties of the measured susceptibility value, the cross-sectional area of the object, and the spin density inside the object. In this scenario, as the annular region between R_3' and R_3 overlaps with the annular region between R_2 and R_3, we must rewrite $\delta(S_2 - S_3)$ in terms of $\delta(S_3' - S_3)$ and $\delta(S_2 - S_3')$, where the signal S_3' is the overall complex signal within R_3'. In K, we show the uncertainties of quantified variables when $R_2 > R_3' > R_3$.

In this work, we use a two-echo approach to solve susceptibilities of cylindrical objects. As we quantify magnetic moment and susceptibility from two different images, no correlation is between measured results. We provide uncertainty formulas in L and M. For cylindrical objects at low orientations, we derive uncertainties of the susceptibility and the cross-sectional area ($\delta\Delta\chi/\Delta\chi$ and $\delta A_0/A_0$) by varying susceptibility and area in Eq.(5.7). We treat $\delta\Delta\chi/\Delta\chi$ and $\delta A_0/A_0$ as two unknowns in a new set of linear equations derived from the variations of Eq.(5.7). Then we solve $\delta\Delta\chi/\Delta\chi$ and $\delta A_0/A_0$ simultaneously from this new set of linear equations. We evaluate these two uncertainties through the error propagation method.

5.2.6 *In vivo* MR data collection and processing

We applied our methods to several isolated veins (see Figs. 5.3 and 5.4) from branches of anterior, inferior, superior cerebral veins, and transverse sinus, which were from two sets of existing MR images [35, 38]. A 3D gradient echo single-echo sequence with velocity compensation in all three directions was used for the acquisitions of both datasets.

One set of the images was acquired from a female volunteer at a 3.96 T Bruker machine. A single channel birdcage head coil was used in this case. The imaging parameters were: isotropic resolution 0.5 mm, $T_E = 11.6$ ms and 19.2 ms, $T_R =$ 26.0 ms, flip angle = 11°, read bandwidth = 120 Hz/pixel and field of view = 256 mm $\times$ 176 mm $\times$ 45 mm. The k-space data were used for analyses. The scan was performed twice, but individually for each echo time.

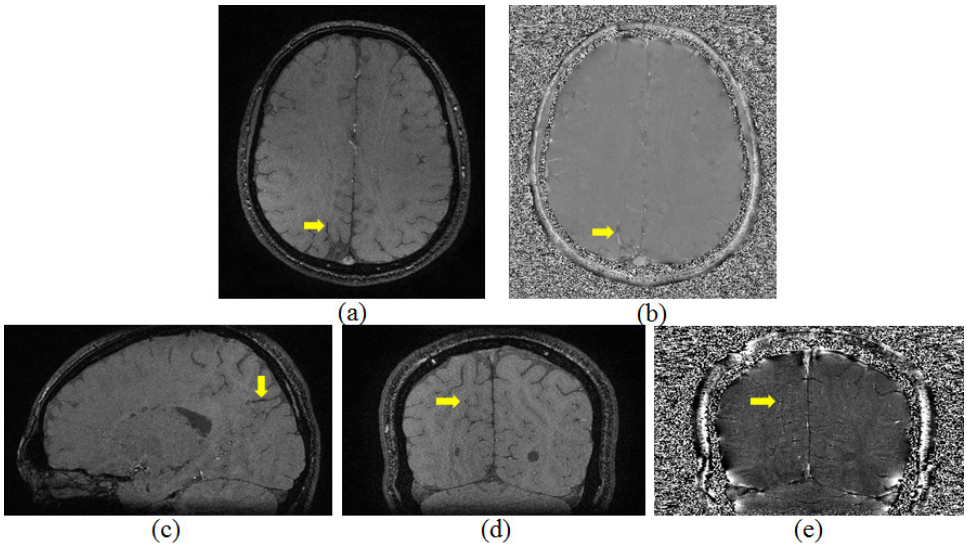

Figure 5.3: A set of 3D gradient echo images at $T_E = 17.3$ ms from 2.89 T shows a vein, whose susceptibility has been analyzed. (a) Magnitude and (b) its associated phase image from a volunteer. (c) Sagittal view of the same vein as shown in (a) and (b). The orientation of this vein is $80^\circ \pm 3^\circ$ to the main field. The same vein is also displayed in the coronal (d) magnitude and (e) its associated phase image.

The other set of images was acquired from a male volunteer at a 2.89 T Siemens VERIO machine. A 12-channel head coil was used in this case. The imaging parameters were: isotropic resolution 0.5 mm, $T_E = 14.3$ ms and 17.3 ms, $T_R = 26$ ms, flip angle = 15°, read bandwidth = 121 Hz/pixel, and field of view = 256 mm $\times$ 184 mm $\times$ 128 mm. Only combined magnitude and phase images were saved for this scan. The images were also acquired twice, one from each individual echo time.

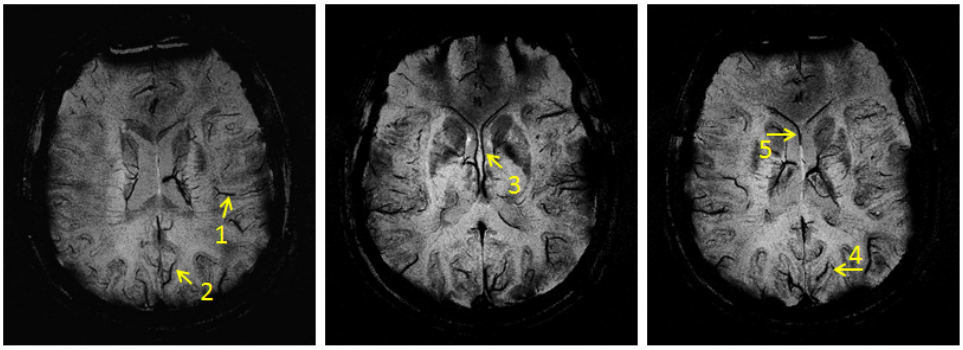

Figure 5.4: A set of SWI images having minimal intensity projections (mIP) over 8 slices at $T_E = 19.2\,\text{ms}$ from $3.96\,\text{T}$ shows a total of five well-separated veins. Quantified results of those veins are listed in Table 5.6. The mIP images help to display the entire length of each vein, which is not necessarily lying on the original transverse plane. Results of these veins are given in the first 5 rows in Table 5.6.

With these two sets of existing images, we first displayed each vein of interest from the transverse, coronal, and sagittal plane. Figure 5.3 shows an example. Then we estimated the direction and orientation of the vein from those three imaging planes. The detailed procedure of estimating the orientation of a cylindrical object was given in [10]. We summarize other post-processing procedures in the flow chart in Fig. 5.5. For comparisons, we also solved for the susceptibility of the vein from Eq.(5.4) at the longer echo time. In some cases, R_3' was chosen between R_2 and R_3.

5.3 Results

In this section, we present results of quantified magnetic moments, susceptibility values, cross-sectional areas of cylindrical objects, and spin densities from simulations, previous phantom images, and existing human data.

5.3.1 Simulations

Presence of the local background field

With the assigned local background phase of 0.1 radian, we have estimated a local background phase of 0.10 radian using radii 1.5 pixels and 2.5 pixels in Eq.(5.10). The measured magnetic moments are the same with and without the correction of the local background phase. However, the quantified susceptibility value and other parameters are improved with the correction of the local background phase (see Table 5.2). This shows that it is necessary to correct a small local background phase.

Table 5.2: Quantified results from simulated images at $T_E = 24$ ms and with an orientation of 90°. The actual values are $\wp = 3.85$ rad·pixel^2, $\Delta\chi = 0.4$ ppm, $A = 3.14$ pixel^2, $\rho_0 = 10.0$, and $\rho_{0,c} = 3.31$. The second column lists the magnetic moment. The third column lists the susceptibility value. The fourth column lists the cross-sectional area, A. The fifth column lists the effective spin density inside the object. The sixth column lists the effective spin density outside the object. The results at the third row are before the removal of the local background phase. The results at the fourth row are after the removal of the local background phase, which is calculated from Eq. (5.10).

	$\wp$	$\Delta\chi$	A	$\rho_{0,c}$	ρ_0
unit	rad·pixel^2	ppm	pixel^2		
Before	3.82	0.44	2.84	5.54	9.91
After	3.82	0.40	3.14	2.80	9.95

Susceptibility quantifications at large orientations

Using the quantified magnetic moment from $T_E = 30$ ms scaled to that at $T_E = 17$ ms as an input to Eq.(5.4), the precision of the measured susceptibility at $T_E = 17$ ms is improved. The quantified magnetic moment at $T_E = 30$ ms is 4.86 ± 0.34 rad·pixel^2, compared to the input value of 4.82 rad·pixel^2. Table 5.3 lists the magnetic moment directly quantified from $T_E = 17$ ms or scaled from $T_E = 30$ ms, and their associated susceptibilities and

cross-sectional areas solved from Eq.(5.4).

Table 5.3: Quantified results from simulated images at $T_E = 17\,\text{ms}$ and with an orientation of 90°. The theoretical values of input parameters are given in the caption of Table 5.2. The second column lists the magnetic moment, $\wp$. The third column lists the susceptibility value. The fourth column lists the cross-sectional area, A. The magnetic moment in the third row was quantified directly from Eq.(5.9). The theoretical value of $\wp$ at T_E =17 ms is 2.73 rad·pixel^2. The magnetic moment in the fourth row was scaled by the magnetic moment, 4.86 ± 0.34 rad·pixel^2, at T_E=30 ms.

	$\wp$ rad·pixel^2	$\Delta\chi$ ppm	A pixel^2
No scaled	2.63 ± 0.94	0.39 ± 0.12	3.08 ± 1.42
Scaled	2.75 ± 0.19	0.39 ± 0.07	3.25 ± 1.69

Susceptibility quantifications at low orientations

The results of measured susceptibility values agree with the theoretical value within 5%. The quantified cross-sectional areas of the objects agree with the input value within 8%. These results are shown in Table 5.4. We also find that this approach is suitable for objects with orientations up to 40°.

Table 5.4: Quantified results from simulated images using the low orientation method. The first column lists the orientation. The second column lists T_E. The third column lists $\Delta\chi$ solved from Eq.(5.8). Numbers inside parentheses show the two echo times used for calculating the susceptibility. The theoretical value of $\Delta\chi$ is 0.4 ppm and the theoretical cross-sectional area is 3.14 pixel^2. The chosen radius, R, for solving Eq.(5.8) is 1.5 pixel. The fourth column lists the cross-sectional area of the cylinder calculated from Eq.(5.7). The fifth column lists the effective spin density inside the object calculated from the imaginary part used in Eq.(5.7). The sixth column lists the quantified effective spin density outside the object.

Angle Degree	T_E ms	$\Delta\chi$ ppm	A pixel^2	$\rho_{0,c}$	ρ_0
10	17	0.41 ± 0.03 (17/24)	3.27 ± 0.78	4.2 ± 1.6	9.89 ± 0.20
	24		3.14 ± 0.75	3.4 ± 1.6	9.89 ± 0.20
30	17	0.42 ± 0.13 (17/24)	3.14 ± 1.70	4.2 ± 1.7	9.89 ± 0.20
	24		2.96 ± 1.60	4.5 ± 2.8	9.88 ± 0.20
30	17	0.42 ± 0.05 (17/30)	2.89 ± 0.84	4.2 ± 1.2	9.79 ± 0.20
	30		2.96 ± 0.86	2.5 ± 1.1	9.76 ± 0.20

Influence of the high pass filter

For cylindrical objects whose radii are 1 pixel, quantified magnetic moments and phase values are almost the same with or without the application of the high pass filter (see Table 5.1). It indicates that quantifications of small objects are not affected by the high pass filter. Therefore, our $in\text{-}vivo$ results are unlikely affected by the chosen size of the high pass filter. We note that due to the partial volume effect, some measured phase values inside objects can be much smaller than the actual phase values. However, quantified susceptibility values using our method still agree well with input values.

For cylindrical objects whose radii are 3 pixels, quantified magnetic moments using our method with or without the application of the high pass filter can become very different when the echo time is 30 ms or longer (see Table 5.1). In addition, even at $T_E = 10$ ms, measured phase values (from central pixels completely inside each object) can already be different with the use of the high pass filter. This shows that the high pass filter can influence susceptibility quantification when an object is slightly large.

With the applications of the high pass filter, if a phantom or a brain does not occupy the entire image, our further simulations show that the phase value inside a cylindrical object can be further reduced. The reduction depends on the phantom size (or the brain size), object size, object orientation, the original phase value inside the object, or the size of the high pass filter. This was the reason why we cropped the human images before we applied the high pass filter.

5.3.2 Re-examination of the previous phantom images

Table 5.5 lists phantom results from an object at the low orientation ($28.2°$). The differences between the quantified susceptibility values and the expected value (0.58 ppm) are less than 10%. However, the differences between the measured cross-sectional areas and the true value ($19.0 \pm 0.2\,\text{mm}^2$) can be up to 30%. The uncertainties of these results are about one third of those results quantified from the previous single echo approach using Eq.(5.4) [10].

Table 5.5: Quantified results from phantom images with an image resolution of 1 mm isotropic, using two different echo times when the object is parallel to the main field. Two different slices have been analyzed. The theoretical value of $\Delta\chi$ is 0.58 ± 0.05 ppm and the cross-sectional area is $19.0 \pm 0.2\,\text{mm}^2$. The first column lists the echo time. The second and the sixth column list $\Delta\chi$ solved from Eq.(5.8). The chosen radius, R, for solving Eq.(5.8) is 3.0 mm. The superscripts, a and b, refer to the two echo times used for quantifying the susceptibility. The third and seventh column list the cross-sectional area of the cylinder calculated from Eq.(5.7). The fourth and eighth column list the effective spin density inside the object calculated from the imaginary part used in Eq.(5.7). The fifth and ninth column list the effective spin density outside the object.

	Slice number 12				Slice number 16			
T_E (ms)	$\Delta\chi$ ppm	Area mm^2	$\rho_{0,c}$	ρ_0	$\Delta\chi$ ppm	Area mm^2	$\rho_{0,c}$	ρ_0
11		23.4 ± 3.7	2241 ± 130	1291 ± 13		23.2 ± 3.7	2239 ± 130	1263 ± 13
17	0.55 ± 0.03^a	22.7 ± 2.3	2059 ± 160	1272 ± 13	0.56 ± 0.03^a	22.7 ± 2.3	2021 ± 160	1257 ± 13
20	0.55 ± 0.02^b	22.6 ± 2.9	1961 ± 120	1261 ± 13	0.54 ± 0.02^b	24.8 ± 3.2	2137 ± 120	1262 ± 13

Comments: $^aT_E = 11$ ms and 17 ms. $^bT_E = 11$ ms and 20 ms .

5.3.3 Results from existing human images

Our quantified susceptibility values shown in Table 5.6a in general agree with values (0.37-0.54 ppm) from other recent work [43, 55, 44]. However, our susceptibility values of 5 veins in different regions of each volunteer's brain are close to each other. The typical susceptibility value from a vein of a healthy person is about 0.41 ppm, if we assume an oxygenation level of 70%, a Hemoticrit of 40%, and a susceptibility difference between fully deoxygenated blood and oxygenated blood of 3.39 ppm [50]. From the measured

cross-sectional area of each vein in Table 5.6a, we find that the diameters of analyzed vein range from 1.2 to 3.0 pixels.

For comparisons, Table 5.6b lists the results of magnetic moments, susceptibility values, cross-sectional areas, and other variables of veins quantified from the longer echo time of each volunteer's images. We find that in general the results of susceptibility values, cross-sectional areas, and spin densities inside veins have larger uncertainties than those results in Table 5.6a. The susceptibility values in highlighted grey areas in Table 5.6 were estimated using Eq.(5.6).

For veins at low orientations, we have quantified two vessels with orientations of $20^\circ \pm 5^\circ$ and $29^\circ \pm 3^\circ$ at $T_E = 11.6$ ms from 3.96 T images. As the volunteer moved between the scans, at $T_E = 19.2$ ms, the orientation of the latter vein changed from $29^\circ \pm 3^\circ$ to $16^\circ \pm 5^\circ$, but the orientation of the former vein did not change. The susceptibility value of the former vein is 0.46 ± 0.11 ppm and its cross-sectional area is 1.54 ± 1.23 pixel^2. The susceptibility value of the latter vein is 0.43 ± 0.03 ppm and its cross-sectional area is 4.37 ± 1.18 pixel^2. These two susceptibility values are in good agreement with those shown in Table 5.6a.

We have also estimated susceptibility values of veins at low orientations from 2.89 T. However, the quantified values are about 0.6 ppm. A closer examination reveals that phase values inside those veins are much higher than the expected value at $T_E = 14.3$ ms, but are about the same as the expected values at $T_E = 17.3$ ms if a susceptibility of 0.40 ppm is assumed. After we further examine the data, we believe that this problem is due to the combination of multi-channel phase images.

5.4 Discussion

Our averaged susceptibility values of veins from Table 5.6a for two volunteers imaged at 3.96 T and 2.89 T are 0.46 ± 0.02 ppm and 0.39 ± 0.02 ppm, respectively. For the purpose of comparing results below from other groups, the calculated standard deviations here have neglected the uncertainty of the susceptibility of each vein. The standard deviation, 0.02 ppm, is smaller than those from other recent results. For example, the averaged susceptibility values of veins in each volunteer for three volunteers in the work by [43] are 0.54 ± 0.13 ppm, 0.49 ± 0.09 ppm, and 0.53 ± 0.09 ppm. Note that these averaged susceptibility values are higher than our values. In addition, the averaged diameter of quantified veins from [43] is 4.5 pixels, compared to a range of 1.2-3.0 pixels from our images.

In the work by [44], the averaged susceptibility value of 48 veins from 8 volunteers (7 of whom are male) is 0.37 ppm. The standard deviation of the susceptibility quantified from 6 cortical veins of each volunteer is between 0.04 ppm and 0.08 ppm (see Fig. 5b of [44]). In another work by [55], the averaged susceptibility value of small veins from 6 subjects is 0.45 ± 0.02 ppm. The phase and the statistical method described in [55] require subjects to breathe in PCO_2 and PO_2 independently at 7 T.

In our previous work [10], when the orientation of the cylindrical object is around the magic angle (54.7°), Eq.(5.4) cannot solve for the susceptibility of the object. However, for the vein around the magic angle, we may quantify the susceptibility of this vein by obtaining the magnetic moment in the typical gradient echo sequence and measuring the size of this vein by applying the dark blood spin echo sequence.

With uncertainty formulas given in the Appendices of this paper and in Appendix B of [10], we can optimize imaging parameters by minimizing the uncertainties of susceptibilities of small veins but keeping reasonable imaging time of a two-echo 3D gradient echo sequence. The first consideration is the image resolution. If we are interested in veins with diameters similar to those quantified in this work (at least 0.5 mm in diameter), we can reduce the isotropic image resolution to 0.6 mm. Second, if our goal is to maintain uncertainties of the susceptibility less than 35% from a 3 T machine, for most veins with a diameter of at least two pixels, SNR at least 5.7 to 1 from the shorter echo time, and with orientations either larger than 70° or smaller than 30°, we can choose T_E to be 17 ms and 24 ms. The choice of 24 ms is because this value is close to T_2^* of the venous blood [57]. The choice of 17 ms is to have some time difference away from 24 ms, but $T_E = 17$ ms is still long enough such that we have sufficient phase values inside those veins of interest. If we choose T_R to be 28 ms and a transverse scan with a field of view of 256 mm $\times$ 192 mm and a slab coverage of 128 mm, the scan time will be about 32 minutes. If we choose T_E to be 17 ms and 30 ms and T_R to be 35 ms, with other parameters being the same, the scan time will be about 40 minutes. However, the uncertainties of the susceptibility for the same veins will be reduced to 16%. This can be seen from results shown in Table 5.3 and Table 5.4. If a vein has a length to diameter ratio of more than 5:1, depending on the length of the vein, it may be possible to average quantified susceptibility values from several slices. This will further reduce the uncertainty of the measurement.

Another possible way to reduce the uncertainty of the measured susceptibility from a vein at a large orientation is to inject the contrast agent (Gd-DTPA) into subjects. Here we assume that the vessel size does not change before and after the injection. We can

first determine the size of the vein from post-contrast images and then calculate the susceptibility of the same vein from pre-contrast images. Our simulations indicate that this approach can lead to an uncertainty less than 15% with the above parameters of the vein and with $T_E = 17$ ms and 24 ms.

For the consideration of scan time, if a typical neuro protocol has covered the entire brain with either T_1-weighted or T_2-weighted sequence, then we may use these suggested parameters of the 3D gradient echo sequence to cover only a portion of the brain in which susceptibilities of veins are interested to clinicians. If we just cover 64 slices, the scan time will be less than 12 minutes. We may further reduce this scan time by enabling parallel imaging.

5.5 Conclusion

With the improved procedures that take into account practical issues in MR imaging, we have demonstrated that magnetic susceptibilities and cross-sectional areas of veins at different orientations can be quantified with reasonable accuracy and precision. The susceptibility values of different veins are almost the same for each volunteer, while the susceptibility values differ between the two volunteers in this work. We have also shown that our post processing procedures will not be affected by subject movements between scans.

Table 5.6: Magnetic susceptibility and 4 other unknowns of veins were measured from $T_E =$ 19.2 ms and 11.6 ms at 3.96 T and from $T_E = 17.3$ ms and 14.3 ms at 2.89 T. The first column lists the main field strength. The second column lists each vessel's orientation. The third column lists the magnetic moment of the vessel. Results from (a) show quantified magnetic moments from the longer echo time but other quantified parameters from the shorter echo time, by scaling the measured magnetic moments to values at the shorter echo time. On the other hand, results from (b) show quantified values all from the longer echo time. The fourth column lists $\Delta\chi$ of the venous blood. The fifth column lists the cross-sectional area of each vein. The sixth column lists the effective spin density inside each vein. The seventh column lists the effective spin density outside each vein. The last vein in the tables has different orientations, due to the movement of the volunteer between the two scans. The orientation of this vein in (a) is from the shorter echo time, while the value in (b) is from the longer echo time.

B_0	Angle (Degree)	$\wp$ rad·pixel^2	$\Delta\chi$ ppm	A_0 pixel^2	$\rho_{0,c}$	ρ_0	
4	80 ± 3	1.29 ± 0.55	0.46 ± 0.37	1.50 ± 1.79	297 ± 217	279 ± 8	
4	90 ± 1	2.01 ± 0.32	0.45 ± 0.16	2.27 ± 1.11	239 ± 98	292 ± 9	
4	75 ± 3	2.57 ± 0.31	0.45 ± 0.12	3.14 ± 1.00	384 ± 104	334 ± 10	
4	70 ± 3	1.22 ± 0.35	0.48 ± 0.34	1.45 ± 1.39	254 ± 163	323 ± 6	
4	70 ± 3	1.35 ± 0.32	0.48 ± 0.31	1.63 ± 1.38	309 ± 185	261 ± 8	(a)
3	80 ± 3	2.67 ± 0.45	0.40 ± 0.19	3.94 ± 2.48	242 ± 87	306 ± 9	
3	90 ± 1	2.30 ± 0.44	0.38 ± 0.22	3.46 ± 2.11	57 ± 30	303 ± 9	
3	80 ± 3	2.03 ± 0.45	0.36 ± 0.22	3.33 ± 2.70	164 ± 64	354 ± 11	
3	67 ± 3	3.07 ± 0.31	0.40 ± 0.20	5.15 ± 2.78	198 ± 63	227 ± 7	
3	75 ± 3	1.59 ± 0.64	0.39 ± 0.34	2.49 ± 2.99	231 ± 136	338 ± 7	

B_0	Angle (Degree)	$\wp$ rad·pixel^2	$\Delta\chi$ ppm	A_0 pixel^2	$\rho_{0,c}$	ρ_0	
4	80 ± 3	2.13 ± 0.91	0.43 ± 0.39	1.58 ± 1.57	28 ± 24	227 ± 7	
4	90 ± 1	3.32 ± 0.53	0.32 ± 0.13	3.20 ± 1.83	87 ± 54	244 ± 7	
4	75 ± 3	4.26 ± 0.51	0.70 ± 0.30	2.01 ± 0.90	143 ± 112	299 ± 7	
4	70 ± 3	2.02 ± 0.58	0.37 ± 0.21	1.91 ± 1.51	329 ± 194	281 ± 8	
4	70 ± 3	2.23 ± 0.53	0.28 ± 0.15	2.90 ± 2.00	230 ± 108	210 ± 6	(b)
3	80 ± 3	3.23 ± 0.55	0.44 ± 0.09	3.53 ± 0.92	214 ± 58	283 ± 8	
3	90 ± 1	2.78 ± 0.53	0.33 ± 0.17	3.94 ± 0.62	90 ± 36	286 ± 8	
3	80 ± 3	2.46 ± 0.54	0.36 ± 0.19	3.27 ± 1.05	118 ± 67	344 ± 10	
3	67 ± 3	3.72 ± 0.37	0.35 ± 0.21	5.90 ± 3.60	168 ± 54	220 ± 7	
3	70 ± 3	1.82 ± 0.73	0.35 ± 0.38	2.78 ± 1.78	241 ± 203	318 ± 6	

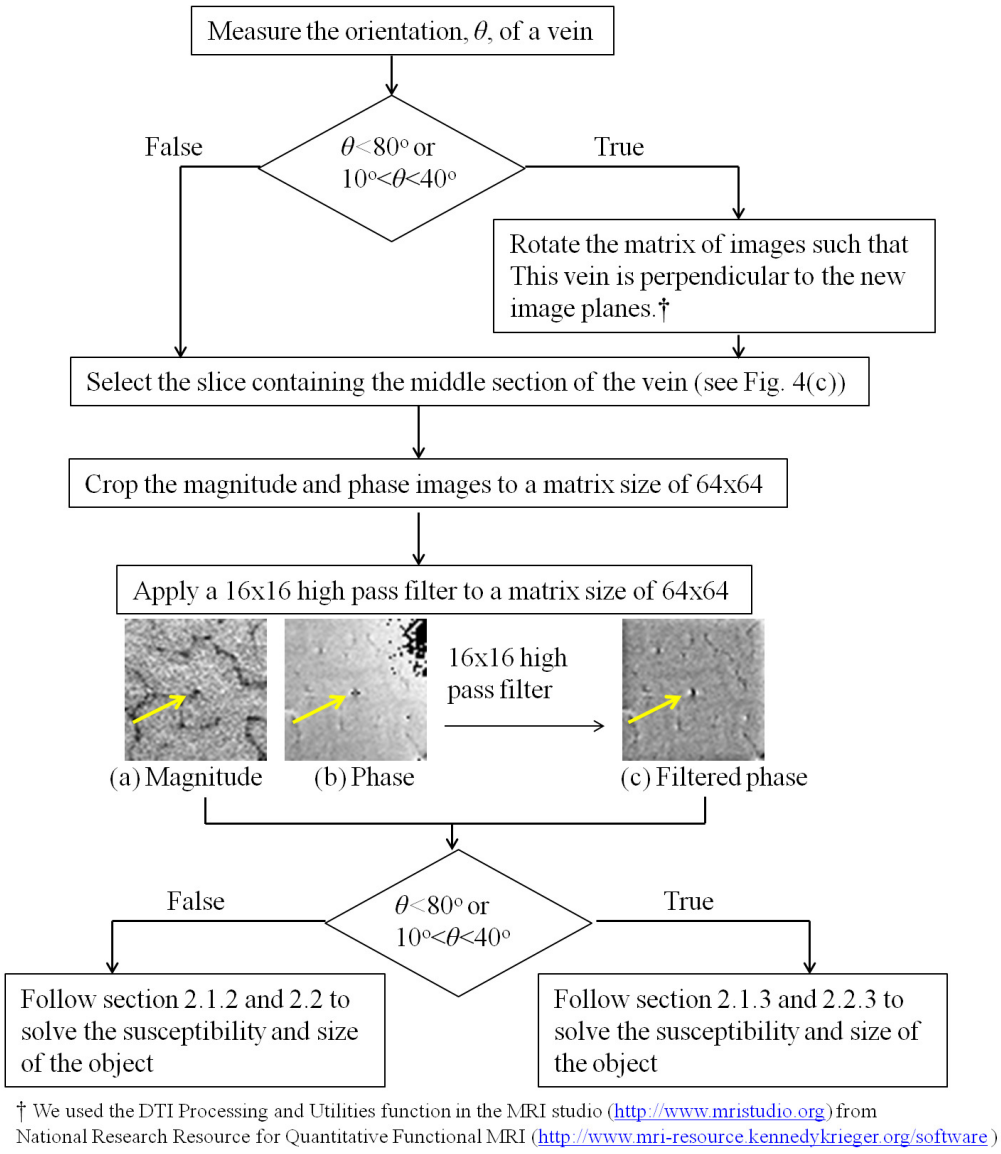

Figure 5.5: The flow chart of *in-vivo* MR data post-processing procedures. The vein is pointed by the yellow arrows at the center of (a), (b), and (c). The signals of this vein and of the surrounding area in magnitude (a) and filtered phase images (c) have been used for extracting the susceptibility and the cross-sectional area of the vein.

Chapter 6

APPLICATION AND FUTURE DIRECTIONS

This series of work has shown accurate results in the susceptibility quantifications of small objects such as veins, air bubbles, and glass beads. The CISSCO method has now also been applied to cerebral microbleeds, calcified spots in the brain, and nanoparticles. The latter can be used as therapeutic agents for treatments or cell labeling at the molecular level [58]. Currently, nanoparticles are quantified by the typical R_2 and $R_2^\star$ method [59], but the lack of MR signals leads to inaccurate results. The CISSCO method avoids low MR signals of objects themselves, as it first obtains the magnetic moment of each object based on field distributions around the object. When the 3D CISSCO method is applied to localized clusters of nanoparticles which label cells in rat brains [60], the number of labeled cells in each cluster can be calculated from CISSCO and other known information such as the neural progenitor cellular iron uptake [61]. This ability of measuring the number of cells opens the door for evaluating drug efficacies in the $in\ vivo$ settings.

While the CISSCO method is developed with the assumptions that objects are spheres or long cylinders, the method can be applied to objects that are not perfect spheres or long cylinders. This is because the far field induced from an object can be always modeled from a sphere with an equivalent magnetic moment. This basic physics concept allows us to apply CISSCO to many $in\ vivo$ objects. However, for accurate susceptibility quantifications of *in vivo* objects, we must first establish standards from phantom studies. As the magnetic susceptibility of a solution is proportional to its concentration, we have seen some very accurate results from CISSCO applied to phantoms consisting of gadolinium, ferritin, and nanoparticle solutions [62]. In general, the uncertainties from these phantom

studies are less than 10%.

Although a quantified magnetic moment from the 2D CISSCO method will not be affected by a constant but unknown background phase around the object, this is not true for the 3D CISSCO method. Thus, the 3D CISSCO method requires further improvement before it is applied to $in\ vivo$ objects [60].

Related to susceptibility quantifications from MR images, it is also important to properly remove the background phase. Currently the most effective background removal method is SHARP [28], but SHARP can still leave some background phase in the surroundings of an object. Some efforts have been made recently [63] but more work toward this direction is needed. Only with a proper background phase removal method, QSM methods can really be applied to clinical domain and served as a diagnostic tool for health conditions such as Alzheimers disease, vascular dementia, traumatic brain injuries, etc..

Appendix A

MAXIMIZING THE REAL SIGNAL FROM AN ANNULAR RING TO IDENTIFY THE OBJECT CENTER

We first define $\beta \equiv \rho^2 = (\rho\cos\psi - x_0)^2 + (\rho\sin\psi - y_0)^2$ and $\alpha \equiv (\rho\cos\psi - x_0)^2 - (\rho\sin\psi - y_0)^2$ such that

$$\cos 2\psi = \frac{(\rho\cos\psi - x_0)^2 - (\rho\sin\psi - y_0)^2}{\rho^2} \equiv \frac{\alpha}{\beta} \tag{A.1}$$

We also define

$$f \equiv e^{-ip\cos 2\psi/\rho^2} = e^{-ip\alpha/\beta^2} \tag{A.2}$$

such that the MR signal S is

$$S = \ell\rho_0 \int_{R_1}^{R_2} d\rho\,\rho \int_0^{2\pi} d\psi f \tag{A.3}$$

The first derivatives of f with respect to x_0 and y_0 are

$$\frac{\partial f}{\partial x_0} = -ipf\frac{2}{\beta^3}(x_0 - \rho\cos\psi)[3(\rho\sin\psi - y_0)^2 - (\rho\cos\psi - x_0)^2] \tag{A.4}$$

$$\frac{\partial f}{\partial y_0} = ipf\frac{2}{\beta^3}(y_0 - \rho\sin\psi)[3(\rho\cos\psi x_0)^2 - (\rho\sin\psi y_0)^2] \tag{A.5}$$

The second derivatives of f with respect to x_0 and y_0 at $x_0 = y_0 = 0$ are

$$\left.\frac{\partial^2 f}{\partial x_0^2}\right|_{x_0=y_0=0} = -2p^2 f\frac{1}{\rho^6}(1 + \cos 6\psi) - 6ipf\frac{1}{\rho^4}\cos 4\psi \tag{A.6}$$

$$\left.\frac{\partial^2 f}{\partial y_0^2}\right|_{x_0=y_0=0} = -2p^2 f\frac{1}{\rho^6}(1 - \cos 6\psi) + 6ipf\frac{1}{\rho^4}\cos 4\psi \tag{A.7}$$

As

$$\int_0^{2\pi} d\psi f = 2\pi J_0(p/\rho^2) \tag{A.8}$$

$$\int_0^{2\pi} d\psi f \cdot \cos 4\psi = -2\pi J_2(p/\rho^2) \tag{A.9}$$

$$\int_0^{2\pi} d\psi f \cdot \cos 6\psi = 2\pi i J_3(p/\rho^2) \tag{A.10}$$

it becomes clear that

$$Im \left.\frac{\partial^2 S}{\partial x_0^2}\right|_{x_0=y_0=0} = -Im \left.\frac{\partial^2 S}{\partial y_0^2}\right|_{x_0=y_0=0} \tag{A.11}$$

and

$$Re \left.\frac{\partial^2 S}{\partial x_0^2}\right|_{x_0=y_0=0} = Re \left.\frac{\partial^2 S}{\partial y_0^2}\right|_{x_0=y_0=0} = 2\pi\ell\rho_0 \left(\frac{p}{R_2^2} J_1\left(\frac{p}{R_2^2}\right) - \frac{p}{R_1^2} J_1\left(\frac{p}{R_1^2}\right)\right) \tag{A.12}$$

As $R_2 > R_1$ and the maximum of $xJ_1(x)$ occurs at $x \approx 2.4$, the first root of $J_0(x)$, proper choices of R_1 and R_2 can lead to a negative value of Eq. A.12. Therefore, the object center can be identified by maximizing the real part of the signal from an annular ring.

Appendix B

MINIMIZING THE REAL SIGNAL OF A CIRCLE TO IDENTIFY THE OBJECT CENTER

The calculations used in this Section require the results derived in the Appendix D and Eq. 2.9. At $x_0 = y_0 = 0$, $r(\psi) = a$ and the relevant MR signal is

$$S = \ell\rho_0 \int_0^{2\pi} d\psi \int_a^R d\rho\, \rho\, f \tag{B.1}$$

which is identical to Eq. A.3 if the upper and lower limits of the ρ integral are properly replaced.

The second derivatives of Eq. 2.7 are the results derived from Appendix D with proper changes of the integral limits, plus the following term:

$$\left.\frac{\partial^2 S}{\partial x_0^2}\right|_{extra} = \frac{\partial}{\partial x_0}\left(\left.\frac{\partial S}{\partial x_0}\right|_{extra}\right) - \ell\rho_0 \int_0^{2\pi} d\psi\, r(\psi) \frac{\partial r(\psi)}{\partial x_0} \left.\frac{\partial f}{\partial x_0}\right|_{\rho=r(\psi)} \tag{B.2}$$

where

$$\left.\frac{\partial S}{\partial x_0}\right|_{extra} = -\ell\rho_0 \int_0^{2\pi} d\psi\, r(\psi) \left.\frac{\partial r(\psi)}{\partial x_0} f\right|_{\rho=r(\psi)} \tag{B.3}$$

The second derivative with respect to y_0 has the identical format with x_0 replaced by y_0.

After tedious derivations, we obtain

$$Im \left.\frac{\partial^2 S}{\partial x_0^2}\right|_{x_0=y_0=0} = -Im \left.\frac{\partial^2 S}{\partial y_0^2}\right|_{x_0=y_0=0} \tag{B.4}$$

and

$$Re \left.\frac{\partial^2 S}{\partial x_0^2}\right|_{x_0=y_0=0} = Re \left.\frac{\partial^2 S}{\partial y_0^2}\right|_{x_0=y_0=0} = 2\pi\ell\rho_0 \left(\frac{p}{R^2}\right) J_1\left(\frac{p}{R^2}\right) > 0 \tag{B.5}$$

when $0 < |p/R^2| < 3.8$, the second root of $J_1(x)$. That the result of Eq. J.2 only depends on R rather than both R and a indicates that this procedure of finding the object center is still valid even if the center of the circle R is outside the object. From a different point of view, when an object (such as a nanoparticle) is very small, one can identify the center

of the object by replacing the small object by a much larger object but with the identical magnetic moment p. This is because when the value of $|g|$ is larger than roughly 5, one cannot unambiguously determine the volume of the object based on the gradient echo signal (see Fig. 2.4a).

Appendix C

ACCURACY OF THE OBJECT CENTER

Even though the center of the object can be determined by the method described in the Appendix E, the center cannot be accurately located due to the presence of noise in images. Consider the Taylor expansion of the MR signal

$$S(x_0, y_0) = S|_{x_0=y_0=0} + \frac{1}{2}x_0^2 \left.\frac{\partial^2 S}{\partial x_0^2}\right|_{x_0=y_0=0} + \frac{1}{2}y_0^2 \left.\frac{\partial^2 S}{\partial y_0^2}\right|_{x_0=y_0=0} + (\text{higher order terms}) \quad \text{(C.1)}$$

where the first order terms vanish, as described in the main text. The center of the object cannot be accurately determined if the sum of the second order terms is less than the noise term and even if the higher order terms are neglected. Using the result of Eq. J.2 and considering only the thermal noise, $\sigma\ell\sqrt{\Delta x \Delta y \pi R^2}$, the following criterion can be established

$$\frac{x_0^2 + y_0^2}{\Delta x \Delta y} \leq \frac{\sqrt{\frac{\pi R^2}{\Delta x \Delta y}}}{\pi \mathrm{SNR}\left(\frac{p}{R^2}\right) J_1\left(\frac{p}{R^2}\right)} = \frac{\sqrt{\frac{p}{\Delta x \Delta y}}}{\sqrt{\pi}\mathrm{SNR}\left(\frac{p}{R^2}\right)^{3/2} J_1\left(\frac{p}{R^2}\right)} \quad \text{(C.2)}$$

The maximum of $x^{1.5}J_1(x)$ occurs at $x \approx 2.6$ and the maximum is roughly 2. At $x = 1.5$ and 2, $x^{1.5}J_1(x) = 1.02$ and 1.63, respectively. With a given magnetic moment p in an image, Eq. C.2 clearly defines how accurate the center can be determined.

Appendix D

MAXIMIZING THE REAL PART OF THE SIGNAL FROM A SPHERICAL SHELL TO IDENTIFY THE OBJECT CENTER

In order to calculate the derivatives of signal S in Eq. 3.3, we first calculate the derivatives of its integrand. We define

$$f \equiv e^{-ip(3\cos^2\theta-1)/d^3} \tag{D.1}$$

and we obtain

$$\begin{aligned}
\frac{\partial f}{\partial x_0} &= -\frac{3ipf}{d^7}[4(r\cos\theta - z_0)^2 - (r\sin\theta\cos\phi - x_0)^2 - (r\sin\theta\sin\phi - y_0)^2](r\sin\theta\cos\phi - x_0) \\
\frac{\partial f}{\partial y_0} &= -\frac{3ipf}{d^7}[4(r\cos\theta - z_0)^2 - (r\sin\theta\cos\phi - x_0)^2 - (r\sin\theta\sin\phi - y_0)^2](r\sin\theta\sin\phi - y_0) \\
\frac{\partial f}{\partial z_0} &= -\frac{3ipf}{d^7}[3(r\sin\theta\cos\phi - x_0)^2 + 3(r\sin\theta\sin\phi - y_0)^2 - 2(r\cos\theta - z_0)^2](z_0 - r\cos\theta)
\end{aligned} \tag{D.2}$$

We can easily find that the first derivatives and the cross terms of the second derivatives of S are all zero at $r_0 = 0$. The remaining second derivatives at $r_0 = 0$ are

$$\begin{aligned}
\left.\frac{\partial^2 S}{\partial x_0^2}\right|_{r_0=0} &= -6\pi p\rho_0\left[3p\int_{R_2}^{R_1}\frac{dr}{r^6}\int_0^1 dx(5x^2-1)^2(1-x^2)f_0 - i\int_{R_2}^{R_1}\frac{dr}{r^3}\int_0^1 dx(35x^4-30x^2+3)f_0\right] \\
\left.\frac{\partial^2 S}{\partial y_0^2}\right|_{r_0=0} &= \left.\frac{\partial^2 S}{\partial x_0^2}\right|_{r_0=0} \\
\left.\frac{\partial^2 S}{\partial z_0^2}\right|_{r_0=0} &= -12\pi p\rho_0\left[3p\int_{R_2}^{R_1}\frac{dr}{r^6}\int_0^1 dx(3-5x^2)^2x^2 f_0 + i\int_{R_2}^{R_1}\frac{dr}{r^3}\int_0^1 dx(35x^4-30x^2+3)f_0\right]
\end{aligned} \tag{D.3}$$

where $f_0 \equiv e^{-ip(3x^2-1)/r^3}$. By changing the variable r to ϕ and defining $\phi \equiv p/r^3$, $\phi_1 \equiv p/R_1^3$, and $\phi_2 \equiv p/R_2^3$, we can rewrite the above equations to

$$\left.\frac{\partial^2 S}{\partial x_0^2}\right|_{r_0=0} = -2\pi p^{1/3}\rho_0\left[3\int_{\phi_1}^{\phi_2}\phi^{2/3}d\phi\int_0^1 dx(5x^2-1)^2(1-x^2)f_\phi - i\int_{\phi_1}^{\phi_2}\frac{d\phi}{\phi^{1/3}}\int_0^1 dx(35x^4-30x^2+3)f_\phi\right]$$

$$\left.\frac{\partial^2 S}{\partial z_0^2}\right|_{r_0=0} = -4\pi p^{1/3}\rho_0 \left[3\int_{\phi_1}^{\phi_2} \phi^{2/3} d\phi \int_0^1 dx(3-5x^2)^2 x^2 f_\phi + i\int_{\phi_1}^{\phi_2} \frac{d\phi}{\phi^{1/3}} \int_0^1 dx(35x^4 - 30x^2 + 3) f_\phi\right] \quad \text{(D.4)}$$

where $f_\phi \equiv \exp\{-i\phi(3x^2-1)\}$. Only the real part of the above equations are invariant when p is changed to $-p$. Thus, we only use the real part to identify the object center.

Appendix E

MINIMIZING THE REAL PART OF THE SIGNAL WITHIN A SPHERE TO IDENTIFY THE OBJECT CENTER

Following the derivation in the above Appendix D, the following first derivative is the extra term that we need to include here in addition to Eq. D.2

$$\left.\frac{\partial S}{\partial w}\right|_{extra} = -\rho_0 \int_0^{2\pi} d\phi \int_0^{\pi} d\theta \, \sin\theta \rho^2 f \Big|_{r=\rho(\theta,\phi)} \frac{\partial \rho}{\partial w} \tag{E.1}$$

where w is either x_0, y_0, or z_0. At $r_0 = 0$, one can show that the first derivatives and cross terms of the second derivatives are all zero. The remaining second derivatives of Eq. 3.4 are the following terms plus the results from Eq. D.3

$$\begin{aligned}
\left.\frac{\partial^2 S}{\partial x_0^2}\right|_{extra,r_0=0} &= 2\pi\rho_0 a \int_0^1 dx\,(3x^2-1) f_a + 6i\pi\rho_0 \frac{p}{a^2} \int_0^1 dx\,(7x^2-1)(1-x^2) f_a \\
\left.\frac{\partial^2 S}{\partial y_0^2}\right|_{extra,r_0=0} &= \left.\frac{\partial^2 S}{\partial x_0^2}\right|_{extra,r_0=0} \\
\left.\frac{\partial^2 S}{\partial z_0^2}\right|_{extra,r_0=0} &= -4\pi\rho_0 a \int_0^1 dx\,(3x^2-1) f_a - 12i\pi\rho_0 \frac{p}{a^2} \int_0^1 dx\,(5-7x^2) x^2 f_a
\end{aligned} \tag{E.2}$$

where $f_a \equiv \exp\{-i\phi_a(3x^2-1)\}$ and $\phi_a \equiv p/a^3$. By defining $\phi_R \equiv p/R^3$, the final formulas of the second derivatives are

$$\begin{aligned}
\left.\frac{\partial^2 S}{\partial x_0^2}\right|_{r_0=0} &= 2\pi\rho_0 a \left[\int_0^1 dx\,(3x^2-1) f_a - 3\phi_a^{1/3} \int_{\phi_R}^{\phi_a} \phi^{2/3} d\phi \int_0^1 dx (5x^2-1)^2 (1-x^2) f_\phi \right. \\
&\quad \left. + 3i\phi_a \int_0^1 dx\,(7x^2-1)(1-x^2) f_a + i\phi_a^{1/3} \int_{\phi_R}^{\phi_a} \frac{d\phi}{\phi^{1/3}} \int_0^1 dx (35x^4 - 30x^2 + 3) f_\phi \right] \\
\left.\frac{\partial^2 S}{\partial y_0^2}\right|_{r_0=0} &= \left.\frac{\partial^2 S}{\partial x_0^2}\right|_{r_0=0} \\
\left.\frac{\partial^2 S}{\partial z_0^2}\right|_{r_0=0} &= -4\pi\rho_0 a \left[\int_0^1 dx\,(3x^2-1) f_a + 3\phi_a^{1/3} \int_{\phi_R}^{\phi_a} \phi^{2/3} d\phi \int_0^1 dx (3-5x^2)^2 x^2 f_\phi \right. \\
&\quad \left. + 3i\phi_a \int_0^1 dx\,(5-7x^2) x^2 f_a + i\phi_a^{1/3} \int_{\phi_R}^{\phi_a} \frac{d\phi}{\phi^{1/3}} \int_0^1 dx (35x^4 - 30x^2 + 3) f_\phi \right]
\end{aligned} \tag{E.3}$$

Again, as only the real part of the above equations are invariant when p is changed to $-p$, we only use the real part to identify the object center.

Appendix F

UNCERTAINTY OF SUSCEPTIBILITY AT A GENERIC ORIENTATION: MAGNETIC MOMENT AND SUSCEPTIBILITY ARE QUANTIFIED FROM THE SAME IMAGE

In the evaluations of the following equations in this Appendix, positive magnetic moment value $|\wp|$ and positive susceptibility $|\Delta\chi|$ should be used.

When the susceptibility is quantified from S_3, which is enclosed by a radius R_3, the uncertainty of the susceptibility is given by

$$\frac{\delta\Delta\chi}{\Delta\chi} = \frac{\sqrt{\delta\theta^2 A^2 + (\frac{\delta Re(S_3)}{\pi\ell\sigma})^2 B^2 + (\frac{\delta Im(S_3)}{\pi\ell\sigma})^2 C^2 + (\frac{\delta(S_1-S_2)}{\pi\ell\sigma})^2 D^2 + (\frac{\delta(S_2-S_3)}{\pi\ell\sigma})^2 E^2}}{|\wp/\sin\theta^2|\,|\mathsf{SNR}_{0,c}(1-3\cos^2\theta)/3 - \mathsf{SNR}_0 \sin\phi_{in} J_0(g')/g|} \tag{F.1}$$

where $\mathsf{SNR}_0 \equiv \rho_0/\sigma$ and $\mathsf{SNR}_{0,c} \equiv \rho_{0,c}/\sigma$

$$A = 2|\wp|\frac{\cos\theta}{\sin\theta}\left(\mathsf{SNR}_0 \sin\phi_{in}\frac{J_0(g')}{g'} - \mathsf{SNR}_{0,c}\right) \tag{F.2}$$

$$B = -\sin\phi_{in}$$

$$C = \cos\phi_{in}$$

$$D = \sin\phi_{in}\left(\frac{h_3}{h_{12}} + \frac{h_{23}\left(\frac{h_3}{h_{12}}(\frac{J_0(\phi_2)}{\phi_2} - \frac{J_0(\phi_1)}{\phi_1}) + \frac{J_0(\phi_3)}{\phi_3}\right)}{h_{12}\frac{J_0(\phi_3)}{\phi_3} + h_{23}\frac{J_0(\phi_1)}{\phi_1} + h_{31}\frac{J_0(\phi_2)}{\phi_2}}\right)$$

$$E = -\sin\phi_{in}\frac{\left(h_3(\frac{J_0(\phi_2)}{\phi_2} - \frac{J_0(\phi_1)}{\phi_1}) + h_{12}\frac{J_0(\phi_3)}{\phi_3}\right)}{h_{12}\frac{J_0(\phi_3)}{\phi_3} + h_{23}\frac{J_0(\phi_1)}{\phi_1} + h_{31}\frac{J_0(\phi_2)}{\phi_2}}$$

where $h_3 = \int_{\phi_3}^{|g'|} \frac{dx}{x^2} J_0(x)$, and $\phi_i \equiv |\wp|/R_i^2$, $i = 1, 2$ or 3

$$h_{ij} = \int_{\phi_i}^{\phi_j} \frac{dx}{x^2} J_0(x)$$

$$\frac{\delta Re(S_3)}{\pi \ell \sigma} = \sqrt{\frac{\Delta x \Delta y R_3^2}{\pi} + \epsilon_R^2 (\wp h_3 \mathsf{SNR}_0 + \mathsf{SNR}_{0,c} \cos\phi_{in} \frac{\wp}{|g'|})^2}$$

where ϵ_R is defined as the percentage change between the theoretical value of $Re(S_3)$ and summed $Re(S_3)$ directly from images.

$$\frac{\delta Im(S_3)}{\pi \ell \sigma} = \sqrt{\frac{\Delta x \Delta y R_3^2}{\pi} + \epsilon_I^2 (\mathsf{SNR}_{0,c} \sin\phi_{in} \frac{\wp}{|g'|})^2}$$

where ϵ_I is defined as the percentage change between the theoretical value of $Im(S_3)$ and summed $Im(S_3)$ directly from images.

$$\frac{\delta(S_i - S_j)}{\pi \ell \sigma} = \sqrt{\frac{\Delta x \Delta y}{\pi} \left| R_i^2 - R_j^2 \right| + \epsilon_{ij}^2 (\wp h_{ij} \mathsf{SNR}_0)^2}$$

where $\epsilon_{ij} \equiv \delta(S_i - S_j)/(S_i - S_j)$ for $i,\ j = 1, 2, 3$ and the index i or j refers to the circle within which the complex signal is added. Similarly, ϵ_{ij} should be interpreted as the percentage change between the theoretical $S_i - S_j$ (which is a real number) and the real part of summed $S_i - S_j$ directly from images.

The uncertainty of the spin density outside the object is calculated from $S_1 - S_2$ and is given by

$$\frac{\delta \rho_0}{\rho_0} = \frac{1}{\mathsf{SNR}_0} \sqrt{(\frac{F}{\wp})^2 (\frac{\delta(S_1 - S_2)}{\pi \ell \sigma})^2 + (\frac{G}{\wp})^2 (\frac{\delta(S_3 - S_2)}{\pi \ell \sigma})^2}$$

where

$$\frac{F}{\wp} = \frac{1}{\wp h_{12}} + \frac{\frac{h_{23}}{h_{12}} \left(h_{12} + \frac{J_0(\phi_2)}{\phi_2} - \frac{J_0(\phi_1)}{\phi_1} \right)}{\wp \left(h_{12} \frac{J_0(\phi_3)}{\phi_3} + h_{23} \frac{J_0(\phi_1)}{\phi_1} + h_{31} \frac{J_0(\phi_2)}{\phi_2} \right)}$$

$$\frac{G}{\wp} = \frac{-\left(h_{12} + \frac{J_0(\phi_2)}{\phi_2} - \frac{J_0(\phi_1)}{\phi_1} \right)}{\wp \left(h_{12} \frac{J_0(\phi_3)}{\phi_3} + h_{23} \frac{J_0(\phi_1)}{\phi_1} + h_{31} \frac{J_0(\phi_2)}{\phi_2} \right)}$$

The cross-sectional area of a cylindrical object is defined as $A_0 \equiv \pi a^2$. Its uncertainty is given by

$$\frac{\delta A_0}{A_0} = \Bigg[(\frac{A}{H} + 2\cot\theta)^2 \delta\theta^2 + (\frac{B}{H})^2 (\frac{\delta Re(S_3)}{\pi \ell \sigma})^2 + (\frac{C}{H})^2 (\frac{\delta Im(S_3)}{\pi \ell \sigma})^2 + (\frac{h_{23}}{I} + \frac{D}{H})^2 (\frac{\delta(S_1 - S_2)}{\pi \ell \sigma})^2 + (\frac{h_{12}}{I} - \frac{E}{H})^2 (\frac{\delta(S_2 - S_3)}{\pi \ell \sigma})^2 \Bigg]^{1/2}$$

where

$$H = \left| \wp / \sin\theta^2 \right| \left(\mathsf{SNR}_{0,c} (1 - 3\cos^2\theta)/3 - \mathsf{SNR}_0 \sin\phi_{in} J_0(g')/g \right)$$

$$I = \wp \mathsf{SNR}_0 \left(h_{12} \frac{J_0(\phi_3)}{\phi_3} + h_{23} \frac{J_0(\phi_1)}{\phi_1} + h_{31} \frac{J_0(\phi_2)}{\phi_2} \right)$$

The spin density inside the object is given by

$$\frac{\delta \rho_{0,c}}{\rho_{0,c}} = \Bigg[\left(\frac{\delta Im(S_3)}{\pi \ell \sigma} \right)^2 \left(\frac{1}{a^2 \sin\phi_{in} \mathsf{SNR}_{0,c}} + \frac{C}{H} (1 - \phi_{in} \cot\phi_{in}) \right)^2 + \left(\frac{\delta Re(S_3)}{\pi \ell \sigma} \right)^2 \left(\frac{B}{H} (1 - \phi_{in} \cot\phi_{in}) \right)^2 + \left(\frac{\delta(S_1 - S_2)}{\pi \ell \sigma} \right)^2 J^2 + \left(\frac{\delta(S_2 - S_3)}{\pi \ell \sigma} \right)^2 K^2 + (\delta\theta)^2 \left(\frac{A}{H} (1 - \phi_{in} \cot\phi_{in}) - g \sin 2\theta \cot\phi_{in} + 2\cot\theta \right)^2 \Bigg]^{1/2}$$

where

$$J = \frac{D}{H} (1 - \phi_{in} \cot\phi_{in}) + \frac{h_{23}}{I}$$

$$K = \frac{E}{H} (1 - \phi_{in} \cot\phi_{in}) - \frac{h_{12}}{I}$$

Appendix G

UNCERTAINTY OF SUSCEPTIBILITY FOR THE PARALLEL ORIENTATION

In this Appendix, subscripts 1 and 2 in the following equations refer to the values quantified from echo time T_{E_1} and T_{E_2}, respectively. They should not be confused with different radii used in the main text and the previous Appendix.

The uncertainty of the susceptibility is given by

$$\begin{aligned}\frac{\delta\Delta\chi}{\Delta\chi} &= \left[\delta\theta^2(\frac{\mathbb{A}}{\mathbb{H}})^2 + (\frac{\mathbb{B}}{\mathbb{H}})^2\left(\frac{\delta\rho_{0,1}}{\rho_{0,1}}\right)^2 + (\frac{\mathbb{C}}{\mathbb{H}})^2\left(\frac{\delta\rho_{0,2}}{\rho_{0,2}}\right)^2 + (\frac{\mathbb{D}}{\mathbb{H}})^2\left(\frac{\delta Re(S_1)}{\ell\rho_{0,1}}\right)^2\right. \\ &+ \left.(\frac{\mathbb{E}}{\mathbb{H}})^2\left(\frac{\delta Re(S_2)}{\ell\rho_{0,2}}\right)^2 + (\frac{\mathbb{F}}{\mathbb{H}})^2\left(\frac{\delta Im(S_1)}{\ell\rho_{0,1}}\right)^2 + (\frac{\mathbb{G}}{\mathbb{H}})^2\left(\frac{\delta Im(S_2)}{\ell\rho_{0,2}}\right)^2\right]^{1/2}\end{aligned} \tag{G.1}$$

$$\mathbb{A} = -\mathbb{I}\sin 2\theta$$

$$\mathbb{B} = \tan\phi_{in,1}\left(\frac{Im(S_2)}{\ell\rho_{0,2}} - \frac{Re(S_2)}{\ell\rho_{0,2}}\tan\phi_{in,2}\right)$$

$$\mathbb{C} = \tan\phi_{in,2}\left(\frac{Re(S_1)}{\ell\rho_{0,1}}\tan\phi_{in,1} - \frac{Im(S_1)}{\ell\rho_{0,1}}\right)$$

$$\mathbb{D} = \tan\phi_{in,1}\tan\phi_{in,2}$$

$$\mathbb{E} = -\mathbb{D}$$

$$\mathbb{F} = -\tan\phi_{in,2}$$

$$\mathbb{G} = \tan\phi_{in,1}$$

$$\mathbb{H} = \frac{1}{3}(1 - 3\cos^2\theta)\mathbb{I}$$

$$\begin{aligned}\mathbb{I} &= \left(\frac{Re(S_1)}{\ell\rho_{0,1}} - \frac{Re(S_2)}{\ell\rho_{0,2}}\right)(g_1 \cdot \tan\phi_{in,2} + g_2 \cdot \tan\phi_{in,1}) \\ &+ \frac{Im(S_1)}{\ell\rho_{0,1}}(g_1 \tan\phi_{in,1}\tan\phi_{in,2} - g_2) - \frac{Im(S_2)}{\ell\rho_{0,2}}(g_2 \tan\phi_{in,1}\tan\phi_{in,2} - g_1)\end{aligned}$$

$$\frac{\delta Re(S_n)}{\ell\rho_{0,n}} = \sqrt{\Delta x\Delta y\frac{\pi R^2}{\mathrm{SNR}_{0,n}^2} + \epsilon_R^2\left(\frac{Re(S_n)}{\ell\rho_{0,n}}\right)^2} \tag{G.2}$$

$$\frac{\delta Im(S_n)}{\ell\rho_{0,n}} = \sqrt{\Delta x\Delta y\frac{\pi R^2}{\mathrm{SNR}_{0,n}^2} + \epsilon_I^2\left(\frac{Im(S_n)}{\ell\rho_{0,n}}\right)^2} \tag{G.3}$$

$$\frac{\delta\rho_{0,n}}{\rho_{0,n}} = \sqrt{\frac{\Delta x\Delta y}{\pi(R_a^2 - R_b^2)\mathrm{SNR}_{0,n}^2} + \epsilon_{ab}^2}$$

where ϵ_{ab} is the percentage error between the theoretical spin density and the measured spin density within the annular ring defined by radii R_a and R_b.

The uncertainty of the cross-sectional area quantified from each echo time is given by

$$\begin{aligned}\left(\frac{\delta A_0}{A_0}\right)_{\mathrm{T_{E1}}} &= \Bigg[\left(\frac{\delta Im(S_1)}{\ell\rho_{0,1}}\right)^2\left(\frac{\mathbb{KF}}{\mathbb{JH}} + \frac{\cot\phi_{in,1}}{\mathbb{J}}\right)^2 + \left(\frac{\delta Im(S_2)}{\ell\rho_{0,2}}\right)^2\left(\frac{\mathbb{KG}}{\mathbb{JH}}\right)^2 \\ &+ \left(\frac{\delta Re(S_1)}{\ell\rho_{0,1}}\right)^2\left(\frac{\mathbb{KD}}{\mathbb{JH}} - \frac{1}{\mathbb{J}}\right)^2 + \left(\frac{\delta Re(S_2)}{\ell\rho_{0,2}}\right)^2\left(\frac{\mathbb{KE}}{\mathbb{JH}}\right)^2 + \left(\frac{\delta\rho_{0,1}}{\rho_{0,1}}\right)^2\left(\frac{\mathbb{KB}}{\mathbb{JH}} + \frac{\mathbb{M}}{\mathbb{J}}\right)^2 \\ &+ \left(\frac{\delta\rho_{0,2}}{\rho_{0,2}}\right)^2\left(\frac{\mathbb{KC}}{\mathbb{JH}}\right)^2 + \delta\theta^2\left(\frac{\mathbb{KA}}{\mathbb{JH}} + \frac{\mathbb{L}}{\mathbb{J}}\right)^2\Bigg]^{1/2}\end{aligned} \tag{G.4}$$

and

$$\begin{aligned}\left(\frac{\delta A_0}{A_0}\right)_{\mathrm{TE2}} &= \left[\left(\frac{\delta Im(S_1)}{\ell\rho_{0,1}}\right)^2\left(\frac{\mathbb{KF}}{\mathbb{JH}}\right)^2+\left(\frac{\delta Im(S_2)}{\ell\rho_{0,2}}\right)^2\left(\frac{\mathbb{KG}}{\mathbb{JH}}+\frac{\cot\phi_{in,2}}{\mathbb{J}}\right)^2\right. \\ &+ \left(\frac{\delta Re(S_1)}{\ell\rho_{0,1}}\right)^2\left(\frac{\mathbb{KD}}{\mathbb{JH}}\right)^2+\left(\frac{\delta Re(S_2)}{\ell\rho_{0,2}}\right)^2\left(\frac{\mathbb{KE}}{\mathbb{JH}}-\frac{1}{\mathbb{J}}\right)^2+\left(\frac{\delta\rho_{0,1}}{\rho_{0,1}}\right)^2\left(\frac{\mathbb{KB}}{\mathbb{JH}}\right)^2 \\ &+ \left.\left(\frac{\delta\rho_{0,2}}{\rho_{0,2}}\right)^2\left(\frac{\mathbb{KC}}{\mathbb{JH}}+\frac{\mathbb{M}}{\mathbb{J}}\right)^2+\delta\theta^2\left(\frac{\mathbb{KA}}{\mathbb{JH}}+\frac{\mathbb{L}}{\mathbb{J}}\right)^2\right]^{1/2}\end{aligned} \tag{G.5}$$

where the subscript n used in the following definitions refers to each variable obtained at the n^{th} echo time T_{E_n}, as those variables depend on the echo time.

$$\mathbb{J}=A_0\left(1+\frac{g_n'^2}{4}-\frac{g_n'^2a^2}{2R^2}\right)$$

$$\mathbb{K}=-\phi_{in,n}\frac{Im(S_n)}{\ell\rho_{0,n}}\csc^2\phi_{in,n}-\pi(R^2-a^2)\frac{g_n'^2a^2}{2R^2}$$

$$\mathbb{L}=-g_n\frac{Im(S_n)}{\ell\rho_{0,n}}\csc^2\phi_{in,n}\sin 2\theta-\pi(R^2-a^2)\frac{g_n'^2a^2}{R^2}\cot\theta$$

$$\mathbb{M}=\pi(R^2-a^2)(1-\frac{g_n'^2a^2}{4R^2})$$

If the cross-sectional area is averaged from two echo times, its uncertainty is given by

$$\begin{aligned}\frac{\delta A_0}{A_0} &= \mathbb{N}^{-1}\left[\left(\frac{\delta Re(S_1)}{\ell\rho_{0,1}}\right)^2\left(1+\frac{\mathbb{D}}{\mathbb{H}}\mathbb{O}\right)^2+\left(\frac{\delta Re(S_2)}{\ell\rho_{0,2}}\right)^2\left(1+\frac{\mathbb{E}}{\mathbb{H}}\mathbb{O}\right)^2\right. \\ &+ \left(\frac{\delta Im(S_2)}{\ell\rho_{0,2}}\right)^2\left(\cot\phi_{in,2}-\frac{\mathbb{G}}{\mathbb{H}}\mathbb{O}\right)^2+\left(\frac{\delta Im(S_1)}{\ell\rho_{0,1}}\right)^2\left(\cot\phi_{in,1}-\frac{\mathbb{F}}{\mathbb{H}}\mathbb{O}\right)^2 \\ &+ \left(\frac{\delta\rho_{0,1}}{\rho_{0,1}}\right)^2\left(\mathbb{C}\cot\phi_{in,1}\cot\phi_{in,2}-\frac{\mathbb{B}}{\mathbb{H}}\mathbb{O}\right)^2 \\ &+ \left.\left(\frac{\delta\rho_{0,2}}{\ell\rho_{0,2}}\right)^2\left(\mathbb{B}\cot\phi_{in,1}\cot\phi_{in,2}+\frac{\mathbb{C}}{\mathbb{H}}\mathbb{O}\right)^2+(\delta\theta)^2\mathbb{P}^2\right]^{1/2}\end{aligned} \tag{G.6}$$

where

$$\mathbb{N} = 2A_0\left(1 + \frac{g_1'^2 + g_2'^2}{8} - \frac{(g_1'^2 + g_2'^2)a^2}{4R^2}\right)$$

$$\mathbb{O} = \frac{Im(S_1)}{\ell\rho_{0,1}}\phi_{in,1}\csc^2\phi_{in,1} + \frac{Im(S_2)}{\ell\rho_{0,2}}\phi_{in,2}\csc^2\phi_{in,2} + \pi(R^2 - a^2)\frac{(g_1'^2 + g_2'^2)a^2}{2R^2}$$

$$\mathbb{P} = \pi(R^2 - a^2)\frac{a^2}{R^2}\left(\frac{2}{1 - 3\cos^2\theta}\right)\left(g_1^2 + g_2^2\right)\sin^3\theta\cos\theta$$

The uncertainty of the spin density inside the object quantified from each echo time is given by

$$\begin{aligned}
\frac{\delta\rho_{0,c,1}}{\rho_{0,c,1}} &= \left[\left(\frac{\delta\rho_{0,1}}{\rho_{0,1}}\right)^2\left(\frac{\mathbb{M}}{\mathbb{J}} + \frac{\mathbb{B}}{\mathbb{H}}\mathbb{Q}\right)^2 + \left(\frac{\delta\rho_{0,2}}{\rho_{0,2}}\right)^2\left(\frac{\mathbb{C}}{\mathbb{H}}\mathbb{Q}\right)^2 + \left(\frac{\delta Re(S_1)}{\ell\rho_{0,1}}\right)^2\left(\frac{1}{\mathbb{J}} - \frac{\mathbb{D}}{\mathbb{H}}\mathbb{Q}\right)^2\right. \\
&+ \left(\frac{\delta Re(S_2)}{\ell\rho_{0,2}}\right)^2\left(\frac{\mathbb{E}}{\mathbb{H}}\mathbb{Q}\right)^2 + \left(\frac{\delta Im(S_1)}{\ell\rho_{0,1}}\right)^2\left(\frac{\ell\rho_{0,1}}{Im(S_1)} - \frac{\mathbb{F}}{\mathbb{H}}\mathbb{Q} - \frac{\cot\phi_{in,1}}{\mathbb{J}}\right)^2 \\
&+ \left.\left(\frac{\delta Im(S_2)}{\ell\rho_{0,2}}\right)^2\left(\frac{\mathbb{G}}{\mathbb{H}}\mathbb{Q}\right)^2 + \delta\theta^2\left(\frac{\mathbb{A}}{\mathbb{H}}\mathbb{Q} + \frac{\mathbb{L}}{\mathbb{J}} + g_1\cot\phi_{in,1}\sin 2\theta\right)^2\right]^{1/2}
\end{aligned}$$

$$\begin{aligned}
\frac{\delta\rho_{0,c,2}}{\rho_{0,c,2}} &= \left[\left(\frac{\delta\rho_{0,1}}{\rho_{0,1}}\right)^2\left(\frac{\mathbb{B}}{\mathbb{H}}\mathbb{Q}\right)^2 + \left(\frac{\delta\rho_{0,2}}{\rho_{0,2}}\right)^2\left(\frac{\mathbb{M}}{\mathbb{J}} + \frac{\mathbb{C}}{\mathbb{H}}\mathbb{Q}\right)^2 + \left(\frac{\delta Re(S_1)}{\ell\rho_{0,1}}\right)^2\left(\frac{\mathbb{D}}{\mathbb{H}}\mathbb{Q}\right)^2\right. \\
&+ \left(\frac{\delta Re(S_2)}{\ell\rho_{0,2}}\right)^2\left(\frac{1}{\mathbb{J}} - \frac{\mathbb{E}}{\mathbb{H}}\mathbb{Q}\right)^2 + \left(\frac{\delta Im(S_1)}{\ell\rho_{0,1}}\right)^2\left(\frac{\mathbb{F}}{\mathbb{H}}\mathbb{Q}\right)^2 \\
&+ \left.\left(\frac{\delta Im(S_2)}{\ell\rho_{0,2}}\right)^2\left(\frac{\ell\rho_{0,2}}{Im(S_2)} - \frac{\mathbb{G}}{\mathbb{H}}\mathbb{Q} - \frac{\cot\phi_{in,2}}{\mathbb{J}}\right)^2 + \delta\theta^2\left(\frac{\mathbb{A}}{\mathbb{H}}\mathbb{Q} + \frac{\mathbb{L}}{\mathbb{J}} + g_2\cot\phi_{in,2}\sin 2\theta\right)^2\right]^{1/2}
\end{aligned}$$

$$\mathbb{Q} = \frac{\mathbb{K}}{\mathbb{J}} + \phi_{in,n}\cot\phi_{in,n}$$

where the subscript n again refers to each variable measured at the n^{th} echo time T_{E_n}.

If we use Eq.(G.6) to further estimate the uncertainty of spin density inside the object

at each echo time, these two uncertainties are given by

$$\begin{aligned}\frac{\delta\rho_{0,c,n}}{\rho_{0,c,n}} &= \Bigg[\delta\theta^2\mathbb{R}^2 + (\frac{\delta\rho_{0,1}}{\rho_{0,1}})^2(\frac{\mathbb{B}}{\mathbb{H}}\mathbb{S} - \frac{\mathbb{C}}{\mathbb{N}}\mathbb{T})^2 + (\frac{\delta\rho_{0,2}}{\rho_{0,2}})^2(\frac{\mathbb{C}}{\mathbb{H}}\mathbb{S} + \frac{\mathbb{B}}{\mathbb{N}}\mathbb{T})^2 \\ &+ (\frac{\delta Re(S_1)}{\ell\rho_{0,1}})^2(\frac{1}{\mathbb{N}} + \frac{\mathbb{D}}{\mathbb{H}}\mathbb{S})^2 + (\frac{\delta Re(S_2)}{\ell\rho_{0,2}})^2(\frac{1}{\mathbb{N}} + \frac{\mathbb{E}}{\mathbb{H}}\mathbb{S})^2 \\ &+ (\frac{\delta Im(S_1)}{\ell\rho_{0,1}})^2(\frac{\mathbb{F}}{\mathbb{H}}\mathbb{S} + \delta_{n,1}\frac{\ell\rho_{0,1}}{Im(S_1)} - \frac{\cot\phi_{in,1}}{\mathbb{N}})^2 \\ &+ (\frac{\delta Im(S_2)}{\ell\rho_{0,2}})^2(\frac{\mathbb{G}}{\mathbb{H}}\mathbb{S} + \delta_{n,2}\frac{\ell\rho_{0,2}}{Im(S_2)} - \frac{\cot\phi_{in,2}}{\mathbb{N}})^2\Bigg]^{1/2}\end{aligned}$$

where $\delta_{n,1}$ and $\delta_{n,2}$ are Kronecker delta functions. Again, the subscript n refers to each variable measured at the n^{th} echo time T_{E_n}.

$$\mathbb{R} = \frac{\mathbb{P}}{\mathbb{N}} + \cot\phi_{in,n}(\frac{\mathbb{A}}{\mathbb{H}}\phi_{in,n} + g_n\sin 2\theta)$$

$$\mathbb{S} = \frac{\mathbb{O}}{\mathbb{N}} - \phi_{in,n}\cot\phi_{in,n}$$

$$\mathbb{T} = \cot\phi_{in,1}\cot\phi_{in,2}$$

Appendix H

THE UNIQUE SOLUTION OF Eq.(4.7)

In this section, g' will be separated into two regimes, $g' > 1.4$ and $0 < g' < 2$. As $J_0(x)/x^2$ is an even function, Eq.(4.7) is invariant even if the sign of magnetic susceptibility, $\Delta\chi$, is changed. Thus, we only consider the positive magnetic susceptibility in the following discussions. This means that g, g', and $\wp$ are also considered to be positive.

H.1 $g' \geq 1.4$

If $\wp/R^2$ is no more than 0.5 radian, g' can be replaced by infinity in Eq.(4.7). This replacement leads to less than 5% deviation from the original result of the integral. Eq.(4.7) can be rewritten and easily solved.

$$Re(S)\sin\phi_{in} = Im(S)\ \cos\phi_{in} + \pi\ell\rho_0\wp\ \sin\phi_{in}\int_{\wp/R^2}^{\infty} dx J_0(x)/x^2 \tag{H.1}$$

$$\phi_{in} = \tan^{-1}\frac{Im(S)}{Re(S) - \pi\ell\rho_0\wp\int_{\wp/R^2}^{\infty} dx\frac{J_0(x)}{x^2}} + 2n\pi \tag{H.2}$$

where n is any integer. Note that it is $2n\pi$ rather than $n\pi$ in the above solution, as the sign of $Im(S)$ is known in Eq.(H.1).

H.2 $0 < g' < 2$

The phase inside the object ϕ_{in} can be rewritten as $\beta g = \beta g'/\alpha$, with $\alpha \equiv \sin\theta^2$ and $\beta \equiv (1 - 3\cos\theta^2)/3$. Therefore, Eq.(4.7) can be rewritten as the following

$$f(g') \equiv Im(S)\cot(\frac{\beta}{\alpha}g') + \pi\ell\rho_0\wp\int_{\wp/R^2}^{g'}\frac{J_0(x)}{x^2}dx - Re(S) \tag{H.3}$$

The first derivative of $f(g')$ is

$$\begin{aligned} f'(g') &= -\frac{\beta}{\alpha}Im(S)\cdot\csc^2(\frac{\beta}{\alpha}g') + \pi\ell\rho_0\wp\frac{J_0(g')}{g'^2} \\ &= \csc^2(\frac{\beta}{\alpha}g')\left[-\frac{\beta}{\alpha}Im(S) + (\frac{\beta}{\alpha})^2\pi\ell\rho_0\wp J_0(g')\mathsf{sinc}^2\phi_{in}\right] \\ &= \csc^2(\frac{\beta}{\alpha}g')\left[-\frac{\beta}{\alpha}Im(S) + k(\phi_{in})\right] \end{aligned} \tag{H.4}$$

where $k(\phi_{in}) \equiv (\frac{\beta}{\alpha})^2 \pi \ell \rho_0 \wp J_0(g')\text{sinc}^2\phi_{in}$.

Clearly, if $\beta Im(S) < 0$, then $f'(g')$ will always be positive and therefore, by the mean value theorem in calculus, only one root exists in $f(g') = 0$. As $\beta Im(S)$ is proportional to $\beta \sin(\phi_{in}) = \beta \sin(\beta g) = |\beta| \sin(|\beta| g) = |\beta| \sin(|\phi_{in}|)$, when $\beta Im(S) < 0$, this implies that $|\phi_{in}|$ is between $(2n-1)\pi$ and $2n\pi$, with n being any positive integer.

On the other hand, when $\beta Im(S) > 0$, this implies that $|\phi_{in}|$ is between $(2n-2)\pi$ and $(2n-1)\pi$. When $|\phi_{in}| < \pi$, Fig. H.1 indicates at most one solution from $f'(g') = 0$. Again, by the mean value theorem, at most two solutions can exist in $f(g') = 0$.

When $\beta Im(S) > 0$ and $2n\pi < |\phi_{in}| < (2n+1)\pi$ with n being a positive integer, Fig. H.1 or Eq.(H.4) indicates that up to two roots can be solved from $f'(g') = 0$ in each π range. This means that at most three solutions can exist in every π range of $f(g') = 0$. Given $0 < g' = \alpha g < 2$ and $\phi_{in} \equiv \beta g$ in the current discussions, we can further derive that

$$0 < 1 - \cos^2\theta = \alpha < \frac{2}{3(n\pi + 1)} \tag{H.5}$$

and

$$-\frac{2}{3} < \beta < -\frac{2n\pi}{3(n\pi + 1)} \tag{H.6}$$

When $n \geq 1$, α is less than 0.161, β is less than -0.506, and the orientation of the object is less than 24° from the main field.

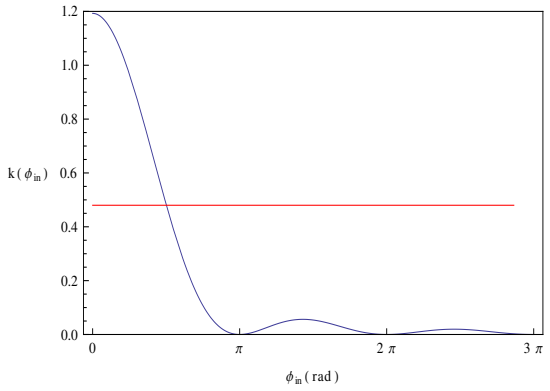

Figure H.1: A plot of $k(\phi_{in}) \equiv \pi\ell\rho_0(\beta/\alpha)^2\wp\text{sinc}^2(\phi_{in})J_0(g')$ versus ϕ_{in}. The plot is generated with $\theta = 90°$, $\alpha/\beta = 0.111$, $\wp = 6.02$, $\rho_0 = 10.0$, $\ell = 1$, $g' = 1.5$, and $Im(S) = 1000$. $k(\phi_{in})$ is defined in Eq.(H.4). This function is monotonically decreased between 0 and π and starts oscillating beyond π. The actual imaginary part of the signal is represented by a horizontal line. The intersection of the horizontal line and the curve indicates the solution of $f'(g')$.

Appendix I

DERIVATION OF Eq.(5.6) FOR THE ESTIMATION OF SUSCEPTIBILITY

We estimate the uncertainty of Eq.(5.5) by deriving the variation of $h(\Delta\chi)$. As the susceptibility has not been solved yet, we do not consider the variation of the susceptibility. We also neglect the uncertainty of ρ_0.

$$\begin{aligned}
&\delta h(\Delta\chi) = \\
&\quad [\delta Re(S)]\sin\phi_{in} - [\delta Im(S)]\cos\phi_{in} - \pi\ell\rho_0(\delta\wp)\sin\phi_{in}\int_{\wp/R^2}^{g'} dx\frac{J_0(x)}{x^2} + \pi\ell\rho_0(\delta\wp)\sin\phi_{in}\frac{J_0(\wp/R^2)}{\wp/R^2} \\
&= \quad \sin\phi_{in}\left[(\pm\sigma\ell\sqrt{\Delta x\Delta y\pi R^2}) - (\pm\sigma\ell\sqrt{\Delta x\Delta y\pi R^2})\cot\phi_{in} + \pi\ell\rho_0(\delta\wp)\left(\frac{J_0(\wp/R^2)}{\wp/R^2} - \int_{\wp/R^2}^{g'} dx\frac{J_0(x)}{x^2}\right)\right]
\end{aligned}$$

Here we only consider the thermal noise in $\delta Re(S)$ and $\delta Im(S)$. As $\delta Re(S)$, $\delta Im(S)$, and $\delta\wp$ are uncorrelated with each other with the proper choices of R_1, R_2, and R_3, the uncertainty of $h(\Delta\chi)$ is

$$\delta h(\Delta\chi)_{max} = \sqrt{(\sigma\ell\sqrt{\Delta x\Delta y\pi R^2})^2 + (\delta\wp)^2\left(\pi\ell\rho_0\sin\phi_{in}\left(\frac{J_0(\wp/R^2)}{\wp/R^2} - \int_{\wp/R^2}^{g'} dx\,\frac{J_0(x)}{x^2}\right)\right)^2}$$

The uncertainty of magnetic moment, $\delta\wp$, is calculated from Eq.15 in [8]. The Gaussian noise, σ, may be measured from the background of magnitude images.

Appendix J

IDENTIFYING THE OBJECT CENTER WITH THE PRESENCE OF A LOCAL UNIFORM FIELD

With an assumed constant local background phase, ϕ_{bkg}, the MR complex signal, S, becomes $Se^{i\phi_{bkg}}$. With Eq.(B.1) from [8], which shows the second derivatives of the original signal S within a radius R,

$$Im\ \frac{\partial^2 S}{\partial x_0^2}\bigg|_{x_0=y_0=0} = -Im\ \frac{\partial^2 S}{\partial y_0^2}\bigg|_{x_0=y_0=0} = -2\pi\ell\rho_0 \left(\frac{\wp}{R^2}\right) J_2\left(\frac{\wp}{R^2}\right) \tag{J.1}$$

and

$$Re\ \frac{\partial^2 S}{\partial x_0^2}\bigg|_{x_0=y_0=0} = Re\ \frac{\partial^2 S}{\partial y_0^2}\bigg|_{x_0=y_0=0} = 2\pi\ell\rho_0 \left(\frac{\wp}{R^2}\right) J_1\left(\frac{\wp}{R^2}\right) \tag{J.2}$$

the real parts of the second derivatives of $Se^{i\phi_{bkg}}$ are

$$Re\frac{\partial^2 Se^{i\phi_{bkg}}}{\partial x_0^2}|_{x_0=y_0=0} = 2\pi\ell\rho_0\frac{\wp}{R^2}\left(J_1(\frac{\wp}{R^2})\cos\phi_{bkg} + J_2(\frac{\wp}{R^2})\sin\phi_{bkg}\right) \tag{J.3}$$

and

$$Re\frac{\partial^2 Se^{i\phi_{bkg}}}{\partial y_0^2}|_{x_0=y_0=0} = 2\pi\ell\rho_0\frac{\wp}{R^2}\left(J_1(\frac{\wp}{R^2})\cos\phi_{bkg} - J_2(\frac{\wp}{R^2})\sin\phi_{bkg}\right) \tag{J.4}$$

When $0 < |\wp/R^2| < 2.63$, $J_1(|\wp/R^2|) > J_2(|\wp/R^2|) > 0$. In addition, when $|\phi_{bkg}| < \pi/4$, we have

$$2\pi\ell\rho_0\frac{\wp}{R^2}\left(J_1(\frac{\wp}{R^2})\cos\phi_{bkg} \pm J_2(\frac{\wp}{R^2})\sin\phi_{bkg}\right) = 2\pi\ell\rho_0\frac{|\wp|}{R^2}\left(J_1(\frac{|\wp|}{R^2})\cos\phi_{bkg} \pm J_2(\frac{\wp}{R^2})\sin\phi_{bkg}\right) > 0 \tag{J.5}$$

As the real parts of second derivatives are positive, this proves that our searching algorithm for the center of the object is still valid.

Appendix K

UNCERTAINTY OF SUSCEPTIBILITY QUANTIFIED FROM THE SAME IMAGE

These formulas are for magnetic moments and susceptibility values quantified from the same image and for cylinders at large orientations. In addition, the area chosen for quantifying the susceptibility, $\pi R_3'^2$, overlaps part of the area, $\pi(R_2^2 - R_3^2)$ (see Fig. 5.1b). The latter area is one of the annular regions for quantifying the magnetic moment. Because of this overlapping, we need to carefully separate these regions and ensure no correlation between those regions. We only use these formulas in this paper for comparison purpose, and we typically do not suggest having overlapping areas. As in theory, $Im(S_3' - S_3)$ is zero, we have neglected the uncertainty of $Im(S_3' - S_3)$.

$$\frac{\delta\Delta\chi}{\Delta\chi} = \frac{\sqrt{\delta\theta^2 A^2 + (\frac{\delta Re(S_3)}{\pi\ell\sigma})^2 B^2 + (\frac{\delta Im(S_3)}{\pi\ell\sigma})^2 C^2 + (\frac{\delta(S_1-S_2)}{\pi\ell\sigma})^2 D^2 + (\frac{\delta(S_3'-S_3)}{\pi\ell\sigma})^2 E^2 + (\frac{\delta(S_2-S_3')}{\pi\ell\sigma})^2 F^2}}{|\wp/g'| \left|\mathsf{SNR}_{0,c}\phi_{in} - \mathsf{SNR}_0 J_0(g')\sin\phi_{in}\right|} \tag{K.1}$$

where $\mathsf{SNR}_0 \equiv \rho_0/\sigma$, σ is the standard deviation of the thermal noise in images, and $\mathsf{SNR}_{0,c} \equiv \rho_{0,c}/\sigma$.

$$A = 2\cot\theta \left|\frac{\wp}{g'}\right| (\mathsf{SNR}_0 J_0(g')\sin\phi_{in} - g'\mathsf{SNR}_{0,c}) \tag{K.2}$$

$$B = -\sin\phi_{in}$$

$$C = \cos\phi_{in}$$

$$D = \sin\phi_{in}\left(\frac{h_3'}{h_{12}} + \frac{h_{23}\left(\frac{h_3'}{h_{12}}(\frac{J_0(\phi_2)}{\phi_2} - \frac{J_0(\phi_1)}{\phi_1}) + \frac{J_0(\phi_3')}{\phi_3'}\right)}{h_{12}\frac{J_0(\phi_3)}{\phi_3} + h_{23}\frac{J_0(\phi_1)}{\phi_1} + h_{31}\frac{J_0(\phi_2)}{\phi_2}}\right)$$

$$E = -\sin\phi_{in}\left(\frac{h_3'(\frac{J_0(\phi_2)}{\phi_2} - \frac{J_0(\phi_1)}{\phi_1}) + h_{12}\frac{J_0(\phi_3')}{\phi_3'}}{h_{12}\frac{J_0(\phi_3)}{\phi_3} + h_{23}\frac{J_0(\phi_1)}{\phi_1} + h_{31}\frac{J_0(\phi_2)}{\phi_2}} + 1\right)$$

$$F = -\sin\phi_{in}\frac{h_3'(\frac{J_0(\phi_2)}{\phi_2} - \frac{J_0(\phi_1)}{\phi_1}) + h_{12}\frac{J_0(\phi_3')}{\phi_3'}}{h_{12}\frac{J_0(\phi_3)}{\phi_3} + h_{23}\frac{J_0(\phi_1)}{\phi_1} + h_{31}\frac{J_0(\phi_2)}{\phi_2}}$$

where $h_3' = \int_{\phi_3'}^{|g'|}\frac{dx}{x^2}J_0(x)$, $\phi_3' = |\wp|/R_3'^2$,

$\phi_i \equiv |\wp|/R_i^2$, $i = 1$, 2, or 3

$$h_{ij} = \int_{\phi_i}^{\phi_j}\frac{dx}{x^2}J_0(x)$$

$$h_3 = \int_{\phi_3}^{|g'|}\frac{dx}{x^2}J_0(x)$$

$$\frac{\delta Re(S_3)}{\pi\ell\sigma} = \sqrt{\frac{\Delta x\Delta y R_3^2}{\pi} + \epsilon_R^2(\wp h_3 \mathsf{SNR}_0 + \mathsf{SNR}_{0,c}\frac{\wp}{|g'|}\cos\phi_{in})^2}$$

where ϵ_R is defined as the percentage difference between the theoretical $Re(S_3)$ and measured $Re(S_3)$ directly summed from simulated images without the Gaussian noise.

$$\frac{\delta Im(S_3)}{\pi\ell\sigma} = \sqrt{\frac{\Delta x\Delta y R_3^2}{\pi} + \epsilon_I^2(\mathsf{SNR}_{0,c}\frac{\wp}{g'}\sin\phi_{in})^2}$$

where ϵ_I is defined as the percentage difference between the theoretical $Im(S_3)$ and measured $Im(S_3)$ directly summed from simulated images without the Gaussian noise.

$$\frac{\delta(S_i - S_j)}{\pi\ell\sigma} = \sqrt{\frac{\Delta x\Delta y}{\pi}\left|R_i^2 - R_j^2\right| + \epsilon_{ij}^2(\wp h_{ij}\mathsf{SNR}_0)^2}$$

where $\epsilon_{ij} \equiv \delta(S_i - S_j)/(S_i - S_j)$ for $i,\ j = 1, 2, 3$ and the index i or j refers to the circle within which the complex signal is added. Similarly, ϵ_{ij} should be interpreted as the percentage difference between the theoretical $S_i - S_j$ (which is a real number) and the real part of $S_i - S_j$ directly summed from images.

$$\frac{\delta\rho_0}{\rho_0} = \frac{1}{\mathsf{SNR}_0}\sqrt{\left(\frac{G}{\wp}\right)^2\left(\frac{\delta(S_1 - S_2)}{\pi\ell\sigma}\right)^2 + \left(\frac{H}{\wp}\right)^2\left(\frac{\delta(S_2 - S_3)}{\pi\ell\sigma}\right)^2}$$

where

$$\frac{G}{\wp} = \frac{1}{\wp h_{12}} + \frac{\frac{h_{23}}{h_{12}}\left(h_{12} + \frac{J_0(\phi_2)}{\phi_2} - \frac{J_0(\phi_1)}{\phi_1}\right)}{\wp\left(h_{12}\frac{J_0(\phi_3)}{\phi_3} + h_{23}\frac{J_0(\phi_1)}{\phi_1} + h_{31}\frac{J_0(\phi_2)}{\phi_2}\right)}$$

$$\frac{H}{\wp} = \frac{-\left(h_{12} + \frac{J_0(\phi_2)}{\phi_2} - \frac{J_0(\phi_1)}{\phi_1}\right)}{\wp\left(h_{12}\frac{J_0(\phi_3)}{\phi_3} + h_{23}\frac{J_0(\phi_1)}{\phi_1} + h_{31}\frac{J_0(\phi_2)}{\phi_2}\right)}$$

As the cross-sectional area of the cylinder is defined as $A_0 \equiv \pi a^2$, the uncertainty of the cross-sectional area is

$$\frac{\delta A_0}{A_0} = \left[\left(\frac{A}{I} + 2\cot\theta\right)^2 \delta\theta^2 + \left(\frac{B}{I}\right)^2 \left(\frac{\delta Re(S_3)}{\pi\ell\sigma}\right)^2 + \left(\frac{C}{I}\right)^2 \left(\frac{\delta Im(S_3)}{\pi\ell\sigma}\right)^2 + \left(\frac{h_{12}}{J} - \frac{F}{I}\right)^2 \left(\frac{\delta(S_2 - S_3')}{\pi\ell\sigma}\right)^2 + \left(\frac{h_{12}}{J} - \frac{E}{I}\right)^2 \left(\frac{\delta(S_3' - S_3)}{\pi\ell\sigma}\right)^2 + \left(\frac{h_{23}}{J} + \frac{D}{I}\right)^2 \left(\frac{\delta(S_1 - S_2)}{\pi\ell\sigma}\right)^2\right]^{1/2}$$

where

$$I = |\wp/g'|\left(\mathsf{SNR}_{0,c}\phi_{in} - \mathsf{SNR}_0 J_0(g')\sin\phi_{in}\right)$$

$$J = |\wp|\mathsf{SNR}_0\left(h_{12}\frac{J_0(\phi_3)}{\phi_3} + h_{23}\frac{J_0(\phi_1)}{\phi_1} + h_{31}\frac{J_0(\phi_2)}{\phi_2}\right)$$

$$\frac{\delta\rho_{0,c}}{\rho_{0,c}} = \left[\left(\frac{\delta Im(S_3)}{\pi\ell\sigma}\right)^2 \left(\frac{1}{a^2\sin\phi_{in}\mathsf{SNR}_{0,c}} + \frac{C}{I}(1 - \phi_{in}\cot\phi_{in})\right)^2 + \left(\frac{\delta Re(S_3)}{\pi\ell\sigma}\right)^2 \left(\frac{B}{I}(1 - \phi_{in}\cot\phi_{in})\right)^2 + \left(\frac{\delta(S_1 - S_2)}{\pi\ell\sigma}\right)^2 K^2 + \left(\frac{\delta(S_3' - S_3)}{\pi\ell\sigma}\right)^2 L^2 + \left(\frac{\delta(S_2 - S_3')}{\pi\ell\sigma}\right)^2 M^2 + (\delta\theta)^2\left(\frac{A}{I}(1 - \phi_{in}\cot\phi_{in}) - g\sin 2\theta\cot\phi_{in} + 2\cot\theta\right)^2\right]^{1/2}$$

where

$$K = \frac{D}{I}(1 - \phi_{in}\cot\phi_{in}) + \frac{h_{23}}{J}$$

$$L = \frac{E}{I}(1 - \phi_{in} \cot \phi_{in}) - \frac{h_{12}}{J}$$

$$M = \frac{F}{I}(1 - \phi_{in} \cot \phi_{in}) - \frac{h_{12}}{J}$$

Appendix L

UNCERTAINTY OF SUSCEPTIBILITY QUANTIFIED FROM DIFFERENT IMAGES

The formulas here are suitable for unknowns quantified from different images. In addition, these formulas are particularly for cylinders with orientations larger than 30°. When the susceptibility is quantified from the shorter echo time with S_3, which is enclosed by the radius R_3, the uncertainty of the susceptibility is

$$\frac{\delta\Delta\chi}{\Delta\chi} = \frac{\sqrt{\delta\theta^2 A^2 + (\frac{\delta Re(S_3)}{\pi\ell\sigma})^2 B^2 + (\frac{\delta Im(S_3)}{\pi\ell\sigma})^2 C^2 + (\frac{\delta\wp}{\wp})^2 D^2 + (\frac{\delta(S_1-S_2)}{\pi\ell\sigma})^2 E^2}}{|I|} \tag{L.1}$$

$$D = -|\wp|\mathrm{SNR}_0 \left(\frac{J_0(\phi_3)}{\phi_3} + \frac{h_3}{h_{12}} \left(\frac{J_0(\phi_2)}{\phi_2} - \frac{J_0(\phi_1)}{\phi_1} \right) \right) \sin\phi_{in}$$

$$E = \frac{h_3}{h_{12}} \sin\phi_{in}$$

$$\frac{\delta\rho_0}{\rho_0} = \frac{1}{h_{12}} \left[\left(\frac{1}{\wp \mathrm{SNR}_0} \right)^2 \left(\frac{\delta(S_1 - S_2)}{\pi\ell\sigma} \right)^2 + \left(h_{12} + \frac{J_0(\phi_2)}{\phi_2} - \frac{J_0(\phi_1)}{\phi_1} \right)^2 \left(\frac{\delta\wp}{\wp} \right)^2 \right]^{1/2}$$

where the uncertainty of ρ_0 here is quantified from the image acquired at the shorter echo time, with the choice of two concentric circles, R_1 and R_2.

$$\begin{aligned} \frac{\delta A_0}{A_0} &= \left[\left(\frac{A}{I} + 2\cot\theta \right)^2 \delta\theta^2 + \left(\frac{B}{I} \right)^2 \left(\frac{\delta Re(S_3)}{\pi\ell\sigma} \right)^2 + \left(\frac{C}{I} \right)^2 \left(\frac{\delta Im(S_3)}{\pi\ell\sigma} \right)^2 + \left(\frac{E}{I} \right)^2 \left(\frac{\delta(S_1 - S_2)}{\pi\ell\sigma} \right)^2 \right. \\ &+ \left. \left(1 - \frac{D}{I} \right)^2 \left(\frac{\delta\wp}{\wp} \right)^2 \right]^{1/2} \end{aligned}$$

$$\frac{\delta\rho_{0,c}}{\rho_{0,c}} = \left[O^2(\delta\theta)^2 + P^2\left(\frac{\delta Im(S_3)}{\pi\ell\sigma}\right)^2 + Q^2\left(\frac{\delta Re(S_3)}{\pi\ell\sigma}\right)^2 + R^2\left(\frac{\delta\wp}{\wp}\right)^2 + S^2\left(\frac{\delta(S_1 - S_2)}{\pi\ell\sigma}\right)\right]^{1/2}$$

where

$$O = \frac{A}{I}(1 - \phi_{in}\cot\phi_{in}) - g\sin 2\theta\cot\phi_{in} + 2\cot\theta$$

$$P = (1 - \phi_{in}\cot\phi_{in})\frac{C}{I} + \frac{1}{a^2\mathrm{SNR}_{0,c}\sin\phi_{in}}$$

$$Q = (1 - \phi_{in}\cot\phi_{in})\frac{B}{I}$$

$$R = (1 - \phi_{in}\cot\phi_{in})\frac{D}{I} - 1$$

$$S = (1 - \phi_{in}\cot\phi_{in})\frac{E}{I}$$

Appendix M

UNCERTAINTY OF SUSCEPTIBILITY FOR CYLINDERS AT SMALL ORIENTATIONS

We derive these uncertainties based on the variations of the susceptibility and cross-sectional area of a cylindrical object from images acquired at two echo times (Eq. 5.7). In this Appendix, subscripts 1 and 2 in the following equations refer to the values quantified from echo time T_{E_1} and T_{E_2}, respectively. If none of the phase values from either echo time is close to multiples of π, then these equations below lead to smaller and more realistic uncertainties than those given in the Appendix B of [10].

$$\begin{aligned}\frac{\delta\Delta\chi}{\Delta\chi} &= \frac{1}{|\mathbb{E}|}\Bigg[(\mathbb{B}_2\mathbb{F}_1)^2\left(\frac{\delta Re(S_1)}{\pi\ell\sigma}\right)^2+(\mathbb{B}_2\mathbb{G}_1)^2\left(\frac{\delta Im(S_1)}{\pi\ell\sigma}\right)^2+(\mathbb{B}_2\mathbb{D}_1)^2\left(\frac{\delta\rho_{0,1}}{\rho_{0,1}}\right)^2 \\ &+ (\delta\theta_1)^2(\mathbb{B}_2\mathbb{C}_1)^2+(\mathbb{B}_1\mathbb{F}_2)^2\left(\frac{\delta Re(S_2)}{\pi\ell\sigma}\right)^2+(\mathbb{B}_1\mathbb{G}_2)^2\left(\frac{\delta Im(S_2)}{\pi\ell\sigma}\right)^2 \\ &+ (\mathbb{B}_1\mathbb{D}_2)^2\left(\frac{\delta\rho_{0,2}}{\rho_{0,2}}\right)^2+(\delta\theta_2)^2(\mathbb{B}_1\mathbb{C}_2)^2\Bigg]^{1/2}\end{aligned}$$

If the orientation of the object is measured only once from both echo times, the term $(\delta\theta_1)^2(\mathbb{B}_2\mathbb{C}_1)^2+(\delta\theta_2)^2(\mathbb{B}_1\mathbb{C}_2)^2$ should be replaced by $(\delta\theta)^2(\mathbb{B}_2\mathbb{C}_1-\mathbb{B}_1\mathbb{C}_2)^2$ in the above uncertainty formula.

$$\mathbb{A}_n=\phi_{in,n}\mathrm{SNR}_{0,c,n}+\frac{g_n'^2}{2}\left(1-\frac{a^2}{R^2}\right)\mathrm{SNR}_{0,n}\sin\phi_{in,n}$$

$$\mathbb{B}_n=\left(1+\frac{g_n'^2}{4}-\frac{g_n'^2a^2}{2R^2}\right)\mathrm{SNR}_{0,n}\sin\phi_{in,n}$$

$$\mathbb{C}_n=-a^2g_n\sin 2\theta_n\left(\mathrm{SNR}_{0,c,n}+\frac{g_n'}{2}\left(1-\frac{a^2}{R^2}\right)\mathrm{SNR}_{0,n}\sin\phi_{in,n}\right)$$

$$\mathbb{D}_n=(R^2-a^2)\left(1-\frac{g_n'^2a^2}{4R^2}\right)\mathrm{SNR}_{0,n}\sin\phi_{in,n}$$

$$\mathbb{E} = a^2(\mathbb{B}_2\mathbb{A}_1 - \mathbb{B}_1\mathbb{A}_2)$$

$$\mathbb{F}_n = -\sin\phi_{in,n}$$

$$\mathbb{G}_n = \cos\phi_{in,n}$$

$$\frac{\delta Re(S_n)}{\pi\ell\sigma} = \sqrt{\frac{\Delta x\Delta y R^2}{\pi} + \epsilon_R^2\left(\frac{Re(S_n)}{\pi\ell\sigma}\right)^2}$$

$$\frac{\delta Im(S_n)}{\pi\ell\sigma} = \sqrt{\frac{\Delta x\Delta y R^2}{\pi} + \epsilon_I^2\left(\frac{Im(S_n)}{\pi\ell\sigma}\right)^2}$$

$$\frac{\delta\rho_{0,n}}{\rho_{0,n}} = \sqrt{\frac{\Delta x\Delta y}{\pi(R_a^2 - R_b^2)\mathrm{SNR}_{0,n}^2} + \epsilon_{ab}^2}$$

where ϵ_{ab} is the percentage difference between the theoretical spin density and the measured spin density within the annular ring defined by radii R_a and R_b. The subscript n in $\rho_{0,n}$ or $\phi_{in,n}$ refers to each variable obtained at the n^{th} echo time T_{E_n}.

$$\begin{aligned}\frac{\delta A_0}{A_0} &= \frac{1}{|\mathbb{E}|}\Bigg[(\mathbb{A}_1\mathbb{G}_2)^2\left(\frac{\delta Im(S_2)}{\pi\ell\sigma}\right)^2 + (\mathbb{A}_2\mathbb{G}_1)^2\left(\frac{\delta Im(S_1)}{\pi\ell\sigma}\right)^2 \\ &+ (\mathbb{A}_2\mathbb{F}_1)^2\left(\frac{\delta Re(S_1)}{\pi\ell\sigma}\right)^2 + (\mathbb{A}_1\mathbb{F}_2)^2\left(\frac{\delta Re(S_2)}{\pi\ell\sigma}\right)^2 \\ &+ (\mathbb{A}_2\mathbb{D}_1)^2\left(\frac{\delta\rho_{0,1}}{\rho_{0,1}}\right)^2 + (\mathbb{A}_1\mathbb{D}_2)^2\left(\frac{\delta\rho_{0,2}}{\rho_{0,2}}\right)^2 \\ &+ (\delta\theta_1)^2(\mathbb{A}_2\mathbb{C}_1)^2 + (\delta\theta_2)^2(\mathbb{A}_1\mathbb{C}_2)^2\Bigg]^{1/2}\end{aligned}$$

If the orientation of the object is measured only once from both echo times, the term $(\delta\theta_1)^2(\mathbb{A}_2\mathbb{C}_1)^2 + (\delta\theta_2)^2(\mathbb{A}_1\mathbb{C}_2)^2$ should be replaced by $(\delta\theta)^2(\mathbb{A}_2\mathbb{C}_1 - \mathbb{A}_1\mathbb{C}_2)^2$ in the above uncertainty formula.

$$\frac{\delta\rho_{0,c,n}}{\rho_{0,c,n}} = \left[(\delta\theta_1)^2\mathbb{H}^2 + \left(\frac{\delta\rho_{0,1}}{\rho_{0,1}}\right)^2\mathbb{I}^2 + \left(\frac{\delta Re(S_1)}{\pi\ell\sigma}\right)^2\mathbb{J}^2 + \left(\frac{\delta Im(S_1)}{\pi\ell\sigma}\right)^2\mathbb{K}^2 \right.$$
$$\left. + (\delta\theta_2)^2\mathbb{L}^2 + \left(\frac{\delta\rho_{0,2}}{\rho_{0,2}}\right)^2\mathbb{M}^2 + \left(\frac{\delta Re(S_2)}{\pi\ell\sigma}\right)^2\mathbb{N}^2 + \left(\frac{\delta Im(S_2)}{\pi\ell\sigma}\right)^2\mathbb{O}^2\right]^{1/2}$$

If the orientation of the object is measured only once from both echo times, the term $(\delta\theta_1)^2(\mathbb{H})^2 + (\delta\theta_2)^2(\mathbb{L})^2$ should be replaced by $(\delta\theta)^2(\mathbb{H}+\mathbb{L})^2$ in the above uncertainty formula.

$$\mathbb{H} = -\delta_{n,1}g_1 \sin 2\theta_1 \cot\phi_{in,1} + (\mathbb{A}_2 - \mathbb{B}_2\phi_{in,n}\cot\phi_{in,n})\frac{\mathbb{C}_1}{\mathbb{E}}$$

$$\mathbb{L} = -\delta_{n,2}g_2 \sin 2\theta_2 \cot\phi_{in,2} - (\mathbb{A}_1 - \mathbb{B}_1\phi_{in,n}\cot\phi_{in,n})\frac{\mathbb{C}_2}{\mathbb{E}}$$

where $\delta_{n,1}$ and $\delta_{n,2}$ are Kronecker delta functions. The subscript n refers to each variable measured at the n^{th} echo time T_{E_n}.

$$\mathbb{I} = \mathbb{D}_1\left(\frac{\mathbb{A}_2}{\mathbb{E}} - \frac{\mathbb{B}_2}{\mathbb{E}}\phi_{in,n}\cot\phi_{in,n}\right)$$

$$\mathbb{M} = -\mathbb{D}_2\left(\frac{\mathbb{A}_1}{\mathbb{E}} - \frac{\mathbb{B}_1}{\mathbb{E}}\phi_{in,n}\cot\phi_{in,n}\right)$$

$$\mathbb{J} = (\mathbb{A}_2 - \mathbb{B}_2\phi_{in,n}\cot\phi_{in,n})\frac{\mathbb{F}_1}{\mathbb{E}}$$

$$\mathbb{N} = (-\mathbb{A}_1 + \mathbb{B}_1\phi_{in,n}\cot\phi_{in,n})\frac{\mathbb{F}_2}{\mathbb{E}}$$

$$\mathbb{K} = \frac{\delta_{n,1}}{a^2\mathrm{SNR}_{o,c,1}\sin\phi_{in,1}} + (\mathbb{A}_2 - \mathbb{B}_2\phi_{in,n}\cot\phi_{in,n})\frac{\mathbb{G}_1}{\mathbb{E}}$$

$$\mathbb{O} = \frac{\delta_{n,2}}{a^2 \mathrm{SNR}_{o,c,2} \sin \phi_{in,2}} - \left(\mathbb{A}_1 - \mathbb{B}_1 \phi_{in,n} \cot \phi_{in,n}\right) \frac{\mathbb{G}_2}{\mathbb{E}}$$

REFERENCES

[1] E. M. Haacke, Y. Xu, Y.-C. N. Cheng, and J. Reichenbach, Magn. Reson. Med. **52**, 612 (2004).

[2] E. M. Haacke et al., Magn. Reson. Imaging **23**, 1 (2005).

[3] E. M. Haacke and J. Reichenbach, *SUSCEPTIBILITY WEIGHTED IMAGING in MRI*, John Wiley & Sons, New York, 2010.

[4] E. M. Haacke et al., J. Magn. Reson. Imaging **26**, 256 (2007).

[5] K. Tong et al., Ann. Neurol. **56**, 36 (2004).

[6] Y. Ge et al., J. Magn. Reson. Imaging **29**, 1190 (2009).

[7] Y.-C. N. Cheng et al., Magn. Reson. Imaging **25**, 1171 (2007).

[8] Y.-C. N. Cheng, C.-Y. Hsieh, J. Neelavalli, and E. M. Haacke, Phys. Med. Biol. **54**, 7025 (2009).

[9] Y.-C. N. Cheng et al., Magn. Reson. Imaging **33**, 829 (2015).

[10] C.-Y. Hsieh, Y.-C. N. Cheng, J. Neelavalli, E. M. Haacke, and R. J. Stafford, Magn. Reson. Imaging **33**, 420 (2015).

[11] C.-Y. Hsieh, Y.-C. N. Cheng, H. Xie, J. Neelavalli, and E. M. Haacke, Magn. Reson. Imaging **33**, 1191 (2015).

[12] E. M. Haacke, R. W. Brown, M. R. Thompson, and R. Venkatesan, *Magnetic Resonance Imaging: Physical Principles and Sequence Design*, John Wiley & Sons, New York, 1999.

[13] R. M. Weisskoff and S. Kiihne, Magn. Reson. Med. **24**, 375 (1992).

[14] S. Lai et al., Magn. Reson. Med. **30**, 387 (1993).

[15] J. Sedlacik, A. Rauscher, and J. R. Reichenbach, Magn. Reson. Med. **58**, 1035 (2007).

[16] J. D. Jackson, *Classical Electrodynamics*, John Wiley & Sons, New York, 1999.

[17] P. Robson and L. Hall, American Institute of Chemical Engineers **51**, 1633 (2005).

[18] P. R. Bevington and D. K. Robinson, *Data Reduction and Error Analysis for the Physical Sciences*, McGraw-Hill, New York, 1992.

[19] W. H. Press, S. A. Teukolsky, W. T. Vetterling, and B. P. Flannery, *Numerical Recipes in C: The Art of Scientific Computing*, John Wiley & Sons, New York, 1992.

[20] C.-Y. Hsieh, Y.-C. N. Cheng, J. Neelavalli, and E. M. Haacke, Proceedings of the International Society for Magnetic Resonance in Medicine , 2596 (2007).

[21] L. DR, *Handbook of Chemistry and Physics, 87th ed.*, CRC Press, New York, 2006–2007.

[22] S. M. Greenberg et al., Lancet. Neurol. $\mathbf{8}$, 165 (2009).

[23] C. Bos, M. A. Viergever, and C. J. G. Bakker, Magn. Reson. Med. $\mathbf{50}$, 400 (2003).

[24] S. Liu, J. Neelavalli, Y.-C. N. Cheng, J. Tang, and E. Mark Haacke, Magnetic Resonance in Medicine $\mathbf{69}$, 716 (2013).

[25] Y.-C. N. Cheng, E. M. Haacke, , and Y.-J. Yu, Magn. Reson. Imaging $\mathbf{19}$, 1017 (2001).

[26] E. M. Haacke, Y.-C. N. Cheng, E. M. Haacke, M. R. Thompson, and R. Venkatesan, *Magnetic Resonance Imaging: Physical Principles and Sequence Design*, John Wiley & Sons, New York, second edition, 2014.

[27] G. Hagberg, E. Welch, and A. Greiser, Magnetic Resonance Imaging $\mathbf{28}$, 297 (2010).

[28] F. Schweser, A. Deistung, B. W. Lehr, and J. R. Reichenbach, NeuroImage $\mathbf{54}$, 2789 (2011).

[29] S. Ogawa et al., Biophys. J. $\mathbf{64}$, 803 (1993).

[30] M. C. Langham, J. F. Magland, C. L. Epstein, T. F. Floyd, and F. W. Wehrli, Magn. Reson. Med. $\mathbf{62}$, 333 (2009).

[31] J. Marques and R. Bowtell, Concepts in Magnetic Resonance Part B: Magnetic Resonance Engineering $\mathbf{25}$, 65 (2005).

[32] Y.-C. N. Cheng, J. Neelavalli, and E. M. Haacke, Phys. Med. Biol. $\mathbf{54}$, 1169 (2009).

[33] L. de Rochefort, R. Brown, M. R. Prince, and Y. Wang, Magnetic Resonance in Medicine $\mathbf{60}$, 1003 (2008).

[34] T. Liu, P. Spincemaille, L. de Rochefort, B. Kressler, and Y. Wang, Magnetic Resonance in Medicine $\mathbf{61}$, 196 (2009).

[35] E. M. Haacke, J. Tang, J. Neelavalli, and Y.-C. N. Cheng, J. Magn. Reson. Imaging **32**, 663 (2010).

[36] W. Li, B. Wu, and C. Liu, NeuroImage **55**, 1645 (2011).

[37] F. Schweser, K. Sommer, A. Deistung, and J. R. Reichenbach, NeuroImage **62**, 2083 (2012).

[38] J. Tang et al., Magnetic Resonance in Medicine **69**, 1396 (2013).

[39] S. Wharton and R. Bowtell, NeuroImage **53**, 515 (2010).

[40] B. Kressler et al., IEEE T. MED. Imaging **29**, 273 (2010).

[41] L. de Rochefort et al., Magnetic Resonance in Medicine **63**, 194 (2010).

[42] B. Bilgic, A. Pfefferbaum, T. Rohlfing, E. V. Sullivan, and E. Adalsteinsson, NeuroImage **59**, 2625 (2012).

[43] A. P. Fan et al., Magnetic Resonance in Medicine **72**, 149 (2014).

[44] B. Xu, T. Liu, P. Spincemaille, M. Prince, and Y. Wang, Magnetic Resonance in Medicine **72**, 438 (2014).

[45] C. Springer and Y. Xu, European Magnetic Resonance Forum, Blonay , 13 (1991).

[46] J. Schenck, Medical Physics **23**, 815 (1996).

[47] T. Liu et al., Radiology **262**, 269 (2012).

[48] D. NEMA, *Digital Imaging and Communications in Medicine (DICOM) Part 3:Information Object Definitions*, National Electrical Manufacturers Association, Rosslyn, 2011, PS 3.3-2011.

[49] T. Liu, W. Xu, P. Spincemaille, A. Avestimehr, and Y. Wang, Medical Imaging, IEEE Transactions on **31**, 816 (2012).

[50] W. M. Spees, D. A. Yablonskiy, M. C. Oswood, and J. J. Ackerman, Magnetic Resonance in Medicine **45**, 533 (2001).

[51] C. Li et al., Magn. Reson.Med. **67**, 808 (2012).

[52] M. A. Fernndez-Seara, A. Techawiboonwong, J. A. Detre, and F. W. Wehrli, Magnetic Resonance in Medicine **55**, 967 (2006).

[53] V. Jain, M. C. Langham, and F. W. Wehrli, J. Cereb Blood Flow Metab **30**, 1598 (2010).

[54] L. C. Krishnamurthy, P. Liu, Y. Ge, and H. Lu, Magnetic Resonance in Medicine **71**, 978 (2014).

[55] I. D. Driver et al., NeuroImage **101**, 458 (2014).

[56] E. M. Haacke et al., Hum Brain Mapp **5**, 341 (1997).

[57] Q. Yang et al., Journal of Magnetic Resonance Imaging **30**, 357 (2009).

[58] L. L. Muldoon et al., Am. J. Neuroradiol. **27**, 715 (2006).

[59] C. V. Bowen, X. Zhang, G. Saab, P. J. Gareau, and B. K. Rutt, Magn. Reson. Med. **48**, 52 (2002).

[60] P. Kokeny et al., ISMRM 2015 Proceedings , 1722 (2015).

[61] P. RA et al., F1000Research **2**, 1 (2013).

[62] H. Xie, Y. N. Cheng, C. Hsieh, P. Kokeny, and E. M. Haacke, ISMRM 2015 Proceedings , 1724 (2015).

[63] S. Buch et al., Magnetic Resonance in Medicine **73**, 2185 (2015).

ABSTRACT

QUANTIFYING MAGNETIC MOMENTS AND SUSCEPTIBILITIES OF SMALL CYLINDRICAL AND SPHERICAL OBJECTS IN MRI

by

CHING-YI HSIEH

December 2015

Advisor: Professor Yu-Chung Norman Cheng

Major: Medical Physics

Degree: Doctor of Philosophy

$\mathbf{Purpose}$: The purpose of this PhD work is to develop a method called Complex Image Summation around a Spherical or Cylindrical Object (CISSCO) for accurate magnetic moment and susceptibility quantifications of narrow cylindrical-like or small spherical-like objects from magnetic resonance imaging (MRI). A typical 3D gradient echo sequence with only one echo time is intended for our approach. For accurate susceptibility quantifications of cylindrical objects at orientations relatively close to the main field, two echo times are needed.

$\mathbf{Methods}$: Our method is to sum over complex MR signals around an object of interest and equates those sums to equations derived from the magnetostatic theory. With those equations, our method is able to determine the center of the object with a subpixel precision. Furthermore, those equations allow us to systematically solve the effective magnetic moment, spin density around the object, susceptibility, and radius of the object in sequence. The uncertainty of each quantified variable is calculated from the error propagation method. For the object without an MR signal, a spin echo sequence can be used to determine the volume of the object, and the susceptibility difference between the object and its surrounding can be further calculated from the magnetic moment. Numerical simulations, a variety of air straws, glass beads, and straws filled with gadolinium in phantom studies with different MR imaging parameters on a 1.5 T or 3 T machine have

been conducted to verify the method. In addition, magnetic moments and susceptibilities of several cerebral veins have also been quantified from 3 T and 4 T human images.

Results: Quantified effective magnetic moments and susceptibility differences from different imaging parameters all agree with each other within two standard deviations of estimated uncertainties. Those results also agree with expected values within uncertainties when available in the literature.

Conclusion: The CISSCO method is developed to accurately quantify the effective magnetic moment and susceptibility of a given small object of interest. Most results are accurate within 10% of true values and roughly half of the total results are accurate within 5% of true values using reasonable imaging parameters. The method is minimally affected by the partial volume, dephasing, and phase aliasing effect.

AUTOBIOGRAPHICAL STATEMENT

Name: CHING-YI HSIEH, DABR

Education:

PhD Medical Physics, Wayne State University, Detroit, MI, Sep. 2004-Present

M.S. Physics, The State University of New York at Buffalo, NY, Sept. 2004

B.S. Physics, Chung Yuan Christian University, Chung Li, Taiwan, June 1997

Professional Experience:

Student Assistant, Dept. of Radiology, Wayne State University, June, 2013-Present

Imaging Physics Resident, MD Anderson Cancer Center, Houston, TX, 2010-2012

Graduate Teaching Assistant, Department of Physics, The State University of New York at Buffalo, 2002-2004

Publications:

C. Hsieh, Y.-C.N. Cheng, He Xie, E.M. Haacke, J. Neelavalli, Susceptibility and size quantifications of small human veins from an MRI method, *Magn. Reson. Imaging*, (33) 2015, pp. 1191-1204, `http://dx.doi.org/10.1016/j.mri.2015.07.008`.

Y.-C.N. Cheng, **C. Hsieh**, R. Tackett, P. Kokeny, R. Regmi, G. Lawes, An Effective Magnetic Moment Quantifications of Small Spherical Objects in MRI, *Magn. Reson. Imaging*, (33) 2015, pp. 829-839.

C. Hsieh, Y.-C.N. Cheng, J. Neelavalli, E.M. Haacke, R.J. Stafford, An Improved Method for Susceptibility and Radius Quantification of Cylindrical Objects from MRI, *Magn. Reson. Imaging*, (33) 2015, pp. 420-436.

C. Hsieh, G. Gladish, C.E. Willis, Evaluation of a commercial cardiac motion phantom for dual-energy chest radiography. J Appl Clin Med Phy. 2014 Mar;15(2), pp. 235-251.

Y.-C. Cheng, **C. Hsieh**, J. Neelavalli, and E.M. Haacke, Quantifying Effective Magnetic Moments and Susceptibilities of Narrow Cylindrical Objects in MRI, *Phys. Med. Biol.*, 54, 2009, pp. 7025-7044.

Y.-C. Cheng, **C. Hsieh**, J. Neelavalli, Q. Liu, M.S. Dawood and E.M. Haacke, A Complex Sum Method of Quantifying Susceptibilities in Cylindrical Objects, *Magn. Reson. Imaging*, (8) 2007, pp. 1171-1180.